Université de Toulouse

Habilitation à Diriger des Recherches

Spécialité : "Physique des particules"

Physics with Boson Pairs

Présenté et soutenue publiquement par:
Dr. Joany MANJARRÉS RAMOS
le 15 Juillet 2025

Jury composé de
Oscar ÉBOLI
Ursula BASSLER
Gautier HAMEL DE MONCHENAULT
Pierre PUJOL
Jan STARK

Document soumis en vue de l'obtention de
l'Habilitation à diriger des recherches

January 12, 2026

Contents

Introduction

The first decade of operations at the Large Hadron Collider (LHC) has firmly established the success of the Standard Model (SM) of particle physics, confirming it as a remarkably accurate framework for describing fundamental interactions. The discovery of the Higgs boson, along with the observation of rare processes such as light-by-light scattering [1], triboson production [2, 3], and the electroweak production of massive vector bosons [4–7], are among the most significant recent achievements. Yet, the SM leaves many fundamental questions unanswered — the origin of the cosmological baryon asymmetry, the nature of dark matter and dark energy, and the unification of forces. These open problems make the search for physics beyond the Standard Model (BSM) more pressing than ever.

Despite intensive efforts, the LHC data have so far revealed no direct signs of new physics. The ATLAS and CMS experiments have set increasingly stringent exclusion limits, pushing the mass scales of hypothetical new particles into the multi-TeV range. This evolving landscape calls for a shift in strategy: instead of hunting for bumps and resonances, we must dig deeper into the structure of the known — using precision, subtle signatures, and rare processes to probe what lies beneath. In this context, one of the most promising places to search for new physics is within the mechanism that gives mass to fundamental particles: electroweak symmetry breaking (EWSB). This mechanism, realized through the Higgs field, not only generates the masses of the W and Z bosons but also governs how these bosons interact at high energies. It ensures the unitarity of their scattering amplitudes and defines the self-coupling structure of the Higgs boson itself.

Understanding this sector in depth remains one of the central goals of modern particle physics. With the discovery of the Higgs boson, we have entered a new era — one that focuses not only on confirming its existence, but also on unraveling the structure of the scalar potential and probing the dynamics of EWSB itself. In this endeavor, the production of boson pairs — involving the W, Z, and Higgs bosons — plays a crucial role. Their properties, production rates, angular distributions, and polarizations provide a rich testing ground for the SM and a potential window into new physics.

A key part of this picture is polarization. The longitudinal modes of massive vector bosons arise directly from the Higgs mechanism, and their behavior at high energies provides a unique fingerprint of EWSB. Measuring polarization in vector boson scattering (VBS) processes is thus not only technically challenging but also theoretically profound: it connects directly to the dynamics of electroweak symmetry breaking and the role of the Higgs field in defining the vacuum state and the mass of vector bosons. For me, this connection has been more than a theoretical motivation: it has guided my research path and shaped the questions I continue to pursue. These themes — VBS and boson polarization — lie at the heart of my research.

At the same time, we know the Standard Model does not provide all the answers. Boson pair production offers not only precision tests of the theory but also have discovery potential. New heavy particles — such as vector resonances or scalar states — could decay into boson pairs, producing distinct signatures in invariant mass distributions and angular correlations. Even if new physics lies beyond the direct energy reach of the LHC, its virtual effects can still appear in these channels and be captured through Effective

Field Theory (EFT) frameworks. My research has aimed to bridge these two complementary directions: precision and exploration. I have been fortunate to contribute to both direct and indirect searches using boson pairs.

This document summarizes my contributions to this vibrant and challenging field over the past twelve years. It reflects a journey — shaped by collaboration, dialogue, and mentorship — through the rich dynamics of electroweak boson interactions, from in-depth studies of the Standard Model to broader searches for physics beyond the Standard Model. The experimental framework — including the LHC, the ATLAS detector, and the reconstruction of physics objects — is introduced in Chapter 1. Chapter 2 presents a selection of precision tests of the Standard Model, with a focus on vector boson scattering and polarization. Chapter 3 delves into the search for new physics, highlighting both the direct searches I contributed to and the indirect probes conducted within the Effective Field Theory approach. Finally, Chapter 4 offers a brief outlook on future directions and open questions that continue to shape this field.

1 Experimental Aspects: Production, Detection, and Identification of Bosons

Diboson interactions provide a powerful probe of the Standard Model and a sensitive avenue for exploring possible deviations that may hint at physics beyond it. Experimentally to study them, we need both a reliable source of bosons and a detector capable of identifying W, Z, and Higgs bosons with high precision.

The Large Hadron Collider (LHC), described in Section 1.1, offers an ideal setting for such studies. It has produced an unprecedented number of W, Z, and Higgs bosons—surpassing all previous accelerators. While W and Z bosons were already well-measured prior to the LHC, the Higgs boson was discovered there for the first time.

Detecting and measuring the particles emerging from LHC collisions is the task of the ATLAS detector and collaboration, introduced in Section 1.2. A central challenge is that the bosons of interest decay almost immediately and never reach the detector directly. Their presence must be inferred from their decay products, which are first reconstructed as individual objects (Section 1.3), and then combined to form boson candidates (Section 1.4).

The W, Z, and Higgs bosons decay to a range of final states with varying probabilities, producing particles that the ATLAS detector can observe. My research focuses primarily on leptonic decays of W and Z bosons. Despite their relatively small branching fractions, these channels are especially valuable due to the precision with which ATLAS can reconstruct electrons and muons. In contrast, for multiboson studies involving Higgs bosons I rely on hadronic decays— $H \rightarrow b\bar{b}$—because of his larger branching ratio, which enhance the chances of detection. The following sections will highlight key aspects relevant to the reconstruction of the objects used in my research.

1.1 The Large Hadron Collider

The Large Hadron Collider (LHC)[8] is the most powerful particle accelerator ever built. Since 2010, it has been colliding protons[1] at increasingly higher center-of-mass energies and luminosities. Designed to reach a maximum proton energy of 7 TeV, it is expected enable proton-proton (pp) collisions up to a center-of-mass energy of $\sqrt{s} = 14$ TeV.

The LHC is a 27 km superconducting ring located beneath the French-Swiss border. Proton beams are guided close to the speed of light using powerful magnets and brought into collision at four interaction points, where major experiments are installed. ATLAS (A Toroidal LHC ApparatuS) and CMS (Compact Muon Solenoid) are general-purpose detectors designed to explore a wide range of phenomena. ALICE (A Large Ion Collider Experiment) specializes in heavy-ion physics, and LHCb (Large Hadron Collider

[1] While the LHC primarily collides protons, it can also accelerate and collide heavy ions, such as lead–lead and proton–lead beams.

beauty) focuses on the study of b-hadrons. Proton-proton collisions occur at a staggering rate of up to 40 million per second (one every 25 nanoseconds).

Since the start of operations, the LHC has completed three major data-taking periods, or Runs. Run-1 (2010–2013) recorded collisions at 7 and 8 TeV. Run-2 (2015–2018) delivered data at 13 TeV, and the ongoing Run-3, which began in 2022, operates at 13.6 TeV. Figure1.2 (left) shows the cumulative luminosity delivered to ATLAS over the years. The slope of the curve reflects the instantaneous luminosity, which determines the rate of interactions. Figure 1.2 (right) presents the average number of interactions per bunch crossing ($\langle\mu\rangle$), which has increased significantly across the Runs—already exceeding design expectations during Run-2. The results discussed in this document are primarily based on Run-2 data.

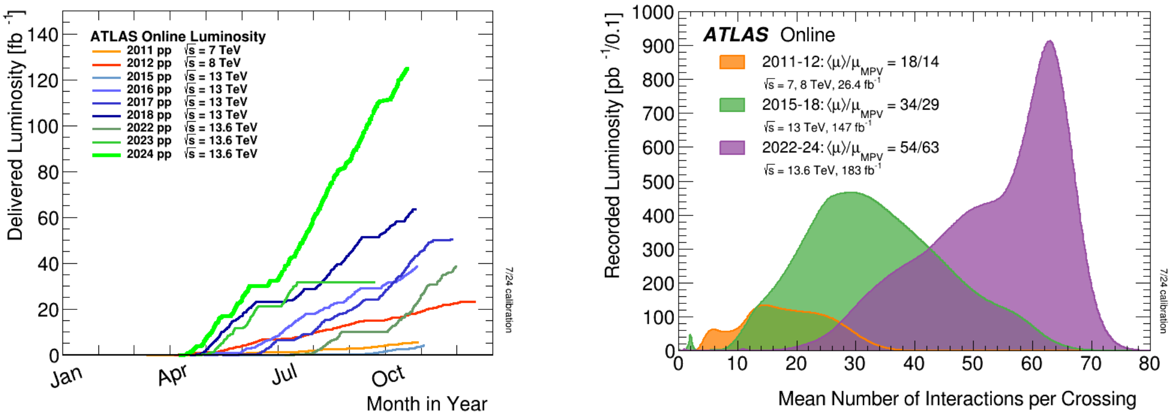

Figure 1.1: Cumulative luminosity delivered to ATLAS as a function of date during stable beams for high-energy pp collisions (left). Luminosity-weighted distribution of the mean number of interactions per bunch crossing (right), with the average $\langle\mu\rangle$ value and most probable μ_{MPV} values indicated inside the figure. Figures taken from Ref.[9].

Run-3 is expected to continue until mid-2026, after which the LHC will enter a Long Shutdown (LS3) to prepare for the High-Luminosity LHC (HL-LHC) phase. The HL-LHC will maintain the same maximum collision energy but increase the luminosity by an order of magnitude. This upgrade involves the installation of stronger focusing magnets, superconducting "crab cavities," enhanced protection systems, and new superconducting transmission lines. ATLAS and CMS will also undergo major detector upgrades to accommodate the higher data rates and radiation levels. The HL-LHC is expected to be operational by 2029 and will run for at least a decade. By the end of its operation, each of the two general-purpose experiments is expected to collect around 3000 fb^{-1} of integrated luminosity, enabling unprecedented precision in measurements and sensitivity to rare processes.

1.2 ATLAS overview

ATLAS (A Toroidal LHC ApparatuS) is one of the two general-purpose detectors at the LHC, designed to explore a wide range of physics—from precision measurements of the Standard Model and studies of the Higgs boson, to searches for phenomena beyond it. The ATLAS collaboration comprises around 6000 scientists and engineers from over 170 institutes across 40 countries, making it a truly global effort. I have been part of ATLAS since the start of my PhD in 2010, contributing to several facets of the collaboration's work. My involvement has spanned from detector design—such as studies on resistive micromegas [10] for the Muon Spectrometer's New Small Wheel—to operations during Run 2, a particularly dynamic period for the Transition Radiation Tracker (TRT), where I was responsible for calibration and tracking software.

The ATLAS detector itself is a massive, multi-layered detector, with a forward–backward symmetric cylindrical geometry and a near 4π coverage in solid angle[2] surrounding one of the LHC's collision points. It consists of concentric subsystems designed to identify and measure particles by tracking their trajectories, determining their momenta and energies, and inferring missing transverse momentum. Charged particles are bent by a magnetic field to enable momentum and charge measurements.

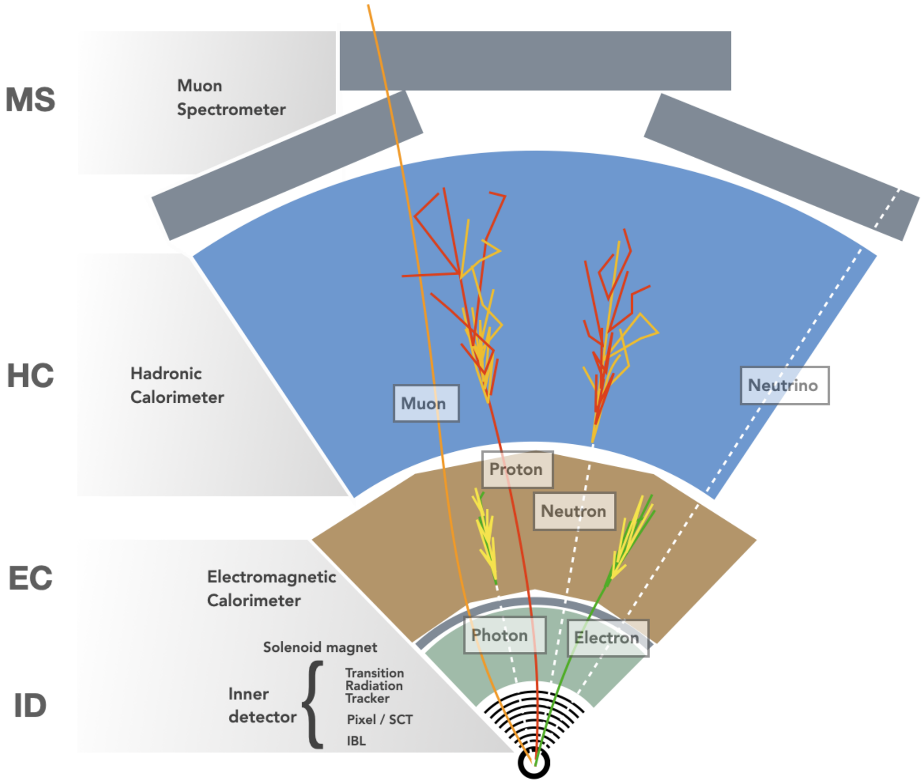

Figure 1.2: Transverse view of the ATLAS detector, showing its different sub-detector systems and the typical signatures of various particles. Muons traverse the entire detector and are identified in the muon spectrometer. Photons and electrons deposit energy in the electromagnetic calorimeter, but only electrons leave a track in the inner detector. Hadrons, such as protons and neutrons, interact with both the electromagnetic and hadronic calorimeters, but only charge particles leave a track in the inner detector. Neutrinos, escape the detector without leaving a direct signature, contributing to missing transverse momentum.

The innermost subsystem is the Inner Detector (ID), dedicated to charged-particle tracking within the pseudorapidity range $|\eta| < 2.5$. Located closest to the interaction point, it operates in an environment of high radiation and particle density. The ID combines three technologies: the pixel detector (including the Insertable B-Layer added before Run2 for improved vertex resolution), the silicon microstrip detector (SCT), and the Transition Radiation Tracker (TRT). The TRT, covering up to $|\eta| < 2.0$, also aids electron

[2] ATLAS uses a right-handed coordinate system with its origin at the nominal interaction point (IP) in the centre of the detector and the z-axis along the beam pipe. The x-axis points from the IP to the centre of the LHC ring, and the y-axis points upwards. Polar coordinates (r, ϕ) are used in the transverse plane, ϕ being the azimuthal angle around the z-axis. The pseudorapidity is defined in terms of the polar angle θ as $\eta = -\ln\tan(\frac{\theta}{2})$.

identification by exploiting differences in transition radiation between electrons and pions. Filled with a xenon gas mixture, the TRT provides electron–pion discrimination through the detection of high-threshold hits. During early Run-2, I contributed to maximizing TRT performance under instantaneous luminosities that exceeded original design parameters, and with a detector suffering of severe gas leakages that forced us to change the gas for some layers. The ID is enclosed in a 2 T solenoidal magnetic field, enabling high-precision momentum measurements, charge identification, and efficient tagging of b-quarks and τ leptons.

Surrounding the ID is the calorimeter system, which measures particle energies via total absorption. It includes electromagnetic (EM) and hadronic (HC) components. The EM calorimeter, based on lead/liquid-argon (LAr) technology, has fine granularity and covers $|\eta| < 3.2$, providing excellent energy measurements for electrons and photons. The hadronic calorimeters use steel/scintillator tiles in the central region ($|\eta| < 1.7$), and copper/LAr modules in the endcaps ($1.5 < |\eta| < 3.2$). The forward calorimeter ($3.2 < |\eta| < 4.9$), employing copper/LAr and tungsten/LAr technologies, ensures energy measurement capability in the very forward regions. The nearly hermetic calorimeter coverage is essential for measuring missing transverse energy and inferring the presence of invisible particles such as neutrinos.

The outermost subsystem is the Muon Spectrometer (MS), which identifies and measures the momentum of muons that penetrate beyond the calorimeters. It covers $|\eta| < 2.7$ and relies on large air-core superconducting magnets producing a toroidal field. It comprises precision tracking detectors (drift tubes and cathode strip chambers), as well as fast trigger chambers: resistive plate chambers (RPCs) in the barrel and thin gap chambers (TGCs) in the endcaps. The combination of inner tracking and muon systems, operating in solenoidal and toroidal fields respectively, allows for precise curvature measurements over long path lengths, enabling accurate charge and momentum reconstruction.

Event selection is handled by a two-level trigger system: a hardware-based first-level trigger reduces the rate to below 100kHz, followed by a software-based high-level trigger that stores approximately 1kHz of physics events. Additional dedicated detectors monitor luminosity and beam conditions, ensuring high-quality data collection.

ATLAS operations rely on an extensive software framework Athena [11] that supports detector control, data acquisition, simulation of detector effects, and reconstruction of both real and simulated events.

Looking ahead, the ATLAS detector will undergo major upgrades to prepare for the HL-LHC era. These include complete replacement of the Inner Detector with an all-silicon Inner Tracker (ITk) will allow robust tracking performance under extreme pile-up conditions. The High Granularity Timing Detector (HGTD), to be installed in the forward region ($2.4 < |\eta| < 4.0$), will provide precise timing information with a resolution of 30 ps per track. This will be critical for mitigating pile-up effects by enabling time-based separation of vertices. The calorimeters and muon systems will also be enhanced with new readout electronics, and the trigger and data acquisition systems are being restructured to cope with the expected data rates. These upgrades are crucial to fully exploit the 3000 fb^{-1} of integrated luminosity anticipated by the end of the HL-LHC program, enabling new levels of precision and sensitivity in the exploration of fundamental physics.

1.3 Object reconstruction and Identification in ATLAS

The reconstruction and identification of physics objects in ATLAS have evolved over time, adapting to detector conditions, the requirements of different analyses and new analysis techniques. This section provides a general overview of how key objects are reconstructed and identified.

Electrons and photons are reconstructed from energy deposits in clusters of cells within the electromagnetic calorimeter [12, 13]. A dynamic cluster-size algorithm [14] allows for energy recovery from bremsstrahlung and photon conversions. For electron reconstruction, these clusters are matched to tracks in the Inner Detector, with track refitting applied when bremsstrahlung is detected. Unconverted photons[3] correspond to clusters without ID tracks, while converted photons are associated with tracks originating from conversion vertices. Recent work, including mine, has contributed to improving the reconstruction of non-primary tracks as part of the inner detector upgrade for the HL-LHC [15]. Electron identification [16] involves multiple variables, such as the shape of the energy cluster in the calorimeter, track quality, and track-to-cluster matching. The charge is determined from the curvature of the associated ID track.

Muons are identified using combined information from the Muon Spectrometer, Inner Detector, and calorimeters. Muons are primarily identified by matching an Inner Detector track with a corresponding track in the Muon Spectrometer [17]. To ensure high-quality reconstruction, muons must have a minimum number of hits in both systems and exhibit consistency in geometrical and momentum matching, taking into account energy loss in the calorimeters. In addition to the standard reconstruction, muons can be identified under special conditions. For instance, if a Muon Spectrometer (MS) track is incomplete but matches an Inner Detector (ID) track, this can occur in regions with limited MS coverage. Conversely, to fully exploit the MS coverage up to $|\eta| < 2.7$, muons with an MS track pointing back to the interaction point but only short ID track segments available are also reconstructed. In cases where an MS track is entirely missing, muons can still be identified by extrapolating ID tracks to the calorimeters and searching for energy deposits consistent with a minimum ionizing particle. Muon charge identification benefits from the fact that muon tracks are less prone to significant distortions compared to electrons, which are affected by bremsstrahlung, or pions, which undergo hadronic interactions. Additionally, the longer lever arm of the Muon Spectrometer provides an independent measurement, helping to reduce charge misidentification compared to electrons. At the analysis level, isolation requirements are often applied to select prompt muons and suppress those originating from jets. This is done by ensuring that no nearby tracks exist within a p_T-dependent variable-size cone, R, around the muon.

For electrons, photons, and muons different identification and isolation working points (ranging from loose to tight) are optimized to maximize background rejection. Stricter selection criteria improve purity by reducing background contamination but come at the cost of lower identification efficiency.

Jets result from the hadronization of quarks and gluons, which cannot exist in isolation due to color confinement. Instead, they hadronize, producing collimated sprays of particles that leave tracks in the Inner Detector and energy deposits in the calorimeters. In ATLAS, the choice of jet reconstruction algorithm depends on the analysis needs: *small*-R jets ($R = 0.4$) [18] are typically used for quark and gluon studies, while *large*-R jets ($R = 1.0$) [19] are used to capture the hadronic decays of boosted massive particles such as W and Z bosons, $h \to b\bar{b}$, and top quarks. Both jet types coexist in an event, and the appropriate choice is made at the analysis level. Jet reconstruction begins with topo-clusters, noise-suppressed calorimeter clusters [14], which are grouped using the anti-k_t algorithm [20]. To mitigate pile-up effects, *small*-R jets undergo simulation-based and *in-situ* calibrations, while *large*-R jets are trimmed [21]. Calibration corrections are then applied to account for detector effects such as non-compensation, dead material, leakage, and out-of-cone effects. Finally, jet substructure techniques—analyzing the angular distribution of energy within the jet—help distinguish hadronic decays of boosted particles from QCD multijet backgrounds, an area of continuous and fast development [22].

[3] A photon conversion is the process where a high-energy photon interacts with matter to produce an electron-positron pair

Missing Transverse Momentum (MET) provides indirect signatures of invisible particles, such as neutrinos. It is reconstructed as the negative vector sum of the momenta of all calibrated objects—electrons, muons, photons, hadronically decaying τ-leptons, and jets—plus a soft term accounting for low-momentum energy not linked to these objects [23, 24]. During Run-2, a track-based soft term was introduced using ID tracks to improve pile-up suppression. Both the choice of input objects and the soft term definition are optimized depending on the analysis to improve MET resolution.

1.4 Boson reconstruction in ATLAS

The bosons studied in this work are extremely short-lived and decay before reaching the ATLAS detector. Their reconstruction thus relies on identifying their decay products, which can produce very different signatures depending on the decay mode.

As shown in Table 1.1, W and Z bosons can decay into either leptons (leptonic decays) or quarks (hadronic decays). For the Higgs boson, Figure 1.3 shows that the dominant decay channel near a mass of 125 GeV is into a pair of bottom quarks ($b\bar{b}$).

Channel	Branching Ratio
$Z \to \ell\ell$	3.3658 ± 0.0023 %
$Z \to \nu\nu$	20.000 ± 0.0055 %
$Z \to q\bar{q}$	69.911 ± 0.0056 %
$W \to \ell\nu$	10.86 ± 0.09 %
$W \to qq'$	67.41 ± 0.27 %

Table 1.1: Decay branching ratios of the gauge bosons considered [25]. The ℓ indicates a type of lepton, either e, μ or τ, not summed over them.

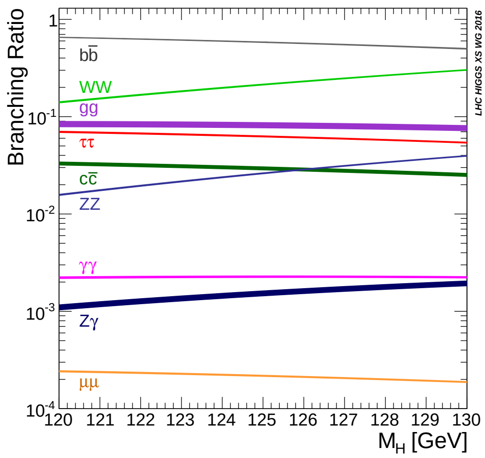

Figure 1.3: Higgs boson branching ratios and their uncertainties for the mass range around 125 GeV [26].

The ability to identify boson decays depends strongly on the type of final state. Leptonic decays, in particular, offer clean experimental signatures. A Z boson decaying to two charged leptons (electrons or muons) can be efficiently reconstructed by selecting opposite-charge, same-flavour lepton pairs and computing their invariant mass. These events are so well-measured that Z bosons are commonly used as standard candles for calibrating electrons [12, 16], muons [17], and jets [27].

Reconstructing W bosons that decay leptonically is more challenging due to the undetected neutrino. However, by combining a high momentum charged lepton with the missing transverse energy of the event, a transverse mass can be computed, which provides a good handle on the W signal. The ability to reconstruct W bosons is demonstrated by the precision of the recent ATLAS measurement of the W mass [28].

Hadronic decays of W, Z, or Higgs bosons are more complex to reconstruct and require different strategies depending on the boson's transverse momentum. In the resolved regime, the decay products are reconstructed as two distinct small-radius jets. In the boosted regime, however, the boson appears as a single large-radius jet with a characteristic two-prong substructure from its two-body decay. In contrast, jets from single quarks or gluons—frequent products of proton-proton collisions—lack this feature. In these cases, jet substructure techniques, often using machine learning algorithms, become essential for identifying the origin of the jet and distinguishing hadronic boson decays [29].

Tagging jets originating from bottom quarks (b-jets) is particularly important in analyses involving Higgs decays, as $H \rightarrow b\bar{b}$ is the dominant channel. The b-jets are distinct from light-quark jets: they tend to produce more particles and frequently involve secondary decays into neutrinos or muons, which are only partially detected. This makes their precise reconstruction challenging. Recently, transformer-based machine learning models have significantly improved the estimation of b-jet transverse momentum, surpassing traditional calibration methods [22]. These models also predict the jet mass, enhancing the ability to distinguish Higgs decays. Figure 1.4 illustrates how large-radius jets from various processes—including Z and Higgs decays to b-quarks—can be separated using these improved techniques.

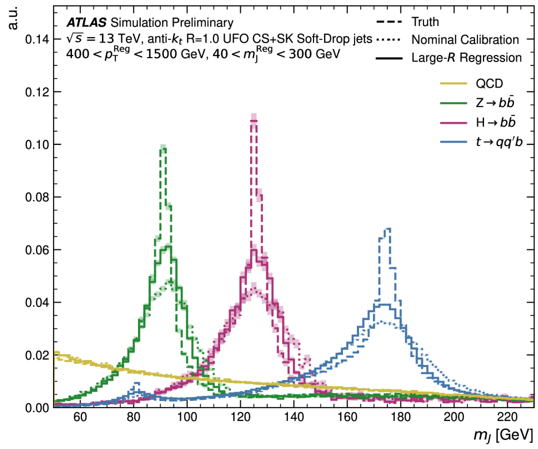

Figure 1.4: Mass distribution of large-radius jets originating from different processes: $Z \rightarrow b\bar{b}$ (green), $H \rightarrow b\bar{b}$ (magenta), top-quark decays (blue), and non-resonant $b\bar{b}$ production (yellow). Taken from [22].

Most of my research has focused on analyses involving leptonic decays of W and Z bosons. However, given the larger branching fractions of hadronic modes, future projects—such as those aiming to probe rare processes like di-Higgs production—will increasingly benefit from improved jet tagging techniques and boosted boson reconstruction.

2 Beyond the Particle Zoo: Probing the Standard Model Through Diboson Interactions

"The big book of Nature is written in a mathematical language¨

— Galileo Galilei, *Il Saggiatore*

The quest for a consistent framework to describe the fundamental forces governing the smallest constituents of matter has led to the construction of the Standard Model of particle physics. This theoretical framework, grounded in symmetry principles and experimental evidence, provides a consistent description of the known elementary particles and their interactions.

In the Standard Model, each particle is represented by a quantum field characterized by intrinsic properties such as spin, charge, and mass. Matter is made up of fermions—spin-$\frac{1}{2}$ particles—while the fundamental forces are mediated by spin-1 bosons: the photon (γ), gluons (g), and the weak bosons ($W^{\pm}$, Z). The model also includes a spin-0 scalar field: the Higgs boson, that plays a crucial role in the generation of particle masses.

Beyond listing the particles in this "Zoo," one of the Standard Model's major achievements is its ability to make precise predictions about how these particles interact with each other. Testing these predictions through experimental measurements allows us to probe the consistency of the theory—and potentially reveal where it breaks down.

In this chapter, I focus on a particular class of processes—diboson interactions—which provide unique sensitivity to the dynamics of electroweak symmetry breaking (EWSB). But before diving into the measurements, it's helpful to briefly revisit the theoretical foundations that make these processes relevant to probe the Standard Model.

At the heart of the Standard Model lies the principle of *local gauge invariance*, which requires that physical laws remain unchanged under transformations that vary from point to point in space-time. While individual quantum fields transform under these operations, measurable physical quantities remain unchanged, this property is known as *gauge invariance* or *gauge symmetry*. Enforcing this symmetry leads naturally to the introduction of gauge bosons: the force carriers. The interactions among them are governed by the symmetry group $SU(2)_L \otimes U(1)_Y \otimes SU(3)_C$ [30–32], associated respectively with the weak, electromagnetic, and strong forces. Each symmetry corresponds to a conserved quantum number: weak isospin, hypercharge, and color charge.

Matter fields—quarks and leptons—transform under these symmetries according to their quantum numbers. Quarks, which carry color charge are triplets under $SU(3)_C$, while leptons are singlets. Both quarks and leptons come in three families, each with identical gauge quantum numbers but different masses. Within each family, particles are organized into doublets, and they differ by their electric charge, so there are up- and down-type quarks (u, d), as well as neutrinos and charged leptons (ν, ℓ).

Curiously, interactions with the $SU(2)_L \otimes U(1)_Y$ fields depend on the helicity[1] of the fermions: only left-handed doublets are charged under $SU(2)_L$. This fundamental asymmetry, was introduced in the Standard Model to align with experimental observations [33] and makes gauge interactions in the Standard Model *chiral*[2]. This has profound consequences in the predictions such as the maximal violation of parity in weak interactions and it forbids the generation of particle masses through conventional means without breaking gauge symmetry.

The solution to this apparent contradiction came with the Higgs mechanism, proposed independently by Higgs, Brout, Englert, Guralnik, Hagen, and Kibble in the 1960s [34–36]. By introducing a scalar field with a non-zero vacuum expectation value, the theory allows gauge bosons and fermions to acquire mass via spontaneous symmetry breaking, without sacrificing gauge invariance. After EWSB, the hypercharge and isospin fields mix, producing the mediators of the electromagnetic and weak interactions: the massless photon (γ) and the massive weak bosons ($W^{\pm}$ and Z). Fermions acquire mass through Yukawa-type interactions with the scalar field. The remaining physical component of this field is the Higgs boson, the last particle added to the Particle Zoo. The Higgs Mechanism thus establishes a profound connection between the gauge bosons and the Higgs boson, intertwining their properties and interactions in a way that is fundamental to the structure and predictions of the Standard Model.

The discovery of the Higgs boson in 2012 confirmed the Higgs mechanism, but many fundamental questions remain. Is the mechanism responsible for EWSB exactly as described in the Standard Model, or merely an effective approximation? The origin of EWSB is one of the most compelling open questions in particle physics, closely tied to others: the structure of the early Universe, the matter-antimatter asymmetry, the origin of neutrino masses, and the observed hierarchies and patterns in fermion masses and mixings.

These questions sit at the heart of contemporary research in particle physics, and their answers are intimately linked to the nature of the Higgs boson and the dynamics of the scalar sector. In particular, the longitudinal components of the W and Z bosons—related via the Equivalence Theorem to the Nambu-Goldstone bosons "eaten" during EWSB—provide a powerful probe into this sector. Measuring the interactions of these longitudinally polarized bosons, and of the Higgs boson itself, is key to testing the inner workings of the Standard Model.

This is where diboson processes come in. To maintain gauge invariance, the weak force carriers must not only interact with matter but also with one another. These self-interactions—triple and quartic gauge couplings (TGCs and QGCs)—are precisely predicted by the Standard Model. At the LHC, multiboson production processes allow us to test these predictions. For example, vector boson scattering (VBS) processes, though rare, are sensitive at tree level to both TGCs and QGCs. They also offer access to interactions involving longitudinally polarized bosons, which are central to EWSB dynamics.

While inclusive diboson production is mostly sensitive to triple gauge couplings, its much higher rate at the LHC—nearly ten times that of VBS—makes it particularly well-suited to studying polarization. Although these processes are dominated by transverse modes, precision measurements and modern analysis techniques are beginning to isolate the longitudinal components. Ultimately, di-Higgs production will provide access to the Higgs self-coupling and gauge-Higgs couplings, closing the loop on direct tests of the scalar sector.

[1] Helicity is the sign of the projection of the spin vector onto the momentum vector: "left" is negative, "right" is positive.
[2] An object or a system is chiral if it is distinguishable from its mirror image.

Thanks to the LHC's unprecedented energy and luminosity, many of these processes—previously out of reach—are now accessible. In particular, VBS and the production of two longitudinally polarized bosons were not established before the LHC Run-2.

In the sections that follow, I present an overview of recent experimental results on Vector Boson Scatering and Vector Boson Polarization, with a particular focus on the contributions I have made to these efforts. My work has centered on the WZ and same-sign $W^{\pm}W^{\pm}$ channels, in collaboration with many colleagues from ATLAS and the theory community. Most of the studies covered in this Chapter were carried out during my postdoctoral fellowship in Dresden, in collaboration with Michael Kobel and Frank Siegert, when we supervised a talented group of students and early-career researchers: Franziska Iltzsche, Carsten Bittrich, Stefanie Todt, Anna Tegetmeier, Tim Herrmann, Max Stange, and Jan-Eric Nitschke.

Together, we contributed to multiple facets of these analyses: theoretical interpretation, Monte Carlo simulations, event selection optimization, data-driven background estimation, theory uncertainty evaluation, and statistical analysis. The richness of diboson measurements lies not only in the exciting physics they explore, but also in the wide range of experimental and theoretical tools they require. It has been a privilege to work with this group and help push the boundaries of what we can measure. So let's dig in!

2.1 Vector Boson Scattering

The scattering of vector bosons, known as Vector Boson Scattering (VBS), is one of these rare processes that allow us to probe two fundamental aspects of the Standard Model simultaneously. On one hand, VBS directly tests gauge interactions, as it is one of the few processes with tree-level sensitivity to quadrilinear (or quartic) gauge couplings. On the other hand, it probes the mechanism of electroweak symmetry breaking, as it is sensitive to the couplings between the Higgs boson and gauge bosons at energy scales that can significantly differ from the Higgs mass. At the LHC, protons act as a source of vector boson beams. This occurs when incoming quarks from the protons radiate heavy gauge bosons, which can subsequently interact with each other. Figure 2.1 shows a simplified picture of a proton-proton collision event leading to vector boson scattering.

According to the Standard Model, vector boson scattering proceeds through two main types of diagrams: those involving gauge couplings triple or quartic, and those mediated by a Higgs boson exchange (see the bottom part of Figure 2.1). Without including all these contributions, the predicted scattering cross-section increases indefinitely with energy, violating the fundamental principle of probability conservation, known as unitarity. As an example, Figure 2.2 illustrates the predicted cross-section for longitudinal $W^{+}W^{-} \to W^{+}W^{-}$ scattering considering subsets of the contributing tree-level diagrams [37]. The unphysical rise in the cross-section at high energies (red and yellow lines) clearly demonstrates that considering individual contributions, or an incomplete subset, leads to a violation of unitarity. However, it is also very interesting to see that only when all the contributions from different types of interactions are included (green line), the growing behavior cancels out, ensuring a physically consistent prediction.

One might argue that these distributions were primarily interesting before the discovery of the Higgs boson. Now that we know the Higgs exists, and that its measured couplings align with Standard Model predictions within experimental uncertainties, their relevance may seem reduced. But there is more to learn here! Vector Boson Scattering processes are really a window to EWSB sector, these interactions provide unique access to the high-energy behavior of Higgs couplings, specifically at energy scales beyond the Higgs' rest mass. This measurements are particularly sensitive to potential modifications in the Higgs sector,

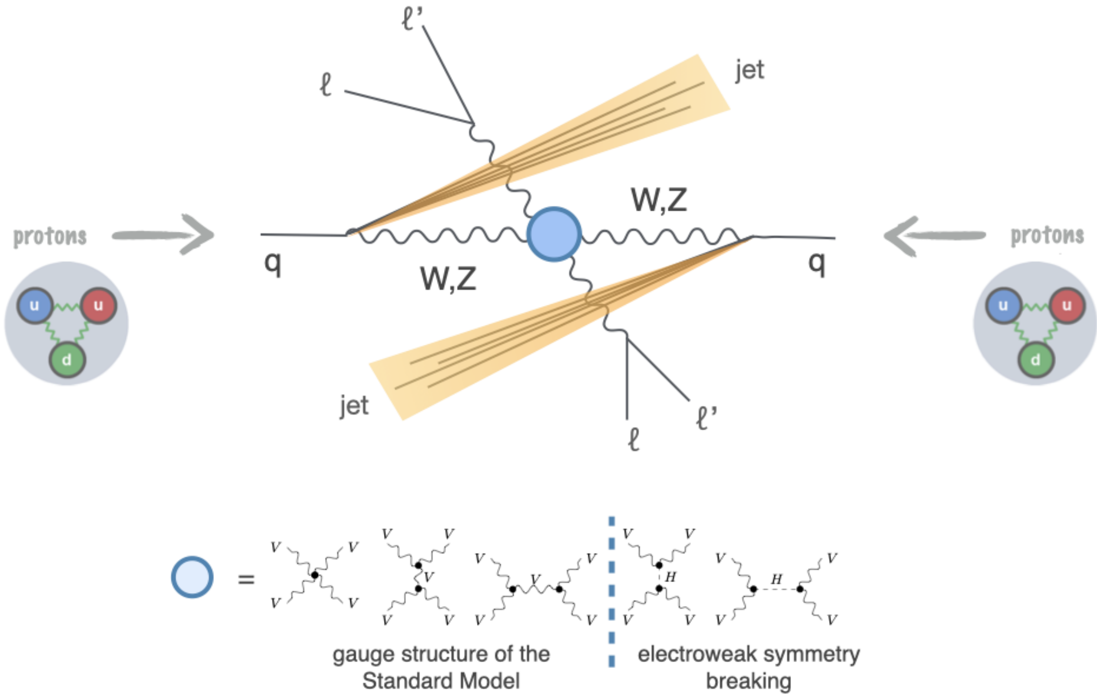

Figure 2.1: A simplified picture of a proton-proton collision event resulting in the scattering of two vector bosons. The blue circle in the middle illustrate the possible exchanges between the bosons at leading order, those include triple and quartic gauge bosons vertices which makes this processes sensitive to the gauge structure of the SM, as well as the exchange of a Higgs boson which makes the process sensitive to the EWSB.

including deviations in cubic and quartic gauge couplings. Given the intricate cancellations between the contributing diagrams even minor departures from Standard Model predictions could manifest as apparent unitarity violations in scattering amplitudes. While unitarity must ultimately be preserved in nature (as a fundamental requirement of quantum field theory), any observed discrepancy between measured VBS cross-sections and SM predictions at high energies would reveal limitations in our current understanding of the EWSB, pointing to the existence of new physics (e.g., additional Higgs-like states or strong dynamics) acting as unitarity-restoring mechanisms.

2.1.1 Signal Definition in a VBS Measurement

We have established that studying VBS at high energies is crucial to test the EWSB sector. However, before performing a VBS measurement, we must first clearly define what can actually be measured, and this seems not to that evident in VBS. From an experimentalist perspective, a scattering process at the LHC is defined by its measured final state, which consists of detector signals put together into physics objects such as leptons, photons, particle jets or missing transverse momentum from neutrinos, using

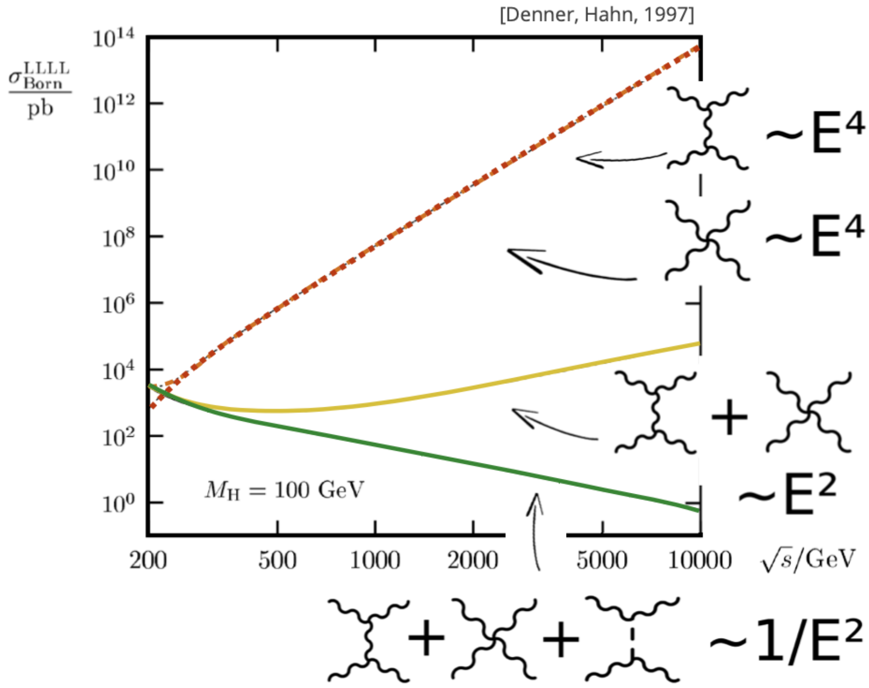

Figure 2.2: The cross-sections for longitudinal $W^+W^- \to W^+W^-$ scattering resulting from subsets of the tree-level diagrams: in red diagrams involving either triple-gauge-boson or quartic-gauge-boson couplings, in yellow diagrams involving both triple and quartic-gauge-boson couplings, and in green diagrams involving Higgs bosons as well as triple and quartic-gauge-boson couplings. Adapted from Ref. [37].

this objects signal-enriched phase-space regions are built upon applying specific kinematic cuts. From a theoretical point of view, a scattering process is defined through its external particles, similar to the experimental definition but it is also aware of the strong and electroweak interactions that take place in the transition between the initial and final states. In the case of VBS, as we discussed so far, the theoretical and experimental definitions partially overlap.

What does this partial overlap mean? Measuring VBS at the LHC requires identifying events with two electroweak (vector) bosons (V) accompanied by two outgoing quarks. Due to color confinement, the quarks hadronize into sprays of particles known as jets (j), leading to a $VVjj$ final state, with the vector bosons decaying into their respective channels. In theoretical calculations at tree level, to connect the initial state protons (or rather, the quarks and gluons) to the $VVjj$ final state, one can categorize the contributions into two groups: those involving only electroweak interaction vertices (denoted "$VVjj$-EW") and those containing at least one strong interaction vertex (denoted "$VVjj$-QCD"). In experimental data, both $VVjj$-EW and $VVjj$-QCD contributions are present. However, within $VVjj$-EW, the VBS diagrams of interest coexist with other electroweak processes that cannot be separated in a gauge-invariant way. Consequently, due to the nature of proton-proton collisions, a direct measurement of the VBS cross-section alone is not possible for comparison with the theoretical predictions, like the ones shown in Figure 2.2. Instead, experimental analyses are designed to exploit the theoretical knowledge to define phase-space regions where the VBS contribution is enhanced. As a result, the measured signal is not purely VBS but rather the broader $VVjj$-EW category. But this is not the end of the story, to understand better what is included in each contribution, let's examine them in more detail.

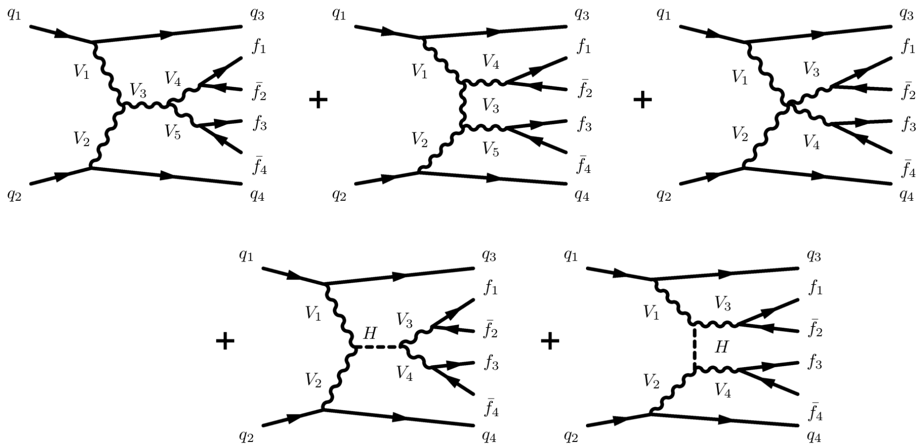

Figure 2.3: Representative diagrams for $VVjj$-EW production where two electroweak gauge bosons are radiated off quarks and interact. The top row shows (from left to right) the interactions via triple gauge vertices the s-channel and the t-channel exchanges, and the quartic gauge vertex. The bottom row illustrates the exchange of a Higgs boson in the s-channel (left) and t-channel (right). Quarks (q), vector bosons ($V = W, Z$), and fermions (f) are labeled accordingly. Figure taken from Ref. [5].

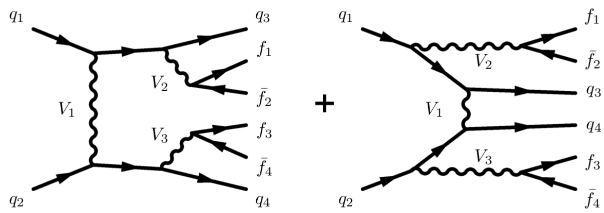

Figure 2.4: Representative diagrams for $VVjj$-EW production where two electroweak gauge bosons are radiated off quarks without gauge boson self interactions. Figure taken from Ref. [5].

The electroweak production ($VVjj$-EW) at leading-order (LO) includes the diagrams with vector boson scattering that we are interested in, but is not limited to them; there are also electroweak-induced processes where the radiated vector bosons do not interact. Thus we can say the electroweak production has two components: the EW VBS production, where two electroweak bosons genuinely scatter, as illustrated in Figure 2.3, and the EW non-VBS production, which also involves electroweak vertices but without boson-boson scattering, as illustrated in Figure 2.4. These purely electroweak contributions are both at order $O\left(\alpha^6\right)$ when including the decay products of the heavy gauge bosons into the counting. A key point here is that the EW non-VBS component cannot be separated from the EW VBS component in a gauge-invariant way. Selecting only specific diagrams would break theoretical consistency.

Another purely electroweak contribution that also leads to the same $VVjj$ final state is the triboson production (VVV), where one of the bosons decays hadronically. These processes can be gauge-invariantly distinguished from the $VVjj$-EW contribution, and are easy to remove experimentally since the resonant decay of a boson into two quarks can be suppressed by imposing a requirement on the invariant mass of the quark pair. As a result, triboson contributions are significantly reduced in the experimental analysis.

The QCD-mediated production, $VVjj$-QCD, as illustrated in Figure 2.5 is then considered as background. This process involves electroweak vertices as well as at least one strong interaction vertex, with contributions of order $O\left(\alpha_s^2\alpha^4\right)$. An important distinction of $VVjj$-QCD processes, compared to $VVjj$-EW-induced ones, is the presence of QCD exchanges between the quark lines, commonly referred as a color connection

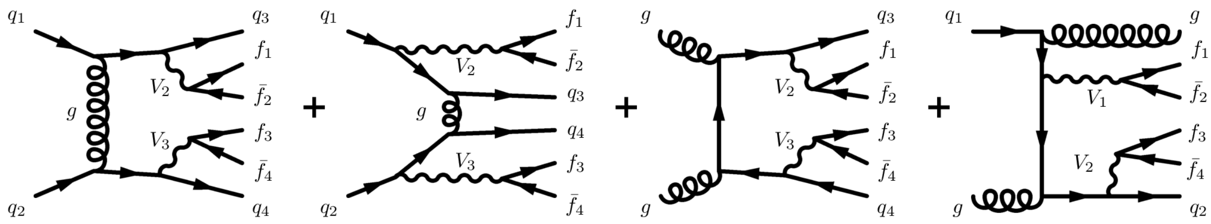

Figure 2.5: Representative diagrams for $VVjj$-QCD production where two electroweak gauge bosons are radiated off quarks, the contributing diagrams involve both electroweak and strong interactions without gauge boson self interactions. Figure taken from Ref. [5].

or color-flow. This feature is particularly useful for distinguishing the EW signal from the QCD background due to their kinematic differences.

Due to the quantum-mechanical nature of the process, the $VVjj$-QCD and $VVjj$-EW contributions interfere at $O(\alpha_s\alpha^5)$ at LO. The classification of the $VVjj$-interference contribution as either signal or background is inherently ambiguous, as it involves both amplitudes, making its treatment an arbitrary choice in experimental analyses. Some analyses have included this interference in the fit, floating with the signal, while others have accounted for it only as an uncertainty. The interference term was found to be small for the fitted distributions, with a very limited impact on the results. However, its treatment already highlights the limitations of this signal definition, and the ambiguity worsens at Next-to-Leading-Order (NLO). At this order, separating contributions that contain only one type of amplitude (EW or QCD) becomes even more cumbersome due to significant mixed-type NLO corrections [38].

Returning to the question of what can be experimentally measured when looking for VBS, the ATLAS analysis has been optimized with specific kinematic cuts to enhance the LO $VVjj$-EW component. However, since separating pure EW and QCD contributions is not possible at NLO [38–41], measurements that define $VVjj$-EW as the signal necessarily rely on theoretical inputs and their approximations to built the signal enriched phase space and to separate signal from background. To maximize model independence, in addition to the $VVjj$-EW measurement, inclusive $VVjj$ cross sections,without subtracting as backgrounds the $VVjj$-QCD or triboson contributions, are now days also published as part of the result.

2.1.2 Current Status of Theory Calculations: VBS at Next-to-Leading Order

Theoretical predictions are essential for VBS measurements, as they enable experimental analyses to define signal-enriched phase-space regions and disentangle the $VVjj$ QCD and EW components. While Run-2 results remain limited by statistical uncertainties, theory and modeling uncertainties already contribute significantly, accounting for about one-third of the total uncertainty in these measurements. With the Run-3 data, statistical uncertainties will decrease significantly, and the precision of $VVjj$-EW measurements is expected to reach just a few percent. To achieve this level of accuracy, next-to-leading order corrections are needed for a robust theoretical description of $VVjj$ processes.

In the previous section, we discussed that Run-2 VBS analyses treated the LO $VVjj$-EW contribution ($O\left(\alpha^6\right)$) as signal and the $VVjj$-QCD contribution ($O\left(\alpha_s^2\alpha^4\right)$) as background. However, the treatment of the EW-QCD interference term ($O\left(\alpha_s\alpha^5\right)$) remained ambiguous: some analyses included it in the signal fit, while others considered it solely as an uncertainty on the signal or even as part of the background. At NLO, defining the signal becomes even more complicated, as significant mixed-type EW-QCD contributions appear. Figure 2.6 shows the contributing perturbative orders of the $VVjj$ calculations at LO and NLO at the LHC. Four different orders enter the complete NLO calculation of the $VVjj$ process: At order $O(\alpha^7)$, only the NLO electroweak corrections to the $VVjj$-EW process enter. The order $O(\alpha_s^3\alpha^4)$ solely receives contributions from the QCD corrections of the $VVjj$-QCD process. For the remaining two orders, $O(\alpha_s\alpha^6)$ and $O(\alpha_s^2\alpha^5)$, a simple separation between the electroweak and strong production mode is no longer possible, as these orders receive contributions from at least two LO contributions. Hence, only the orders $O(\alpha^7)$ and $O(\alpha_s^3\alpha^4)$ can unambiguously be assigned to a given tree-level process. Separating contributions that contain only one type of amplitude (EW or QCD) is no longer possible without leaving behind some contributions [38].

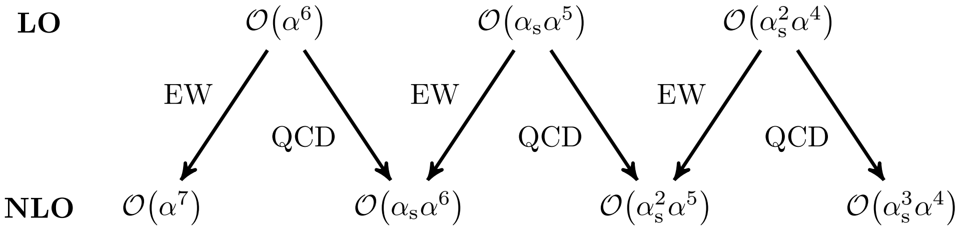

Figure 2.6: Contributing perturbative orders of the $VVjj$ calculations at LO and NLO at the LHC. Figure taken from Ref [38].

Including NLO corrections to $VVjj$ processes is challenging, as only complete calculations at fixed orders of $\alpha_s^n\alpha^m$ are strictly well-defined. A comprehensive discussion of the difficulties associated with a full NLO calculation can be found in Ref. [38], but I would like to highlight some of the key challenges here.

First, $VVjj$ processes already exhibit high dimensionality at leading order. When accounting for vector boson decays, the process involves six final-state particles, and real-emission corrections introduce a seventh, further increasing the complexity. Virtual corrections also contribute significantly, particularly in the case of electroweak corrections. For example, an additional gauge boson can connect the two quark lines or even interact with the decay products of the outgoing vector boson. As a result, loop diagrams with up to eight internal vertices arise, pushing the limits of state-of-the-art computational tools.

Moreover, diagrams featuring corrections to the Higgs, the triple or quartic gauge boson self-interaction appear, either by loops involving gauge bosons or heavy fermions. Additionally, due to the intricate color structure of the purely electroweak process at LO, including QCD loop corrections could alter the overall structure of the process. Depending on the final-state bosons, some contributing diagrams may vanish, leading to different levels of complexity across various $VVjj$ channels.

Despite these challenges, several approximations have been developed and are widely used by the theory community to manage the complexity and compute partial NLO contributions, among them:

- VBS Approximation: Focuses on t- and u-channel diagrams, neglecting interferences and s-channel contributions [40, 42–44].
- VBS Approximation + s-Channel: Adds the s-channel squared matrix element ($|t|^2 + |u|^2 + |s|^2$) to the VBS approximation. Interferences are still neglected [45, 46].
- Discarding Non-Factorisable QCD Corrections: Considers all real emission contributions with interferences but includes only factorisable virtual corrections. Neglects virtual corrections that connect the incoming quark lines [47].

- Double Pole Approximation: Requires exchanged vector bosons to be resonant, neglecting non-resonant contributions [48].
- Effective Vector Boson Approximation: Vector bosons radiated off the quarks in collinear limit [49].

With the help of these approximations, next-to-leading-order calculations in QCD and electroweak theory are now available for $VVjj$-EW processes. However, these results remain approximations, since they might exclude certain higher-order contributions or off-shell effects, depending on the approximations used. Their validity and precision depend on the specifics of the final state and the fiducial phase-space definitions.

A detailed overview of the NLO QCD calculations for $VVjj$-EW at $O(\alpha^6\alpha_s)$ at $\sqrt{s} = 13$ TeV is available in Ref. [50]. Table 2.1 presents the leading-order and NLO QCD cross sections computed under the VBS approximation, along with the corresponding k-factors, defined as the ratio between the NLO and LO cross sections, $k = \sigma_{\mathrm{NLO}}/\sigma_{\mathrm{LO}}$. For purely leptonic VBS processes, the k-factors remain below 10%, while semi-leptonic channels exhibit corrections of up to 20%. These fixed-order calculations employing the VBS approximation have also been matched with parton showers using the PowhegBox Monte Carlo generator [51–53]. Parton shower effects lead to moderate changes in normalization and kinematic distributions compared to the fixed-order NLO QCD results.

Recently, additional Monte Carlo generators have been used for similar studies, particularly in $W^{\pm}W^{\pm}jj$-EW final states [41]. Programs such as VBFNLO and MadGraph5_aMC@NLO offer alternative approaches and can be interfaced with Pythia 8 or Herwig 7 using the Matchbox framework [54, 55]. Although these methodologies introduce different approximations, they have not yet been incorporated into experimental analyses.

Electroweak NLO corrections at $O(\alpha^7)$ introduce significant effects on cross sections and the shapes of kinematic distributions. In $W^{\pm}W^{\pm}jj$ scattering, such corrections reduce the total cross-section by up to 16% and have an even larger impact on high-energy tails due to Sudakov logarithms [56]. These modifications arise from the fundamental structure of the process at the LHC rather than specific selection criteria [50, 56]. Recent studies [38, 57, 58] have presented complete NLO calculations, incorporating all relevant orders. The findings confirm that $O(\alpha^7)$ effects dominate across multiple VBS final states. A notable advancement in this area is the automated implementation of full fixed-order NLO calculations within Sherpa using the Recola matrix-element generator.

The simulation tools used for the ATLAS Run-2 result limited the signal accuracy to leading-order, nevertheless experimental analysis accounted for shape effects on the signal due to NLO QCD and EW corrections by using differential k-factors or in some cases by using truth level simulation from the PowhegBox generator. The large modeling uncertainties in the Run-2 results are due in part to this NLO uncertainties.

2.1.3 VBS Event Topology and Signal Region Definition

The ATLAS measurements are performed in $VVjj$-EW signal-enriched phase-space regions. These signal regions are defined and optimized in each analysis depending on the nature of the backgrounds and the size of the $VVjj$-QCD contribution. Nevertheless, all of the VBS analyses exploit the distinct kinematic features of VBS topology [59].

In hadron collisions, quarks radiating gauge bosons undergo only slight deflections, resulting in two forward-scattered jets, known as tagging jets, which are typically observed on opposite sides of the detector.

Process	σ_{LO}	σ_{NLO}	$k = \sigma_{\text{NLO}}/\sigma_{\text{LO}}$
$pp \to HHjj$ ("VBF-HH")	0.60364(12) fb	0.5613(4) fb	0.93
$pp \to \ell_1^+ \nu_{e_1} \ell_2^- \bar{\nu}_{e_2} jj$ ("VBS-W$^+$W$^-$")	22.691(13) fb	22.30(4) fb	0.98
$pp \to \ell_1^+ \ell_1^- \ell_2^+ \ell_2^- jj$ ("VBS-Z$_\ell$Z$_\ell$")	228.90(16) fb	234.0(7) fb	1.02
$pp \to \ell_1^+ \ell_1^- \nu_2 \bar{\nu}_2 jj$ ("VBS-Z$_\ell$Z$_\nu$")	1.5654(9) fb	1.581(4) fb	1.01
$pp \to \ell_1^+ \nu_{e_1} \ell_2^+ \ell_2^- jj$ ("VBS-W$^+$Z")	1.7056(7) fb	1.679(2) fb	0.98
$pp \to \ell_1^- \bar{\nu}_{e_1} \ell_2^+ \ell_2^- jj$ ("VBS-W$^-$Z")	0.9164(3) fb	0.9424(9) fb	1.03
$pp \to \ell_1^+ \nu_{e_1} \ell_2^+ \nu_{e_2} jj$ ("VBS-W$^+$W$^+$")	5.7321(17) fb	5.616(4) fb	0.98
$pp \to \ell_1^- \bar{\nu}_{e_1} \ell_2^- \bar{\nu}_{e_2} jj$ ("VBS-W$^-$W$^-$")	1.7388(5) fb	1.8785(18) fb	1.08
$pp \to \ell^+ \nu q \bar{q} jj$ ("VBS-W$^+$Z$_{had}$")	21.075(17) fb	23.44(9) fb	1.11
$pp \to \ell^+ \ell^- q \bar{q} jj$ ("VBS-Z$_\ell$Z$_{had}$")	2.186(3) fb	2.455(19) fb	1.12
$pp \to q \bar{q} \ell^+ \ell^- jj$ ("VBS-W$^+_{had}$Z$_\ell$")	2.0880(10) fb	2.304(4) fb	1.10
$pp \to \ell^+ \nu q \bar{q} jj$ ("VBS-W$^+$Z$_{had}$")	9.046(5) fb	9.71(2) fb	1.07
$pp \to q \bar{q} \ell^+ \ell^- jj$ ("VBS-W$^-_{had}$Z$_\ell$")	1.0516(5) fb	1.1991(19) fb	1.14
$pp \to \ell^- \bar{\nu} q \bar{q} jj$ ("VBS-W$^-$Z$_{had}$")	4.670(2) fb	5.347(11) fb	1.14
$pp \to q \bar{q} \ell^+ \nu jj$ ("VBS-W$^+_{had}$W$^+$")	13.942(5) fb	14.960(15) fb	1.07
$pp \to q \bar{q} \ell^- \bar{\nu} jj$ ("VBS-W$^+_{had}$W$^-$")	3.9314(15) fb	4.685(7) fb	1.19

Table 2.1: Integrated cross sections for various VBF and VBS processes at the LHC with a center-of-mass energy of 13 TeV. The values in parentheses indicate statistical errors from Monte Carlo integration. Data sourced from Ref. [50].

A large dijet invariant mass (M_{jj}) and a wide rapidity separation (ΔY_{jj}) between these jets are expected, providing the signal with a clear experimental signature. Figure 2.7 presents the leading-order differential cross sections obtained with MADGRAPH for the $W^{\pm}W^{\pm}jj$ signal, illustrating the discrimination power of the VBS topology to separate the signal $W^{\pm}W^{\pm}jj$-EW (EW6 in the figure) from suppress the $W^{\pm}W^{\pm}jj$-QCD (EW4 in the figure) contribution.

Another commonly exploited feature is the reduced hadronic activity in the rapidity gap between the tagging jets, which serves as a key distinction between $VVjj$-EW and $VVjj$-QCD. The EW process, which lacks color exchanges between the quark lines, exhibits a characteristic topology with minimal activity in this region, whereas the QCD component, involving such exchanges, tends to populate it. As a result, these two contributions dominate different phase-space regions, leading to distinct differential cross-section distributions. To enhance signal purity, some analyses veto events with additional jets between the tagging jets, requiring $N_{\text{gap jet}} = 0$. Another way to quantify the position of the additional jets (or other particles) relative to the tagging jets is through the centrality variable, introduced in [59]. Centrality is typically defined using the difference in (pseudo-)rapidity between a measured particle and the tagging jets.

The diboson system itself also provides useful characteristics for discriminating VBS events. For instance, the vector bosons produced in the scattering process are typically located between the tagging jets. In this case, the centrality variable, now defined using the decay products of the vector bosons, becomes a useful discriminant.

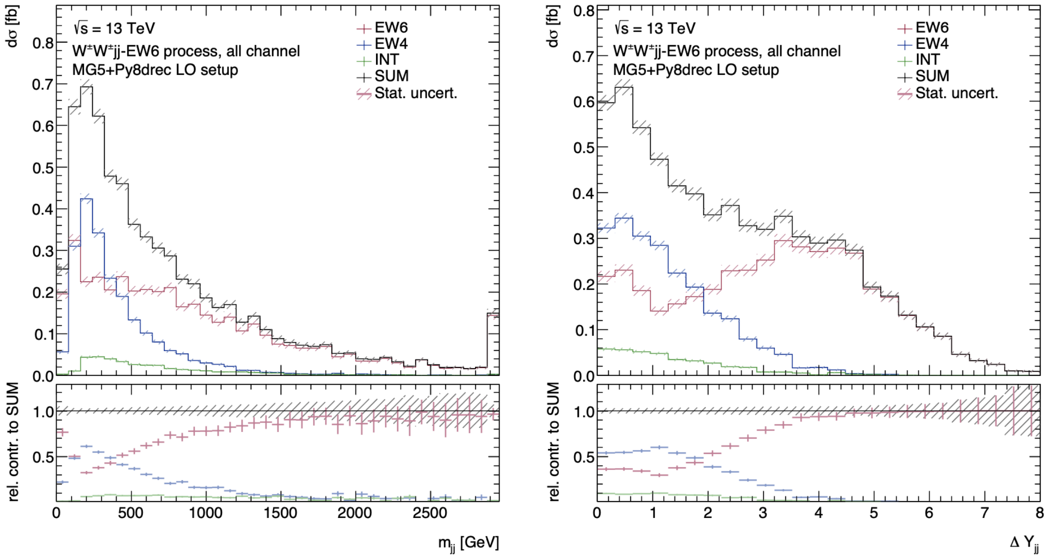

Figure 2.7: Kinematic distributions comparing the leading-order contributions of the $W^{\pm}W^{\pm}jj$ process, the electroweak and the QCD production, and its interference, labelled EW6, EW4, and INT, respectively. The sum of all contributions is also shown, labelled as SUM. The invariant mass mjj (left) and rapidity separation $|\Delta Y_{jj}|$ (right) of the tagging jet system. The lower panel shows the relative contribution with respect to the sum. Uncertainties are statistical uncertainties from the MC generation only. Figure taken from [60].

Figure 2.8 illustrates a simplified picture of vector boson scattering and its subsequent leptonic decay, the tagging jets appear in the forward and backward regions of the detector, while the electroweak gauge bosons are located in between them. Additionally, new resonances may be produced as intermediate states when two electroweak gauge bosons fuse. The properties of the observed diboson system are therefore influenced by the nature of these intermediate resonances.

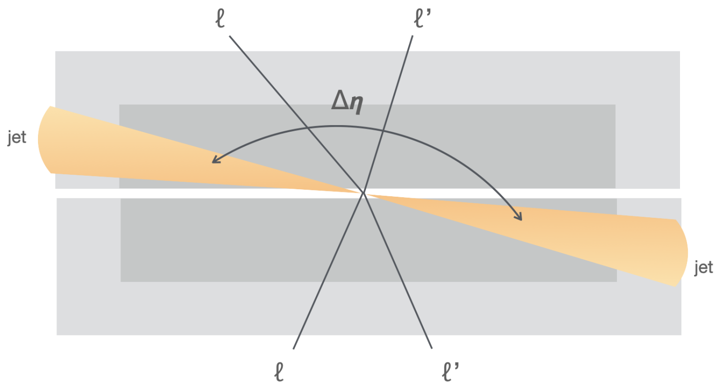

Figure 2.8: Schematic view of a VBS event as observed in a detector. The two tagging jets are shown in yellow, positioned in opposite hemispheres of the detector. The leptons as black lines, are representing the decay products of the bosons, are located between the tagging jets.

Finally, another non-VBS process that can lead to a $VVjj$ final state is triboson production (VVV), where one of the bosons decays hadronically. This purely electroweak $VVjj$-EW contribution can be effectively suppressed in the signal region by applying an invariant-mass requirement on the decay products of the hadronically decaying boson [41].

By applying constraints to standard observables such as the VBS jets invariant mass, rapidity separation between the VBF jets, and centrality, a phase space enriched with VBS events can be defined, significantly suppressing the QCD-induced $VVjj$ background. For instance, Table 2.2 presents the fiducial cross-sections for the electroweak and QCD-induced $VVjj$ processes within a typical VBS analysis phase space.

This includes imposing additional criteria like an invariant mass requirement of $M_{jj} > 500$ GeV and a pseudo-rapidity gap of $|\Delta\eta_{jj}| > 2.4$, along with basic selection cuts on the vector boson decay products and kinematic restrictions on the jets. The table's final column displays the ratio of the fiducial cross-sections for $VVjj$-EW to $VVjj$-QCD production. It can be seen that the QCD-induced $VVjj$ cross-section is of the same order of magnitude as the EW processes across most final states. However, an exception arises in the case of final states involving two same-sign leptons, which are particularly sensitive to the scattering of same-charge $W^\pm$ bosons ($W^\pm W^\pm \to W^\pm W^\pm$) were the QCD induced contribution is largely suppressed.

Final state	VBS channel	$\sigma_{VVjj\text{-EW}}$ [fb]	$\sigma_{VVjj\text{-QCD}}$ [fb]	$\frac{\sigma_{VVjj\text{-EW}}}{\sigma_{VVjj\text{-QCD}}}$
$\nu_e\nu_e\nu'_\ell\nu'_\ell jj$	$ZZjj$	1.68	1.38	1.22
$\ell^\pm\nu_e\nu'_\ell\nu'_\ell jj$	$W^\pm Zjj$	7.64	15.5	0.49
$\ell^\pm\nu_\ell\ell'^\pm\nu'_\ell jj$	$W^\pm W^\pm jj$	3.97	0.346	11.5
$\ell^\pm\ell^\mp\nu_\ell\nu_\ell jj$	$W^+W^-, ZZjj$	12.3	21.8	0.56
$\ell^\pm\ell^\mp\ell'^\pm\nu'_\ell jj$	$W^\pm Zjj$	2.34	4.38	0.53
$\ell^\pm\ell^\mp\ell'^\pm\ell'^\mp jj$	$ZZjj$	0.098	0.100	0.98

Table 2.2: Comparison of the predicted cross-section for fully leptonic final states of the $VVjj$-EW and $VVjj$-QCD processes calculated with Sherpa at LO in a typical phase space. The calculations include leptons of the first and second generation only, $\ell^\pm = e^\pm, \mu^\pm$; (anti-)neutrinos are labelled collectively ν. Statistical uncertainties on the cross-section from the phase space integration are below 2%. Numbers taken from Ref. [61], where detailed information on the process generation and the fiducial phase can be found. The last column shows the ratio of the $VVjj$-EW over the $VVjj$-QCD induced cross-section.

2.1.4 Experimental Results on Vector Boson Scattering

Vector Boson Scattering at the LHC is expected to have cross sections of only a few femtobarns, as shown in Table 2.2. Compared to other processes currently measurable in experiments, VBS is among the rarest, pushing the limits of what can be achieved with the available LHC data.

Being so close to the detection threshold with the current dataset also means that, at the beginning of LHC operations, there was insufficient data to access VBS. During Run-1, efforts in diboson studies focused on establishing inclusive diboson production[3]. This means studying the production of two vector bosons without imposing specific requirements on tagging jets or additional objects. The cross-sections for these inclusive diboson processes are about ten times higher than those for VBS and are dominated by QCD-mediated diagrams. By the end of Run-1, with 20 fb^{-1} of data, statistics was not a limiting factor for inclusive dibosons measurements. This enabled a transition to precision analyses, where differential distributions could be measured, and systematic uncertainties became the primary focus. I contributed to the legacy Run-1 WZ results [62], particularly by improving the data-driven background estimation, which was the dominant source of uncertainty in the measurement. Additionally, I was responsible for the statistical analysis extracting the cross-section measurements and comparing them with theoretical predictions. One key lesson I learned from this work was the significant impact of higher-order corrections on cross-sections and distributions. Initial inclusive diboson total cross-section results exhibited a 15%

[3] Dibosons are important backgrounds to Higgs boson production. Measuring them with high precision helped establish a solid foundation for the Higgs discovery.

discrepancy when compared with Next-to-Leading Order calculations[4], which disappeared entirely once Next-to-Next-to-Leading Order corrections were included in the theoretical predictions.

Although this document focuses on VBS experimental results, this brief discussion highlights how lessons learned from inclusive diboson measurements helped validate the analysis chain, paving the way for VBS studies. In fact, the WZ legacy paper I just discussed [62] already included the first VBS analysis on $WZjj$. At that time, the sensitivity was still too low to report a significance, so only 95% confidence level limits on the cross-section were extracted. This was my initial involvement in VBS, and I have been engaged in the field ever since.

Using the Run-1 dataset, the first VBS searches were published for the fully leptonic channels the $W^{\pm}Zjj$ [62] already mentioned, as well as $W^{\pm}W^{\pm}jj$ [63, 64], and $Z\gamma jj$ [65]. Among these early searches, only the $W^{\pm}W^{\pm}jj$ reached the level of evidence, with a 4.5σ observed significance (3.4σ expected) in ATLAS [63]. All Run-1 results were limited by statistics, a limitation quick overcome with the arrival of the LHC Run-2 dataset.

I became more actively involved in VBS at the beginning of Run-2, an exciting period when the first observations of these processes were anticipated. The increased center-of-mass energy led to higher production cross-sections, and the larger dataset provided clear advantages. During this time, I also took on the role of electroweak convener, overseeing and supporting the development of these analyses within ATLAS. With approximately 40 fb^{-1} of early Run-2 data, the statistic was sufficient to achieve the first observations of electroweak production in the fully leptonic $W^{\pm}W^{\pm}jj$ and $W^{\pm}Zjj$ channels [5, 7, 66, 67]. This dataset also enabled evidence for $ZZjj$ [68] and a first study involving semi-leptonic decays, targeting $WW/WZ\ jj$ events where one of the bosons decayed into jets [69].

The full Run-2 dataset, with 140 fb^{-1}—roughly three times larger than the early Run-2 analyses—allowed for the extension of VBS searches to other diboson channels. With sufficiently high statistical significance, VBS analyses have now transitioned from searches to measurements. The most recent measurements of various $VVjj$-EW final states in ATLAS are summarized as data/theory ratios in Figure 2.9. The initial 8 TeV results are shown in red/orange, while the purple/pink lines correspond to either full or partial Run-2 datasets. The statistical uncertainty remains dominant in all channels, as evident from the darker area in the error bars. Nevertheless, some channels have already the needed accuracy to provide the first differential distributions.

Now let's discuss some of the common experimental aspects to VBS. Most analyses have focused on isolating the electroweak component of the $VVjj$ process, using the Leading Order signal definition discussed earlier. However, more recent studies [70–72] have begun reporting fiducial cross-sections for inclusive $VVjj$ production, alongside with measurements of the electroweak contribution. This approach aligns with theoretical recommendations aimed at improving the precision of higher-order calculations. In all cases, the results are presented in terms of fiducial cross-sections, as a fully inclusive measurement is not well-defined—partons must be assigned a minimum p_T threshold. The fiducial phase space is specified through a set of generator-level requirements, typically chosen to closely match the reconstruction-level selection in order to minimize theoretical uncertainties. The broadest fiducial phase space at the parton level requires all partons to have $p_T > 10$ GeV and at least one pair of outgoing partons with an invariant mass $M_{qq} > 100$ GeV. Additionally, several studies have placed constraints on dimension-8 Effective Field Theory parameters or limits on new beyond the standard model resonances, topics that will be discussed in Chapter 3.

[4] This discrepancy caused considerable concern, making me worry that there might be an issue with the analysis.

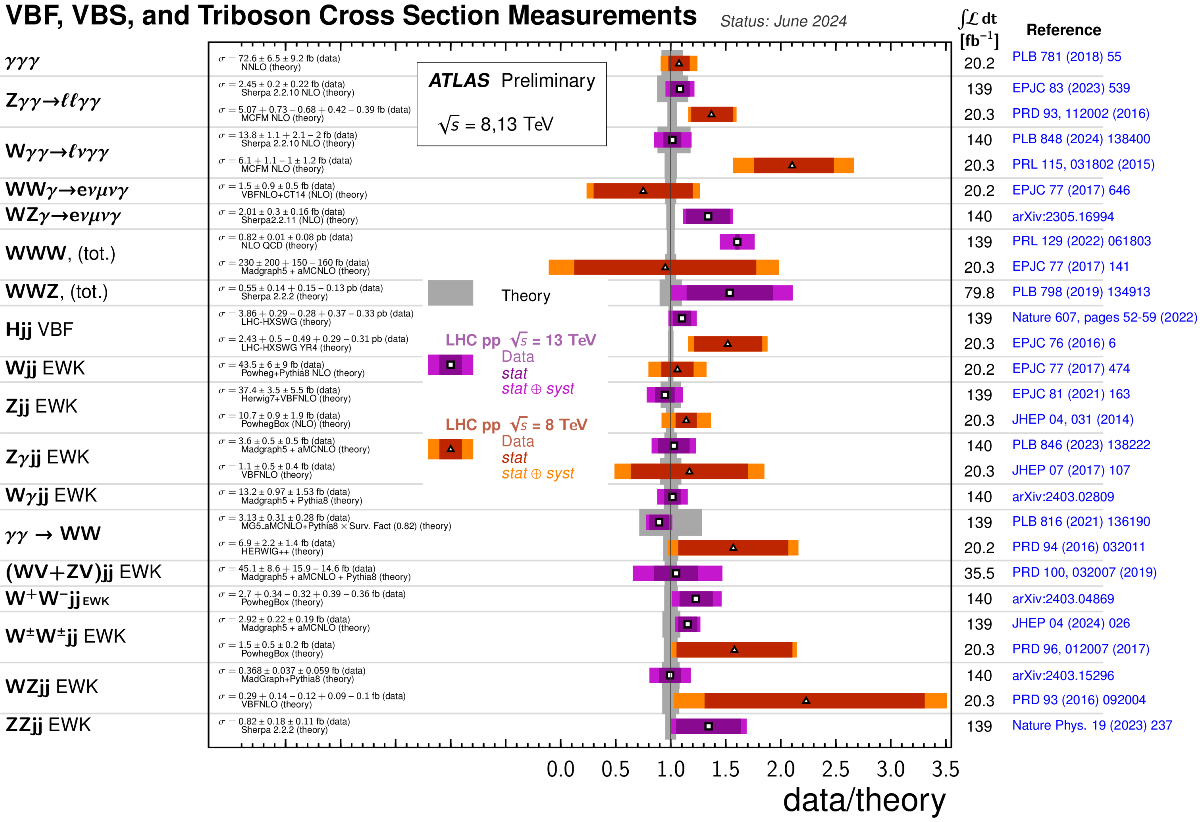

Figure 2.9: The data/theory ratio for several vector boson fusion, vector boson scattering, and triboson fiducial production cross-section measurements.

Regarding the selections each analysis has been optimized depending on the final state, nevertheless some common choices arise, for instance all $VVjj$ analyses exploit the VBS event topology by involving requirements $\Delta\eta_{jj}$ and M_{jj}. In leptonic analyses, events are selected using single-lepton or double-lepton triggers, ensuring a high trigger efficiency for events meeting the offline selection criteria. For other channels, more complex combinations of triggers are employed, often based on jet activity or missing transverse momentum.

The $VVjj$-EW signal processes are usually simulated at leading order with six EW vertices and no QCD vertices, using MADGRAPH [73–75]. For all final states except those involving two same-sign leptons, the $VVjj$-QCD process represents a major irreducible background. To distinguish the EW signal from this QCD background, most experimental results employ multivariate analysis (MVA) techniques that exploit VBS-specific kinematic features. Various MVA implementations are used, including Boosted Decision Trees (BDTs), Deep Neural Networks (DNNs), and Artificial Neural Networks (ANNs). The MVA output typically serves as the final discriminant variable in the signal region. While these techniques significantly enhance analysis sensitivity, they are also highly dependent on theoretical modeling, as they rely on fully simulated events for training. VBS analysis show a quite sizable modeling uncertainties in part due to the missing higher order corrections and scale variations added as uncertainties on the analysis.

Accurately estimating the $VVjj$-QCD background is a critical aspect of the analysis. The shape of this background is generally taken from simulations, while its normalization is determined through data fits in dedicated control regions (CRs), constructed by inverting some of the standard VBS selection criteria. Multiple Monte Carlo event generators are used for $VVjj$ simulation, with significant efforts from both theorists and experimentalists to validate them at the matrix-element level. The choice of parton shower scheme is also crucial. Given the computational cost of simulating QCD samples with up to two extra jets, these are typically generated at next-to-leading order in QCD and/or using matched-and-merged samples with either MADGRAPH or Sherpa [76]. The interference between EW and QCD diagrams is usually modeled with MADGRAPH, and its contribution to the EW process yield is typically in the 1–3% range.

Other significant background sources include misidentified objects reconstructed as leptons or photons. Hadronic activity misidentified as leptons and electrons from photon conversions are mitigated through isolation and identification requirements. Since these backgrounds are often poorly modeled in simulations, data-driven techniques are necessary for their estimation. A combination of control regions in both data and simulation is typically used for this purpose.

Among the various experimental results, the opposite-sign $W^{\pm}W^{\mp}jj$ process, characterized by two oppositely charged leptons and two neutrinos, stands out as particularly challenging and was only recently observed [4, 77]. This final state suffers from substantial background contamination, primarily from top-quark pair production, where both $W^{\pm}$ bosons originate from top decays. To isolate the signal, an effective b-jet veto was implemented, complemented by a multivariate approach to further separate the signal from backgrounds.

Another recent observation comes from the semi-leptonic final states, where the analysis employs latest developments on hadronic boson tagging, incorporating resolved and merged topologies. The resolved approach reconstructs a $W^{\pm}$ or Z boson from two small-radius jets (typically $R = 0.4$) with an invariant mass close to the boson mass. Alternatively, the merged approach selects a large-radius jet ($R = 1.0$) containing two primary subjets whose combined mass is consistent with a $W^{\pm}$ or Z boson. Due to limitations in jet energy resolution, distinguishing between hadronic $W^{\pm}$ and Z bosons remains challenging, leading to analyses that combine both decay modes. Despite their larger branching ratios, hadronic decays suffer from substantial background contamination. To mitigate this, stringent p_T requirements are imposed on the jets. The first evidence and observation of such processes were reported by the collaborations using the full Run-2 dataset [78, 79]. This phase space is particularly valuable for probing physics beyond the Standard Model due to its large energy reach.

Fully hadronic decays of vector bosons in VBS remain largely unexplored, with neither ATLAS nor CMS publishing dedicated analyses focusing solely on this final state. The overwhelming background from multijet production makes such studies feasible only when selecting highly boosted vector bosons. While these analyses may have limited sensitivity to Standard Model $VVjj$ processes, they are of significant interest for Beyond Standard Model searches.

Although $VVjj$ production with photons does not directly probe the mechanism of Electroweak Symmetry Breaking, these processes remain of interest. Experimentally, they involve the direct detection of energetic photons, which leads to high detection efficiencies and relatively large fiducial cross-sections. Theoretically, such processes provide a means to test the gauge structure of the Standard Model, as photon-involved scatterings probe similar interactions.

Fully leptonic channels, such as $W^{\pm}W^{\pm}jj$ and $W^{\pm}Zjj$, offer some of the cleanest experimental signatures. These analyses are now progressing toward more precise measurements, including unfolded distributions [71, 72] and initial polarization studies [70, 80]. My involvement includes contributions to the partial Run-2 results for $W^{\pm}W^{\pm}jj$ and $W^{\pm}Zjj$, as well as the full Run-2 results for $W^{\pm}W^{\pm}jj$. In these studies, I supervised a team of outstanding students: Franziska Iltzsche [81], Stefanie Todt [60], Anna Tegetmeier [82], Tim

Herrmann [83] and Max Stange [84], who worked on the same-sign $W^{\pm}W^{\pm}jj$ publications [5, 71], and Carsten Bittrich [85], who focused on $W^{\pm}Zjj$ [62]. In the following sections, I will highlight key aspects of these fully-leptonic analyses.

Electroweak $W^{\pm}Zjj$ Production

Electroweak $W^{\pm}Zjj$ production is a particularly interesting channel for VBS studies, thanks to the excellent reconstruction and identification capabilities for fully leptonic WZ events. However, a key challenge in this analysis is handling the substantial $W^{\pm}Zjj$-QCD background, which is expected to be at least twice as large as the electroweak signal contribution (see Table 2.2).

This process was among the first VBS observations at the LHC [62]. The analysis requires events with three charged leptons (electrons or muons) with a total charge of ±1, moderate $p_{\mathrm{T}}^{\mathrm{miss}}$, and a distinct VBS topology. Selected events must contain two jets with a large m_{jj}, positioned on opposite sides of the detector. To identify Z bosons, an oppositely charged same-flavor lepton pair is required to have an invariant mass consistent with the Z mass. To further suppress backgrounds from misidentified leptons, a stricter isolation and identification selection is applied to the extra lepton associated with the W boson. This reduces the contribution of misidentified leptons to just 5%.

After event selection, the signal region remains largely dominated by QCD-induced WZ production, which contributes up to 55%. Other backgrounds involving three prompt leptons, such as $tZj + VVV$ (3%), $t\bar{t} + V$ (4%), and ZZ (8%), also play a role. Given that the electroweak process contributes only 25% in the signal region, a multivariate approach is used to enhance the separation between signal and background. A boosted decision tree (BDT) is trained using 15 kinematic variables to exploit differences between the electroweak WZ signal and the QCD-induced background. A crucial aspect of achieving observation was ensuring proper modeling of both the electroweak signal and the QCD-induced WZ background for use in the BDT training. This meant that significant efforts were devoted to understand the modeling of the electroweak signal $WZjj$-EW and the QCD-induced WZ background in association with additional QCD emissions.

Simulating $VVjj$-EW events is inherently challenging due to the complexity of the process, the high-dimensional phase space, and unique features of the signal, such as the absence of color flow at leading order between the two final-state quark lines. This color connection pattern is an essential characteristic of the signal. When a third jet is included in the matrix element calculation—either via merging or at NLO—it reflects this color topology. Since full NLO event simulation is not feasible yet for many final states, the third jet or any additional ones are typically modeled as part of the parton shower. However, this introduces challenges, as some parton shower generators assume a default color connection that may not align with the signal properties.

Issues with color flow have been observed in the Pythia 8 parton shower [41], and solutions have been proposed to address them. To better understand and estimate uncertainties in signal modeling, different generators and shower configurations were tested. A detailed discussion of these studies can be found in Carsten's thesis [85]. To illustrate key findings, Figure 2.10 compares three matrix element (ME) generators paired with different parton showers: Sherpa [76] (which includes both ME generation and its own shower), MadGraph5 (MG5) [75] and Whizard, which are combined with Herwig7 (H7) or Pythia8 [86]. For Pythia8, both the default settings (Py8) and the color-aware configuration (Py8Fix) are tested. While leptonic variables are generally well-modeled, the impact of parton showering is more pronounced in certain observables. As an example, Figure 2.10 shows the η distribution of the third-hardest jet, a variable sensitive to shower effects. Large modeling discrepancies are observed, highlighting the need for careful selection of BDT input variables. To mitigate uncertainties, variables involving the third jet were excluded from the BDT training, and the modeling of all variables included validated with data. Additionally, differences between parton shower configurations, along with standard PDF, renormalization, and factorization scale uncertainties, were incorporated into the analysis as uncertainties on the signal.

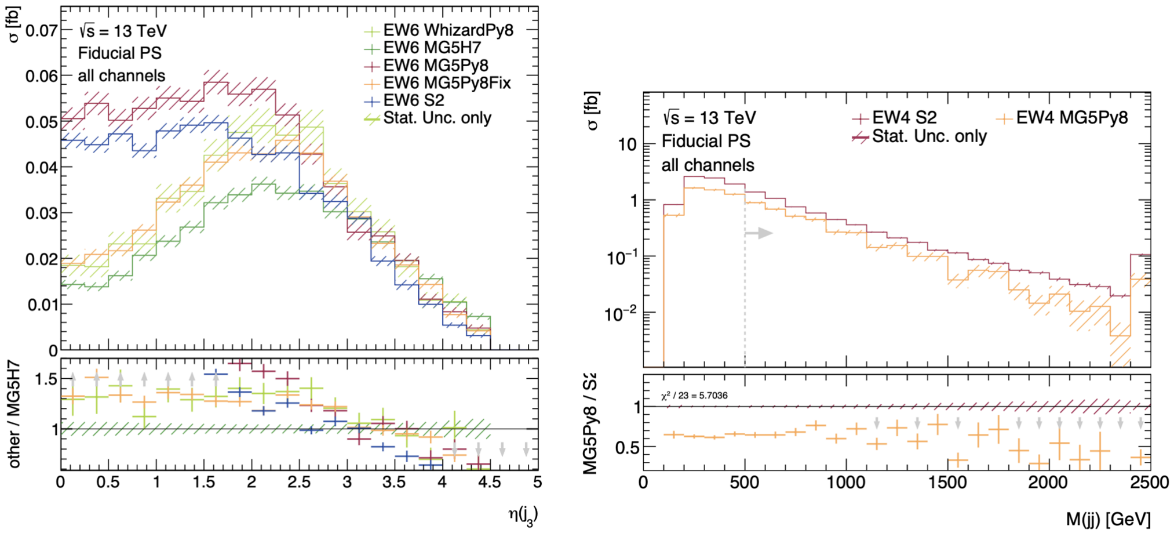

Figure 2.10: Comparison of differential cross-sections for different simulations of the $WZjj$-EW signal (left) and $WZjj$-QCD background (right). Figures taken from [85].

The modeling of the $WZjj$-QCD background requires a different approach compared to the signal process. Since the final state with two jets can also arise from additional emissions in diboson production, processes with initially the same or even lower jet multiplicity in the hard scatter can enter the signal region when extra jets from the parton shower or pileup satisfy the VBS jet selection criteria. To ensure a reliable description of this background, it is crucial to include the third jet in the hard process definition. Given the standard color-flow topology of the $WZjj$-QCD final state, the usual matching and merging techniques can be applied effectively.

At the time of the observation analysis, only Sherpa (S2) simulation was available for the $\ell\ell\ell\nu jj$ final state. This sample was based on diboson production, $pp \rightarrow \ell\ell\ell\nu$, with $0, 1j$@NLO accuracy, merged with extra $2, 3j$@LO. To provide an alternative prediction, truth-level simulations were performed using Madgraph+Pythia8 (MG5Py8) with CKKW-L merging [87], generating diboson production with up to three additional partons at LO accuracy. This setup was designed to match the nominal configuration used by the CMS collaboration [67]. Figure 2.10 compares the two simulations for the di-jet invariant mass. Large differences between the two approaches are observed but remain relatively constant across all observables. A significant portion of the discrepancy arises from the absence of virtual corrections for the 0- and 1-jet final states in Madgraph. Given its higher accuracy in the base process, Sherpa is chosen as the baseline, while the differences between generators are treated as a conservative uncertainty.

To estimate the normalization of backgrounds with prompt leptons, three control regions orthogonal to the signal region were defined. The WZ control region, selecting events with a low di-jet invariant mass. The ZZ control region, requiring an additional fourth lepton in the event. The b-tag control region, where at least one b-jet is required, to constrain $t\bar{t} + V$ backgrounds. These control regions help constrain the normalization of the corresponding backgrounds in the fit. The miss-identified leptons are estimated with a data-driven approach.

The cross-section of electroweak WZ production is extracted through a binned maximum-likelihood fit of the BDT score distribution in the WZ signal region, together with the three control regions. The fit includes systematic uncertainties related to object reconstruction, background modeling, and QCD-EW interference. The QCD-EW interference contributes up to 10% in the signal region and is incorporated as an uncertainty in the $WZjj$-EW template. The normalization factors for the key backgrounds, constrained from data, are measured as follows:

$$\begin{aligned} \mu_{WZjj-\text{QCD}} &= 0.56 \pm 0.16, \\ \mu_{t\bar{t}+V} &= 1.07 \pm 0.28, \\ \mu_{ZZjj-\text{QCD}} &= 1.34 \pm 0.44. \end{aligned}$$

Interestingly, the normalization factor obtained for $WZjj$-QCD indicate a significant reduction in the predicted QCD background is needed to fit the data. While for $t\bar{t} + V$ and $ZZjj - \text{QCD}$ the normalization factors are consistent within uncertainties with the theory prediction.

The normalization factor for the $WZjj - \text{EW}$ signal indicates that a large increase on the predicted WZjj-EW contribution is needed to fit the data in the signal region:

$$\begin{aligned} \mu_{WZjj-\text{EW}} &= 1.77^{+0.44}_{-0.40}\ \text{(stat.)}\ ^{+0.15}_{-0.12}\ \text{(exp. syst.)}\ ^{+0.15}_{-0.12}\ \text{(mod. syst.)}\ ^{+0.15}_{-0.13}\ \text{(theory)}\ ^{+0.04}_{-0.02}\ \text{(lumi.)} \\ &= 1.77^{+0.51}_{-0.45}, \end{aligned}$$

Using the fitted $\mu_{WZjj-\text{EW}}$ the measured fiducial cross-section for electroweak $WZjj$ production is calculated to be:

$$\begin{aligned} \sigma^{\text{fid.}}_{WZjj-\text{EW}} &= 0.57^{+0.14}_{-0.13}\ \text{(stat.)}\ ^{+0.05}_{-0.04}\ \text{(exp. syst.)}\ ^{+0.05}_{-0.04}\ \text{(mod. syst.)}\ ^{+0.01}_{-0.01}\ \text{(lumi.)}\ \text{fb} \\ &= 0.57^{+0.16}_{-0.14}\ \text{fb}. \end{aligned}$$

This result includes interference effects between the QCD and electroweak $WZjj$ processes. Regarding the uncertainties, as expected the dominant uncertainty comes from the limited statistics, experimental systematics are dominated by jet reconstruction uncertainties, theoretical modeling uncertainties already have a sizable impact event thought normalization effects are mitigated by the free floating parameters on the fit, and finally luminosity with a small impact. For comparison, the Standard Model LO prediction from Sherpa for electroweak production, without interference, is :

$$\sigma^{\text{fid., Sherpa}}_{WZjj-\text{EW}} = 0.321 \pm 0.002\ \text{(stat.)}\ \pm 0.005\ \text{(PDF)}\ ^{+0.027}_{-0.023}\ \text{(scale) fb}.$$

This study marks the first observation of the electroweak $WZjj$ process in ATLAS, achieving a significance of 5.3 standard deviation, with a 3.2 expected from Sherpa. This milestone confirms the existence of the process. Following the theorist recommendations, results in the inclusive $WZjj$ setup, where both electroweak and QCD contributions are considered as signal are also provided, in the form of a fiducial cross-section measurement along with unfolded distributions. Figure 2.11 presents the ratio between the measured inclusive $WZjj$ fiducial cross-sections and the SM prediction from Sherpa, shown for each of the four lepton channels and their combination. Remarkably, all measured data points lie systematically below the Sherpa prediction. Even if it is still in agreement within uncertainties this striking trend, also observed in the electroweak-only fit, suggests a potential overestimation of the $WZjj$-QCD cross-section in Sherpa simulations.

Unfolded distributions using the inclusive $WZjj$ setup have been measured for key observables sensitive to anomalous couplings (these unfolded distributions will be used in Section 3.2.2 to set limits using the Effective Field Theory approach), as well as for jet kinematics variables. When compared to Sherpa predictions—after rescaling the $WZjj$-QCD and $WZjj$-EW components—these differential measurements exhibit excellent agreement in shape within uncertainties. This validation reinforces the robustness of our analysis and sets the stage for the following ATLAS measurements.

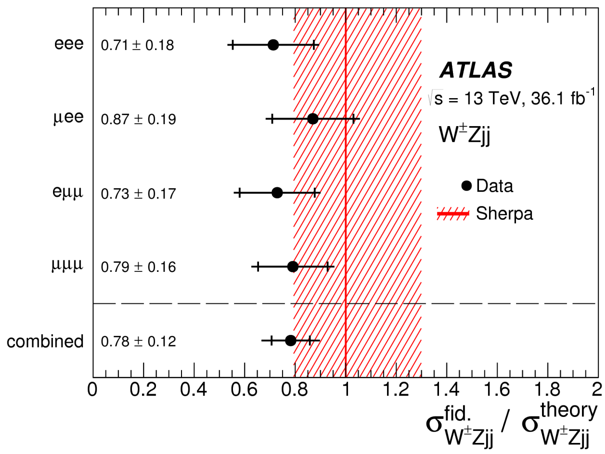

Figure 2.11: Ratio between measured and predicted $WZjj$ integrated cross-sections (EW+QCD) in the fiducial phase space. The inner and outer error bars represent statistical and total uncertainties, respectively. The hatched band indicates the uncertainty in the Sherpa prediction. Figure taken from [7].

Electroweak $W^{\pm}W^{\pm}jj$ Production

Compared to the $WZjj$ analysis just discussed—and actually all other VBS channels—the scattering of two same-charge $W^{\pm}$ bosons stands out as the $e^{\pm}\mu^{\pm}$ golden channel for VBS, with the best signal-over-background ratio. This is because it is the only VBS process where the electroweak contribution dominates over the QCD-induced component (see Table 2.2). This unique feature arises from the absence of gg and qg initial states at leading order for the QCD process, unlike in other channels. Additionally, the presence of same-sign W bosons in the final state largely reduces other sources of background.

This analysis focuses on the fully leptonic decays of the W bosons, into electrons or muons and their associated neutrinos. Events are selected based using the characteristic VBS topology, requiring two high-p_T jets with a large rapidity separation ($|\Delta Y_{jj}| > 2$) and an invariant mass $M_{jj} > 500$ GeV. The modeling of the EW signal has evolved over time: while early Run-2 analyses used Sherpa 2.2.2 with 2- and 3-jet merging at LO as the nominal prediction, more recent full Run-2 results adopted Madgraph 5 at LO.

The presence of two same-sign leptons provides a strikingly clean experimental signature, effectively suppressing dominant backgrounds such as Z + jets and $t\bar{t}$. However, background contributions from those still appear due to jets misidentified as leptons (leading to random charge assignments) and charge misidentification of true leptons (charge-flip), which accounts for approximately 10% of events in the signal region. Another significant background originates from $W\gamma$ events, where photon conversions mimic a same-sign lepton pair, contributing around 10% in the signal region. The dominant background, however, comes from incompletely reconstructed WZ events, when one of the leptons fails the object selection criteria or falls outside the detector acceptance, which contributes up to 30% in the signal region.

I have contributed to two versions of this analysis. The first analysis, using a partial Run-2 dataset, aimed to achieve the first observation of this process and provide an initial cross-section measurement at 13 TeV [5]. The second version included the full Run-2 dataset, the observation was already well established, and the focus shifted to delivering a precise measurement, including differential distributions, and limits on beyond the Standard Model predictions [71].

During the optimization phase of the analysis for the observation, the analysis team explored several strategies to improve background rejection. In particular, optimizing the isolation and identification working points for lepton selection helped reduce backgrounds from misidentified leptons [16, 17]. To further mitigate contributions from charge-flip events, a charge-flip electron identifier (ECIDS), based on a Boosted Decision Tree, was introduced [88].

The largest remaining background is QCD-induced WZ production, which closely mimics the signal when one lepton is not reconstructed. However, a distinctive feature of this background is that it has a larger fraction of gluon-initiated jets compared to the signal. To enhance the rejection of the WZ background, we investigated the potential benefits of tagging the VBF jets as originating from quarks or gluons. As part of A. Tegetmeier's bachelor project [82], we carried out truth-level studies to evaluate the impact of such a tagger. These studies indicated that, in an ideal scenario where the jet origin is perfectly identified, the $WZjj$ background could be reduced by nearly 50%. Of course, an ideal tagger does not exist. Therefore to check the effect of a realistic tagger in the data we used the existing quark-gluon tagger developed by the ATLAS jet group [89] to classify the nature of the VBF jets. This tagger has a version based on track multiplicity requirements in the inner detector and another that combines several jet substructure observables using a BDT. Unfortunately, the background rejection gain was limited. This was partly due to the VBF topology, which results in jets being more forward, often falling outside the inner detector coverage, making track information unavailable. Additionally, the discriminating power of the tagger is more effective for high-energy jets, whereas VBF jets are typically not highly boosted. Figure 2.12 illustrates the track multiplicity (N_{tracks}) for the sub-leading p_T VBF jet in the $WZjj$-QCD background entering the signal region. The distribution is separated into two p_T ranges and categorized by jet origin (quark, pileup or gluon). It can be seen that differences in track multiplicities are expected for the different types. Although this particular tagger was not included in the analysis due to its low efficiency for our case, the distribution here shows that when the tracking information is available some discrimination power could be gained. The study highlights its potential for future analyses at the High-Luminosity LHC (HL-LHC), where tracking coverage will be significantly extended.

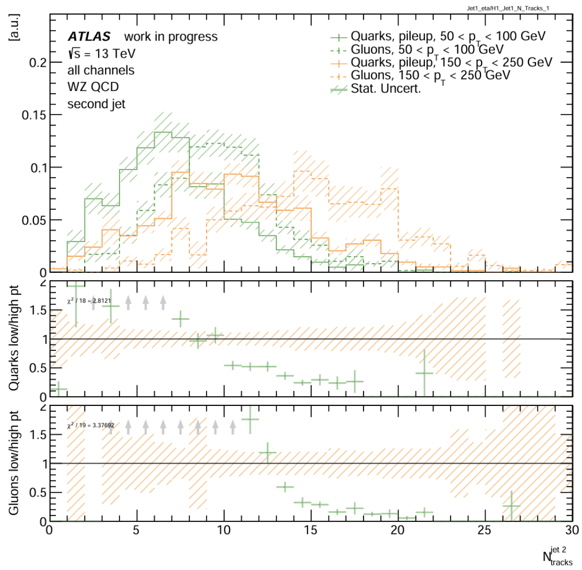

Figure 2.12: Track Multiplicity for the sub-leading p_T VBF jet. The labels Quarks, pileup, and Gluon refer to the respective truth jet origin. The upper subplot shows the ratio of quark jets, while the lower subplot shows this ratio for gluon jets. Figure taken from [82].

Another significant background in the signal region arises from misidentified leptons. Although stringent isolation and identification requirements reduce this contribution to approximately 10%, it remains a challenging source of systematic uncertainty. Aiming to improve the background estimation, Max Stange's master project [84] focused on a data-driven approach using control regions enriched with jets to estimate the probability of a jet being misidentified as a lepton. Constructing these control regions is a delicate task, as it is crucial to maintain a jet composition—in terms of origin of the jet—that closely mirrors that of the signal region. This minimizes the uncertainty due to the extrapolation between the control and signal regions and enhances the robustness of the background estimation. In his work, a new control region based on dilepton events was introduced. This dilepton+jet control region is kinematically closer to the signal region than the previously used dijet control region. While this alternative region had smaller uncertainties related to jet composition, it suffered from limited statistics and was therefore used as a cross-check.

Once the analysis selections and background estimations were established, the next step is the statistical interpretation of the data. A major contribution from the team was the development of a statistical framework tailored to the needs of the analysis. The statistical analysis of both publications was the central focus of the PhD theses of Franziska Iltzsche [81] and Tim Herrmann [83]. Our contributions covered the entire statistical analysis process, from cross-section extraction to unfolding distributions using the likelihood unfolding method, and setting limits on Effective Field Theory operators.

The statistical analysis aims to exploit differential distributions for parameter estimation and hypothesis testing. Given the limited statistics in early results, M_{jj} was used as the primary discriminating variable. However, in the full Run-2 analysis, two-dimensional distributions were introduced, such as the dilepton invariant mass together with M_{jj}, as the former is particularly sensitive to new physics effects. The observable binning was optimized with respect to the expected significance as part of the statistical analysis, the procedure is detailed in Ref. [83]. Splitting the signal region into mutually exclusive channels based on lepton flavor and charge also proved to be highly beneficial for constraining different background contributions, as the sources of misidentified electrons and muons differ.

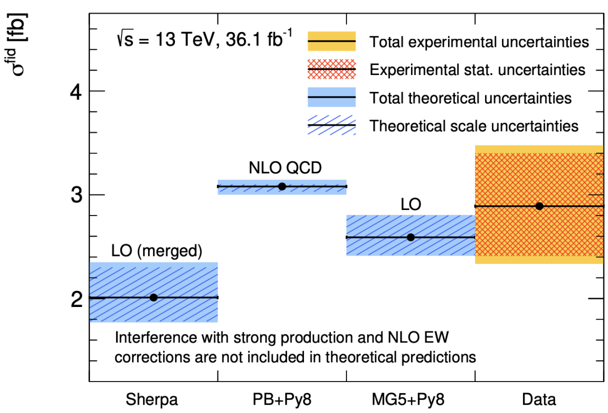

Figure 2.13: Comparison of the measured fiducial cross section with theoretical predictions from Sherpa 2.2.2, Powheg-Box+Py8, and Madgraph. Statistical uncertainties are shown as a checked orange band, combined experimental uncertainties in light orange, scale-dependent theoretical uncertainties as a dashed blue band, and total theoretical uncertainties in light blue. Predictions exclude $W^{\pm}W^{\pm}jj$ electroweak-strong interference and NLO electroweak corrections. Figure taken from [60].

Given the discrepancies on the cross-sections seen in the $WZjj$ analysis the normalization of this background was constrained using data in a dedicated $WZjj$ control region while the shape is estimated with MC simulation. Additionally, information from events with lower M_{jj} values than those in the signal region was used to define a second control region. This low-M_{jj} control region has a smaller signal contribution and similar background composition. Like the signal region, it was split into charge- and flavor-dependent channels which helped to constrain the misidentified lepton background uncertainties.

The signal region and the two control regions are evaluated simultaneously in the fitting procedure, in order to extract the parameters of interest. The background-only hypothesis is rejected with a significance of 6.5σ, marking the first observation of this process in ATLAS. The results are also presented in terms of a fiducial cross-section [5], and are shown in Figure 2.13, compared with three different signal predictions: the nominal prediction from Sherpa 2.2.2, which includes $2,3j$@LO; a Powheg+Pythia8 calculation at next-to-leading order in QCD (PB+Py8); and a pure leading-order MADGRAPH+PYTHIA8 with the fixed color-flow settings (MG5+Py8). It can be see here again that the SHERPA 2.2.2 prediction for the $W^{\pm}W^{\pm}jj$-EW prediction underestimated the observed signal, part of this issues were traced back to the internal color-flow settings in Sherpa and solved with appropriated settings in a never version of the generator. This first results were still largely dominated by statistical uncertainties.

For the full Run-2 analysis, with four times more data available, the possibility of performing a differential analysis on top of the fiducial cross-section measurements became feasible. A careful selection of the variables to unfold was made, considering their sensitivity to potential new physics and their relevance for validating theoretical predictions. Valuable input for this selection came from discussions within the VBSCan COST Network [90]. The variables chosen for the analysis include the dilepton mass, $m_{\ell\ell}$, and the transverse mass, m_T, of the dilepton–E_T^{miss} system, both of which are particularly interesting due to their sensitivity to new physics effects. Additionally, key variables characteristic of vector boson scattering were included, such as the dijet mass, M_{jj}, the number of jets in the rapidity gap between the two VBF signal jets, $N_{\text{gap jets}}$, and the Zeppenfeld variable of the third jet, ξ_{j3}. A dedicated fit is performed for each variable of interest to extract the corresponding differential cross-section. Separate fits are also used to determine the electroweak $W^{\pm}W^{\pm}jj$-EW and inclusive $W^{\pm}W^{\pm}jj$ cross sections.

The fit setup follows the approach described earlier, using the signal region and two control regions. However, for this analysis, two-dimensional distributions are employed in both the signal region and the low-M_{jj} control region. In every bin of the variable of interest, the M_{jj} distribution is fitted to improve the constraints on the signal strength. The cross-section unfolding relies on a maximum-likelihood fit, following the method outlined in Ref. [91]. The unfolding procedure is applied to the detector-level distributions in both the signal and control regions. The detector-level signal distribution is decomposed of multiple subsamples, each corresponding to a specific range of the particle-level variable of interest (referred to as a "cross-section bin"). The binning in the signal and low-m_{jj} control region distributions at the detector level is chosen to match the cross-section binning. The fit determines the signal strength parameters for each cross-section bin, alongside a free parameter for the normalization of the QCD $W^{\pm}Zjj$ background.

Figure 2.14 presents one of the results obtained with this fitting setup. The left figure shows the post-fit distribution of the VBF dijet invariant mass (m_{jj}) in the signal region, which serves as an input for extracting the differential cross-section of $W^{\pm}W^{\pm}jj$-EW as a function of $m_{\ell\ell}$. The $W^{\pm}W^{\pm}jj$-EW contribution in the figure is decomposed into the six $m_{\ell\ell}$ cross-section bins, and shown in different shades of blue. The right figure displays the unfolded distribution obtained with the inputs just described and the control regions, compared with different theoretical predictions from MADGRAPH 5 (using two different shower programs, PYTHIA8 and HERWIG7) and from SHERPA 2.2.11. The SHERPA 2.2.11 MC model includes partial NLO QCD corrections by incorporating real emissions of up to one extra parton, resulting in a 2% lower cross section for EW $W^{\pm}W^{\pm}jj$ production compared to the LO MADGRAPH 5. A significant improvement over previous results is the inclusion of next-to-leading order electroweak corrections within SHERPA 2.2.11 which has the effect of reducing the total prediction by approximately 15%. This distribution shows a good agreement with the bulk of the standard model predictions.

A summary of the measured and predicted $W^{\pm}W^{\pm}jj$-EW (and inclusive) fiducial cross sections is presented in Table 2.3. The Monte Carlo predictions generally agree with the measurements within experimental and theoretical uncertainties, although all predictions underestimate the measured cross-section values. These are the most precise fiducial cross section measurements of $W^{\pm}W^{\pm}jj$ production to date.

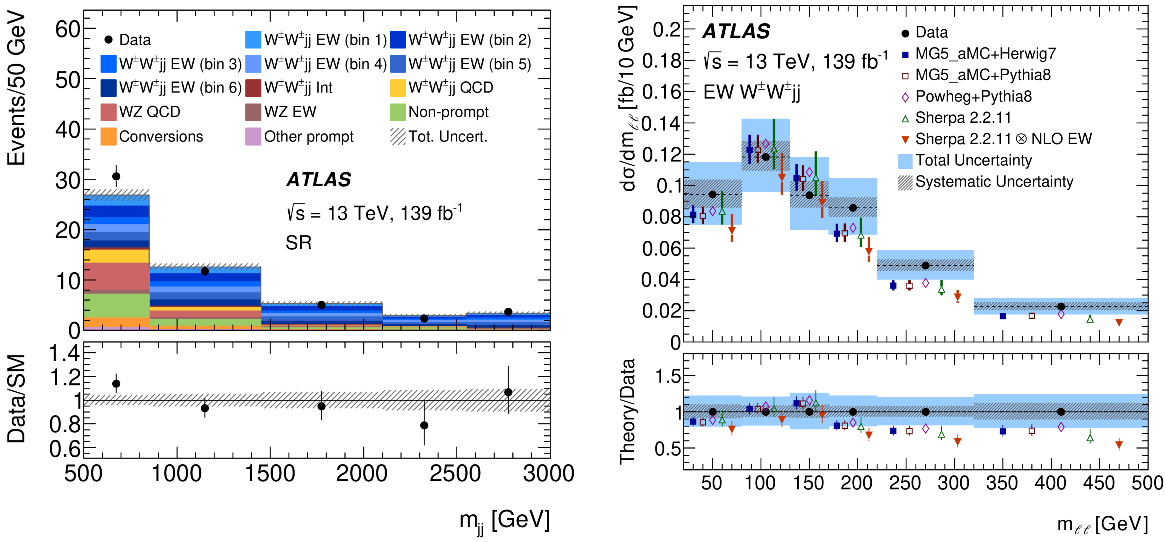

Figure 2.14: Left: Post-fit distribution of the VBF dijet invariant mass (m_{jj}) in the signal region, obtained during the extraction of the differential cross-section of $W^{\pm}W^{\pm}jj$-EW as a function of $m_{\ell\ell}$. Data points are shown in black with vertical error bars indicating statistical uncertainties. Contributions from $W^{\pm}W^{\pm}jj$-EW events in different particle-level $m_{\ell\ell}$ bins are displayed in various shades of blue, labeled as "bin N" (N = 1, 2, ..., 6) in the legend. Right: The measured fiducial differential cross-sections of $W^{\pm}W^{\pm}jj$-EW as a function of $m_{\ell\ell}$. Data points are in black, with horizontal bars indicating bin widths. Systematic uncertainties are represented by hatched boxes, while filled boxes denote total uncertainties. The results are compared to different Standard Model predictions.

Description	$\sigma_{\text{fid}}^{\text{EW}}$ [fb]	$\sigma_{\text{fid}}^{\text{EW+Int+QCD}}$ [fb]
Measured cross section	2.92 ± 0.22 (stat.) ± 0.19 (syst.)	3.38 ± 0.22 (stat.) ± 0.19 (syst.)
MG5_aMC+Herwig7	2.53 ± 0.04 (PDF)$^{+0.22}_{-0.19}$ (scale)	2.92 ± 0.05 (PDF)$^{+0.34}_{-0.27}$ (scale)
MG5_aMC+Pythia8	2.53 ± 0.04 (PDF)$^{+0.22}_{-0.19}$ (scale)	2.90 ± 0.05 (PDF)$^{+0.33}_{-0.26}$ (scale)
Sherpa	2.48 ± 0.04 (PDF)$^{+0.40}_{-0.27}$ (scale)	2.92 ± 0.03 (PDF)$^{+0.60}_{-0.40}$ (scale)
Sherpa ⊗ NLO EW	2.10 ± 0.03 (PDF)$^{+0.34}_{-0.23}$ (scale)	2.54 ± 0.03 (PDF)$^{+0.50}_{-0.33}$ (scale)

Table 2.3: Measured and predicted fiducial cross sections of the EW and inclusive $W^{\pm}W^{\pm}jj$ production, quoted with their respective uncertainties. For Powheg Box+Pythia only the central value is provided. Table adapted from [71]

2.1.5 What Have We Learned from Vector Boson Scattering?

The analysis of LHC Run-2 data has provided invaluable insights into electroweak boson scattering. During the past decade the observation of vector boson pair production in association with two jets was achieved for all diboson combinations, using both leptonic and semi-leptonic decay channels. These results were made possible by the combined efforts of the ATLAS and CMS Collaborations and the theory community. Given that this process is among the rarest that can currently be measured with the LHC data, its observation is a true success.

Beyond the initial observations, the first differential measurements have now been performed, and their precision is already challenging theoretical predictions. As more data is collected during Run-3 and later at the HL-LHC, we will be able to probe this sector in even greater detail, potentially becoming sensitive to higher-order effects and polarization effects.

But what conclusions can we draw so far regarding the gauge structure of the Standard Model? Are the quartic gauge couplings behaving as predicted? Is the Higgs boson playing its expected role in preventing unitarity violation? These were the questions I used to motivate the study, and were dramatically illustrated by Figure 2.2 showing unitarity violation if any of these couplings were removed. Are the fiducial cross-section measurements we have obtained until now already capable of answering these fundamental questions?

To better understand what kind of effects we should expect in $W^{\pm}W^{\pm}jj$-EW observables at the LHC, we have generated simulations using MadGraph+Pythia8. Our goal was to replicate the theoretical scenario where unitarity violations occur. This involved producing events with the LHC configuration and selecting the specific vertices to include in the simulation. The SM and non-SM predictions have been folded to reconstruction level with PowhegBox+Pythia8 to compare with data.

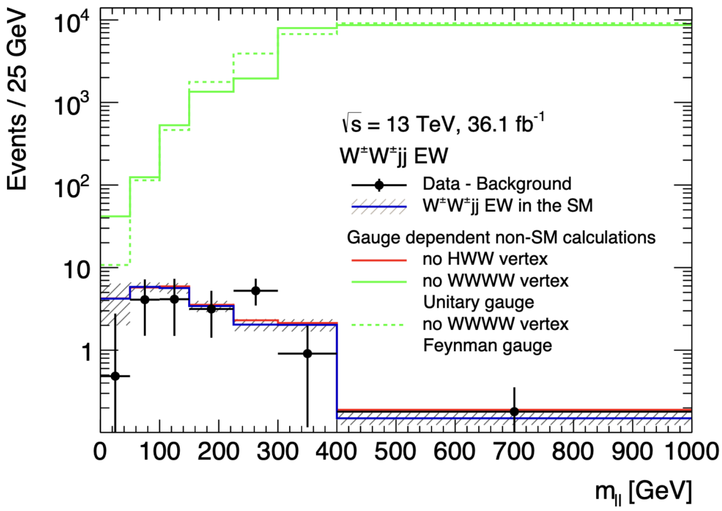

Figure 2.15: Distribution of the dilepton invariant mass, $m_{\ell\ell}$, for several alternative predictions of the $W^{\pm}W^{\pm}jj$-EW process, compared with background-subtracted data after the fit. The predictions include the Standard Model (blue), calculations in the absence of the quartic $WWWW$ vertex (green), and in the absence of the Higgs boson (red). The uncertainties in the background-subtracted data combine statistical uncertainties in the data with the statistical and systematic uncertainties of the backgrounds after the fit. The uncertainties in the SM prediction include experimental and theoretical systematic uncertainties before the fit. Figure based on inputs from Ref. [5].

The results of these simulations are shown in Figure 2.15, compared with background-subtracted data. As a reminder, in the Standard Model, $W^{\pm}W^{\pm}jj$-EW production involves intricate gauge cancellations between diagrams containing quartic electroweak couplings, trilinear couplings, and Higgs–gauge boson interactions. These cancellations can be visualized by comparing the full SM prediction (blue) with calculations where either the quartic $WWWW$ vertex is removed (green) or where the Higgs boson is absent (red). The latter two calculations, performed in unitary gauge at leading-order QCD, are gauge dependent.

As expected, removing the quartic $WWWW$ vertex (green lines) leads to unitarity violation, causing the cross-section to increase rapidly and diverge from both the SM prediction and the data. On the other hand, removing Higgs couplings to the W bosons has only a mild effect at the energy scales we currently probe. One key reason for this difference compared to the theoretical predictions in Figure 2.2 is that those calculations were made for longitudinally polarized bosons, whereas here, no polarization selection has been applied. Since the fraction of longitudinal bosons is below 5%, the impact of the Higgs contribution on the observables remains subtle.

If we truly want to be sensitive to Higgs-sector effects, the next crucial step is to study the polarization of the vector bosons. By isolating the longitudinal component, we can enhance our sensitivity to new physics in the electroweak sector. The study of polarized boson scattering is one of the major goals of both the LHC and HL-LHC programs, and the first steps in this direction have already been taken. Initial results are now available, paving the way for exciting new developments—let's explore them in the next section.

2.2 Vector Bosons Polarization

The polarization states of the $W^{\pm}$ and Z bosons are deeply connected to the origin of their mass—and therefore to the Higgs mechanism itself. To appreciate this connection, let us briefly revisit how the Standard Model generates mass without violating gauge symmetries.

In its early formulation, the Standard Model Lagrangian did not include explicit mass terms, neither for fermions nor for gauge bosons. This was no accident: such terms, like $m\bar{\psi}\psi$ for fermions or $\frac{1}{2}m^2 B^{\mu} B_{\mu}$ for vector fields, would break gauge invariance. Yet, experiments had long confirmed that the weak bosons are massive. The resolution came with the introduction of spontaneous symmetry breaking via the Higgs mechanism [34–36]. At the heart of this mechanism lies a complex scalar field transforming as an $SU(2)$ doublet. When this field acquires a non-zero vacuum expectation value (vev), the symmetry $SU(2)_0 \times U(1)_Y$ is broken down to $U(1)_{\text{em}}$, and the weak bosons acquire mass. Of the four real degrees of freedom in the scalar doublet, three become the longitudinal components of the $W^{\pm}$ and Z bosons, while the fourth manifests as the physical Higgs boson.

This "eating" of Goldstone bosons is more than a formal artifact—it gives the W and Z with an additional polarization state. Unlike massless gauge bosons, which can only be transversely polarized, massive bosons can also exhibit longitudinal polarization. And it is precisely this longitudinal mode that arises from the Higgs mechanism. This connection is not just elegant—it is essential. Without it, scattering amplitudes involving longitudinal vector bosons would grow uncontrollably at high energies, violating unitarity and rendering the theory inconsistent. The Higgs mechanism restores the consistency of the theory and tightly constrains the behavior of these bosons. The behavior of the longitudinal modes, in particular, are predicted with remarkable precision in the Standard Model. Deviations from these predictions could therefore offer one of the most sensitive probes of new phenomena in the electroweak sector [92, 93].

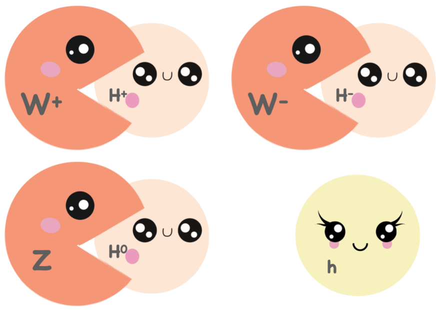

Figure 2.16: The Goldstone bosons generated by spontaneous symmetry breaking being "eaten" by the weak bosons. Image inspired by the quantumdiaries.org.

To illustrate how mass and polarization are intertwined, consider the photon: as a massless gauge boson, it can only be transversely polarized. A longitudinal polarization would imply a component of the field propagating faster than light, which is forbidden. By contrast, massive vector bosons do not move at the speed of light and can access this extra longitudinal degree of freedom—precisely the one generated by the Higgs mechanism.

This deep link between vector boson polarization and electroweak symmetry breaking opens a powerful window into the structure of the Standard Model—and what may lie beyond. At high energies, another layer of insight is provided by the Goldstone boson equivalence theorem [94], which states that the behavior of longitudinally polarized bosons becomes indistinguishable from that of the original Goldstone bosons. In other words, probing longitudinal W and Z bosons at high energies is equivalent to probing the Golsdstone bosons that gave them mass in the first place.

This makes polarization measurements in diboson final states a unique tool. If new physics alters Higgs couplings or introduces new interactions in the electroweak sector, such changes could subtly modify the fractions of longitudinal versus transverse bosons in the data. And the higher the energy, the closer we come to directly probing the dynamics of the Higgs mechanism itself.

The next sections will explore how polarization measurements are performed in practice, and what they are revealing about the electroweak sector—and potentially, about physics beyond the Standard Model.

2.2.1 Theory Predictions for Vector Boson Polarizations

Understanding how to separate the polarizations of electroweak massive bosons from a theoretical perspective is a necessary step before attempting to extract them from data. The W and Z bosons each have three physical polarization states: one longitudinal (0) and two transverse—left-handed (L) and right-handed (R). The transverse polarizations are often grouped together and denoted by T. Figure 2.17 illustrates the possible polarization modes for a massive particle.

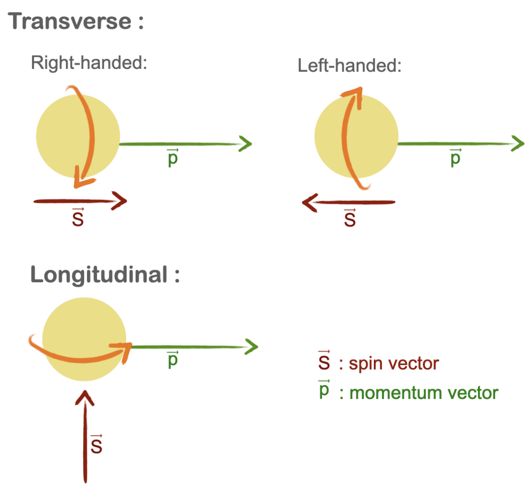

Figure 2.17: Polarization modes for a massive particle. Transverse polarization corresponds to spin aligned or anti-aligned with the momentum (right- or left-handed), while longitudinal polarization corresponds to spin perpendicular to the momentum.

Polarization is not a directly observable quantity, as W and Z bosons decay promptly into other particles. The information about their polarization must therefore be inferred from the kinematics of the decay products. The good news is that parity violation in weak interactions leads to distinctive angular distributions in the decay products depending on the polarization of the parent boson. These distributions provide statistical sensitivity to the underlying polarization of a sample. Extracting polarization fractions from data requires therefore accurate theoretical predictions of these angular distributions, corresponding to each polarization mode. Those can be confronted with experimental data to determine the relative contributions of longitudinal and transverse components to the total data sample, f_0 and f_T, with $f_0 + f_T = 1$, also know as polarization fractions.

The theoretical framework to describe the angular distributions from the leptonic decay of polarized bosons is well established. Each polarization state leads to a characteristic angular distribution for the decay products, which can be computed analytically in the full phase space [95, 96]. However, several complications arise when moving beyond this ideal case. First, since the W and Z bosons are unstable, decay amplitudes corresponding to different polarization states interfere. These interference terms cancel only upon full integration over the azimuthal angle of the lepton. In practice, detector acceptance and event selection criteria restrict the accessible angular range, and such cuts distort the distributions in a polarization-dependent way. As a result, it becomes impossible to directly use the analytical expressions in data fits. In addition, non-resonant diagrams contribute to diboson production already at tree level, for which a polarization interpretation is not well defined. Finally, polarization vectors are not Lorentz-covariant, which means we need to fix a specific reference frame that is consistently used in both theoretical predictions and accessible for data analysis.

To address these issues while preserving gauge invariance and maintaining predictive power in the definition of polarized signals, the target bosons must be on-shell. Therefore, the modeling of the production and decay of polarized bosons requires additional care compared to fully off-shell calculations. In practice, enabling a Monte Carlo generator to simulate intermediate electroweak bosons with fixed polarization states involves two main steps: first, the selection of the resonant contribution to the amplitude in a gauge-invariant way—typically via an on-shell projection—and second, the extraction of individual polarization states from the resonant amplitude. For the on-shell projection, two main approximations are commonly employed:

- **Double-Pole Approximation (DPA):** This method retains only the doubly-resonant diagrams and applies an on-shell projection to bring the intermediate bosons onto their mass shell [97, 98].
- **Narrow-Width Approximation (NWA):** This approach assumes a negligible boson width, effectively reducing the propagators to delta functions. Only strictly on-shell contributions are included [99].

To further limit the impact of non-resonant contributions, diagram selection is used to built gauge-invariant subsets of the doubly-resonant amplitude, and the non-resonant diagrams are then treated as background to the resonant signal. Gauge-dependent effects are suppressed by applying a selection criterion that ensures the intermediate bosons are close to on-shell.

Using these approximations calculating polarized cross-sections is possible and well defined, and a huge progress have been made over the past five years by the theory community to provide polarized predictions for the LHC. Fixed-order predictions for polarized diboson production have been developed in several publications [100–105], employing private codes such as MoCaNLO, MulBos, BBMC, and Stripper, among others. In parallel, Monte Carlo event generators matched with parton showers (PS) have as well incorporated polarized matrix elements. For instance, PHANTOM [106] that specializes in $2 \to 6$ processes; MadGraph5 [75] that supports any multiboson final state and can handle multi-jet merging and, more recently, the generation of "polarized" Feynman rules via tailored UFO models for loop-induced processes [107]; Sherpa [108] can also calculate any multiboson final state offers multi-jet merging and parton shower matching at approximated NLO (nLO); and for some selected diboson channels, polarized simulations have been implemented at next-to-leading order QCD within the POWHEG-BOX-RES framework [105]. Table 2.4 provides an overview of these tools, detailing the type of on-shell approximation used, their support for higher-order corrections, and their compatibility with parton-shower matching for event generation.

As mentioned above, since polarization vectors are not Lorentz-invariant, the definition of polarization depends on the choice of frame. Common options include the partonic center-of-mass frame, the laboratory frame, and the diboson center-of-mass frame. The optimal choice is typically guided by experimental considerations, such as reconstruction capabilities. Existing studies (e.g., [113]) indicate that no single frame is universally preferred. Maintaining consistency between theory and experiment is essential therefore the Monte Carlo generators also offer the possibility to provide polarization results for different frames.

The ability to generate polarized events with Monte Carlo simulations has been a key breakthrough for polarization studies, enabling direct investigation of polarization effects at detector level. This allows us to explore correlations not only among the decay products of individual bosons but also between different bosons and across a broad range of observables. As a result, polarization-sensitive analyses are no longer

Tool	OS approx.	LO	loop-ind.	NLO QCD	NNLO QCD	NLO EW	LO+PS	NLO+PS
MoCaNLO [101–104]	DPA	✓	✓	✓	-	✓	-	-
Stripper [109]	DPA	✓	✓	✓	✓	-	-	-
MulBos [110–112]	DPA	✓	✓	✓	-	✓	-	-
BBMC [103, 104]	DPA	✓	-	✓	-	✓	-	-
Sherpa [108]	NWA	✓	-	(✓)	-	-	✓	-
MadGraph [75]	NWA	✓	✓	-	-	-	✓	-
PowHeg-Box [105]	DPA	✓	-	✓	-	-	✓	✓
PHANTOM [106]	DPA	✓	-	-	-	-	✓	-

Table 2.4: Overview of various Monte Carlo tools and their capabilities for simulating polarized cross sections. The table indicates the type of on-shell approximation employed (OS), the ability to compute loop-induced processes (loop-ind.), the available calculation accuracies—including next-to-leading order QCD (NLO QCD), next-to-next-to-leading order QCD (NNLO QCD), and next-to-leading order electroweak corrections (NLO EW)—as well as the possibility of matching to a parton shower at leading order (PS+LO) or next-to-leading order (NLO+PS).

limited to angular distributions, but can now exploit multidimensional kinematic features to enhance sensitivity and improve the extraction of polarization fractions.

2.2.2 Going Beyond Leading-Order: Higher Order Corrections for Polarized Dibosons

Fixed-order calculations for processes involving intermediate polarized bosons at the LHC have seen significant progress in recent years. Inclusive diboson production with leptonic decays is now known at next-to-leading order [101, 102] and even next-to-next-to-leading order (NNLO) in QCD [114]. The calculation of NLO electroweak corrections, more challenging due to photon radiation from both the production and decay stages, has also been achieved for several inclusive processes, such as ZZ [115], inclusive WZ [111, 116], and again WZ but in specific phase-space regions designed to enhance the doubly longitudinal polarization [105, 112]. For WW production, full NLO EW corrections are also available [117–119]. In the case of semi-leptonic diboson decays, NLO QCD corrections are available [103].

In contrast with inclusive dibosons, polarized VBS processes are mostly known only at leading order [98, 113, 120], with a notable exception: the polarized W^+W^+jj scattering process, which has recently been calculated with full NLO QCD and NLO EW corrections[104]. The current status of higher-order corrections for polarized diboson and vector boson scattering processes is summarized in Table 2.5.

Channel	NLO QCD	NLO EW	NLO EW + QCD	NNLO QCD
$W^+(\ell^+\nu_\ell)\,W^-(\ell'^-\bar{\nu}_{\ell'})$	DPA [101]	DPA [117, 118]	DPA [119]	DPA and NWA [114]
$W^\pm(\ell^\pm\nu_\ell)\,Z(\ell'^+\ell'^-)$	DPA [102, 105]	-	DPA [111, 112, 116]	-
$Z(\ell'^+\ell'^-)Z(\ell'^+\ell'^-)$	-	-	DPA [115]	-
$W^\pm(\text{jets})\,Z(\ell'^+\ell'^-)$	DPA [103]	-	-	-
$W^+(\ell^+\nu_\ell)\,W^+(\ell'^+\nu_{\ell'}) + jj$	-	-	DPA [104]	-

Table 2.5: Summary of available higher-order corrections for different diboson processes and the on-shell method used to calculate the cross sections.

From unpolarized calculations, it is well known that higher-order corrections to diboson cross sections can be sizeable. Polarized calculations naturally show similarly large corrections, but with an added layer of complexity: the corrections are polarization-aware. In some cases, specific polarization states receive substantial corrections while others are only mildly affected, meaning that a single, global k-factor is insufficient.

As an example, Figure 2.18 shows the distribution of the absolute rapidity separation between the positron and the Z boson in inclusive WZ production, within a phase space enhanced for doubly longitudinal polarization [112], in the WZ center-of-mass frame. The middle-upper panel displays the ratio of NLO QCD to LO cross sections, while the middle-lower panel shows $\bar{\delta}_{\mathrm{EW}}$, the EW corrections relative to the NLO QCD result, expressed in percent.

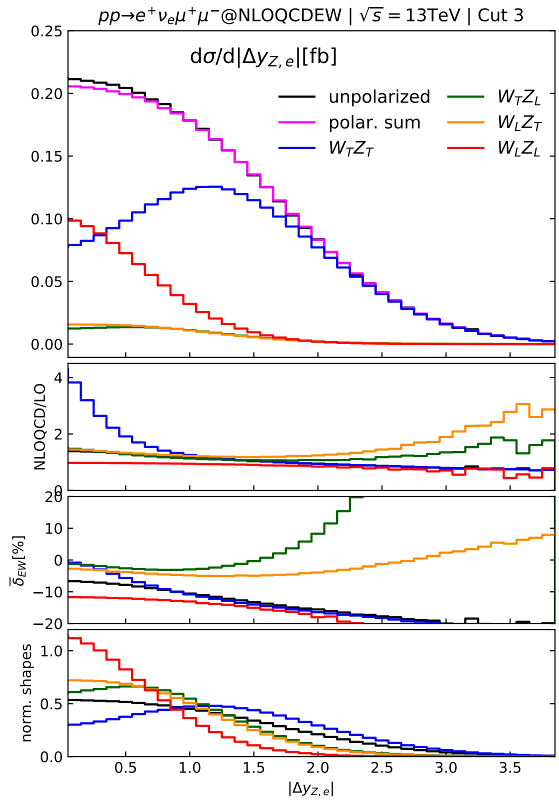

Figure 2.18: Rapidity separation between the e^+ and the Z boson. The main panel shows the NLO QCD+EW cross sections; the upper ratio panel shows NLO QCD over LO; the lower ratio panel shows EW corrections relative to NLO QCD; and the bottom panel shows normalized distributions. Figure taken from [111].

These plots clearly demonstrate that both QCD and EW corrections are not only large but also strongly dependent on polarization and significantly affect the shape of the observable. This underlines the importance of including such corrections in simulations templates when aiming for reliable polarization-dependent cross section measurements.

Unfortunately, fixed-order calculations like the one shown in Figure 2.18, as well as those summarized in Table 2.5, cannot be used directly in experimental analyses, as they do not account for detector effects. For most LHC Run 2 results, the only generators available for simulating polarized signals with parton shower matching were MadGraph and PHANTOM, both limited to leading order accuracy. To work around this, experimental collaborations often relied on reweighting techniques, correcting LO simulated events at truth level bin-by-bin using higher-order predictions and propagating the effects at reconstruction level. While this method can partially recover higher-order effects in selected observables, it also introduces significant theoretical uncertainties.

Bridging this gap between theory calculations and usable inputs for experimental fits remains an important challenge. Recent progress in automating polarized intermediate boson production at approximate nLO QCD accuracy matched to parton showers within the Sherpa framework [108], as well as the first full NLO QCD + PS in PowHeg-Box predictions [121], represent major steps forward.

2.2.3 Experimental Results on Diboson Polarizations

The study of interactions involving polarized massive vector bosons is not a new idea. In particular, there has long been interest in understanding how longitudinally polarized bosons couple to each other and to the Higgs boson through triple ($V_0V_0V_0$, hV_0V_0) and quartic vertices ($V_0V_0V_0V_0$). However, the limited statistics of the available datasets has been a limiting factor for such measurements. While inclusive diboson measurements—as well as the vector boson scattering processes discussed in the previous section—necessarily contain contributions from double longitudinal configurations, the fraction of such events is typically small, generally in the range of 5–10% within commonly used phase spaces.

Due to these limitations, an important early milestone in diboson polarization studies has often been the measurement of events featuring at least one longitudinally polarized boson in the final state V_0V_X ($0X$, with $X = 0, T$). These are typically referred to as single-boson polarization measurements. In parallel, attempts have also been made to isolate events with double longitudinal polarization, V_0V_0 (00) in the final state, known as joint polarization measurements.

The first experimental measurements of diboson polarization were carried out at the LEP collider, where the only accessible diboson process for polarization studies was $e^+e^- \rightarrow W^+W^-$. The LEP collaborations—L3 [122], OPAL [123], and DELPHI [124]—performed single-boson polarization analyses and achieved the first observation of longitudinally polarized W bosons in diboson production. Joint polarization measurements were also attempted by OPAL [125] and DELPHI [126], but the limited statistics prevented them from reaching the sensitivity required for a definitive observation of the longitudinal-longitudinal component.

At the LHC, both single and joint boson polarization measurements have been pursued for various diboson combinations using Run-1 and Run-2 data. These include inclusive production of WZ [127–129] and ZZ [130], as well for the vector boson scattering production of $W^{\pm}W^{\pm}$ [70, 80].

During Run-1 and the early stages of Run-2, no Monte Carlo generator was available to simulate polarized diboson events. Nevertheless, experimental analyses exploited the fact that, at tree level and in the helicity basis, the differential cross section of a decaying boson as a function of the lepton decay angle θ^* can be expressed as a sum of terms, each depending solely on a single polarization fraction [95, 96]. This analytic form enables the extraction of polarization information from unpolarized distributions using fits.

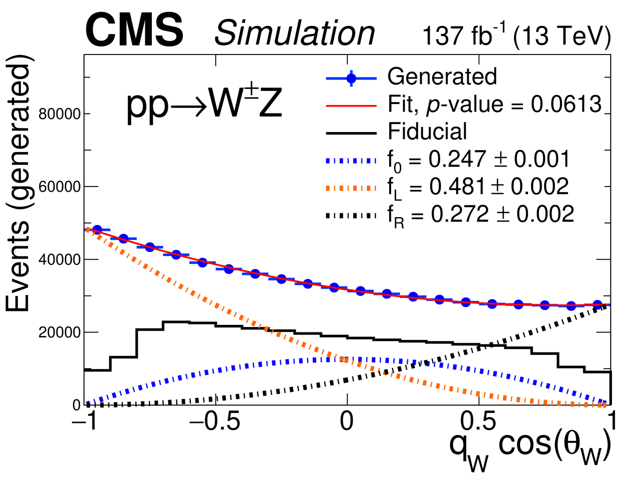

Figure 2.19: Cosine of the W boson polarization angle in the helicity frame at generator level for WZ events in the total phase space. Blue points show MC predictions with statistical uncertainties; the red line is a quadratic fit with polarization components shown as dashed lines. The thick black line shows the distribution in the fiducial phase space, highlighting deviations from the quadratic shape. Figure taken from [127].

An example of such a fit is shown in Figure 2.19 for inclusive WZ production [127]. Because the analytic description is only valid in the total phase space, unpolarized WZ simulations were generated inclusively (shown as blue dots), and the resulting distributions were fitted to extract the W boson's longitudinal (f_0) and transverse ($f_T = f_L + f_R$) polarization fractions (dotted lines). The fitted polarization composition was then used to assign weights to all Monte Carlo events in each bin of $q_W \cos(\theta_W)$, effectively propagating polarization information to the event sample. The same angular distribution in the fiducial phase space is shown as a thick black line. Compare to the fitted templates and the total phase space we can see clear differences, indicating that the analytic expression will fail to describe the polarization effects in the fiducial phase space. The fiducial cuts modify the polarization composition of the total W sample, breaking the simple relation between angular distributions and polarization fractions.

Despite this limitation, the reweighting approach enabled the construction of polarization templates in the fiducial region by propagating weights obtained from the total phase space fit event-by-event into the fiducial phase space. This strategy was used in several Run-1 and early Run-2 analyses [127, 128, 131, 132], leading to the observation (evidence) of single longitudinally polarized Z (W) bosons in WZ production at the LHC. However, this method has important drawbacks: it treats only one boson at a time, ignores spin correlations, preserves only the fitted angular distribution while distorting others, and does not account for off-shell effects. Moreover, its validity degrades once lepton selection cuts or higher-order corrections are introduced.

To address these limitations, more recent Run2 analyses have adopted Monte Carlo tools that simulate polarized dibosons directly, allowing the construction of templates that better capture the full complexity of the process, including spin correlations and interferences [70, 80, 129, 130, 133].

The inclusive WZ [129, 133] and ZZ [130] analyses were the first to use leading-order merged simulations from MadGraph to study polarization at detector level. This represented a significant improvement over reweighting strategies based on analytical formulas. However, LO simulations still fall short in describing inclusive diboson production, which is subject to sizable, shape-dependent next-to-leading order QCD and electroweak corrections.

To mitigate these shortcomings, new reweighting techniques were developed to effectively incorporate NLO QCD and EW effects into the LO templates. Fortunately, fixed-order predictions with polarization dependence described earlier were available, enabling a meaningful a polarization depended reweighting of the LO polarized samples. A particularly innovative technique was introduced in the inclusive WZ analysis in [133], where four deep neural networks (DNNs) were trained to perform multidimensional, event-by-event reweighting. Each DNN targets one of the four joint polarization states (W_0Z_0, W_0Z_T, W_TZ_0, W_TZ_T), they are trained using polarized MadGraph $0, 1j@LO$ events at particle level as input. The trained networks are then applied to unpolarized Powheg+Pythia events simulated at NLO QCD, yielding polarized templates with NLO-like QCD accuracy.

Using this approach and the full Run2 dataset, the simultaneous production of two longitudinally polarized vector bosons was observed in inclusive WZ production and evidence was found in ZZ final states. Table 2.6 presents the measured polarization fractions for inclusive WZ production. The double-longitudinal fraction (f_{00}) accounts for approximately 7% of the selected events, and all the polarization combinations were observed with more than 5 standard deviations.

	Data	**Powheg+Pythia**	**NLO QCD**
		$W^{\pm}Z$	
f_{00}	0.067 ± 0.010	0.0590 ± 0.0009	0.058 ± 0.002
f_{0T}	0.110 ± 0.029	0.1515 ± 0.0017	0.159 ± 0.003
f_{T0}	0.179 ± 0.023	0.1465 ± 0.0017	0.149 ± 0.003
f_{TT}	0.644 ± 0.032	0.6431 ± 0.0021	0.628 ± 0.004

Table 2.6: Measured and predicted polarization fractions for $W^{\pm}Z$ inclusive events [133].

While the observation of two longitudinal bosons is a milestone, a key question remains: do these bosons actually interact with each other? Specifically, are we sensitive to s-channel involving the triple $W_0 W_0 Z_0$ vertex, or is the observed f_{00} fraction dominated by t-channel processes, where longitudinal bosons are radiated independently and do not interact with each other?

To investigate the correlations between the two bosons, the ratio

$$R_c = \frac{f_{00}}{f_0^W f_0^Z}.$$

is introduced. In the absence of spin correlations (neglecting interference), $R_c = 1$. The Standard Model at NLO QCD predicts $R_c = 1.3$, while the measured value is:

$$R_c = 1.54 \pm 0.35.$$

The significance relative to the uncorrelated hypothesis is 1.6 standard deviations, indicating that current data remain compatible with the assumption that the polarizations of the two bosons are independent. In other words, even though we can now measure joint polarizations, we're not yet seeing clear signs of interactions between longitudinally polarized bosons.

That was a bit of a letdown—but not the end of the story. To push further, we turned to theory-driven strategies aimed at amplifying the more subtle features of WZ polarization. In the PhD work of Jan-Eric Nitschke [134], we studied restricted phase spaces designed to reveal the intricate gauge cancellations predicted by the Standard Model, particularly in the transversely polarized configurations. In the same study, we also identified regions that enhance the doubly longitudinal (00) fraction up to 25%. The results were published in [129], and I will delve further into our contributions in the next section.

Before diving into those details, it's worth highlighting the first experimental milestones toward measuring longitudinal interactions in vector boson scattering. Although VBS analyses are still statistically limited, the first of such measurements came from the same-sign $W^\pm W^\pm jj$ channel [70, 80], where the ATLAS collaboration achieved the first evidence for longitudinally polarized W bosons in electroweak production. While sensitivity to the fully longitudinal (00) signal remains constrained by available statistics. As for the WZ VBS channel, no polarization measurements have been published so far. However, we performed initial sensitivity studies as part of Anna Tegetmeier's Master thesis [135]. These reconstruction-level studies suggest that with the current LHC dataset, it may already be possible to reach evidence for single-boson polarization in the WZ channel. That said, probing joint polarization components—especially the doubly longitudinal (00) state—will require the enhanced statistical reach of the HL-LHC.

Now, let's turn to the energy dependence of inclusive WZ polarization fractions, and see what further insights can be drawn from this analysis.

Energy dependence of inclusive WZ polarization fractions

In this study, we explored how the polarization fractions of WZ diboson pairs evolve with energy, focusing on two distinct fiducial regions. One is optimized to measure the Radiation Amplitude Zero (RAZ) effect, which emerges in events with two transversely-polarized bosons, while the second is enriched in events featuring two longitudinally-polarized bosons [136, 137].

The RAZ effect is a leading-order phenomenon predicted for WZ and $W\gamma$ production processes. In the case of WZ production, which proceeds through s-, t-, and u-channel quark-antiquark interactions, the dominant helicity amplitude for two transversely-polarized bosons vanishes precisely when the W boson scattering angle in the WZ rest frame reaches 90° with respect to the incoming antiquark direction [136, 137]. This exact cancellation arises from the gauge structure of the Standard Model and leads to a dip at $\cos\theta_W = 0$—or equivalently, around zero in the $\Delta Y(WZ)$ distribution, where ΔY is the rapidity difference between the W and Z bosons.

Figure 2.20 illustrates this beautifully. In the leading-order prediction shown in Figure 2.20(a), a clear dip appears in the $\cos\theta_W$ distribution for the transversely-polarized (TT) component. But as seen in Figure 2.20(b), this dip starts to fade when moving to a merged LO+1 jet prediction, which incorporates higher-order QCD effects. These corrections essentially "fill in" the dip, reducing the RAZ visibility.

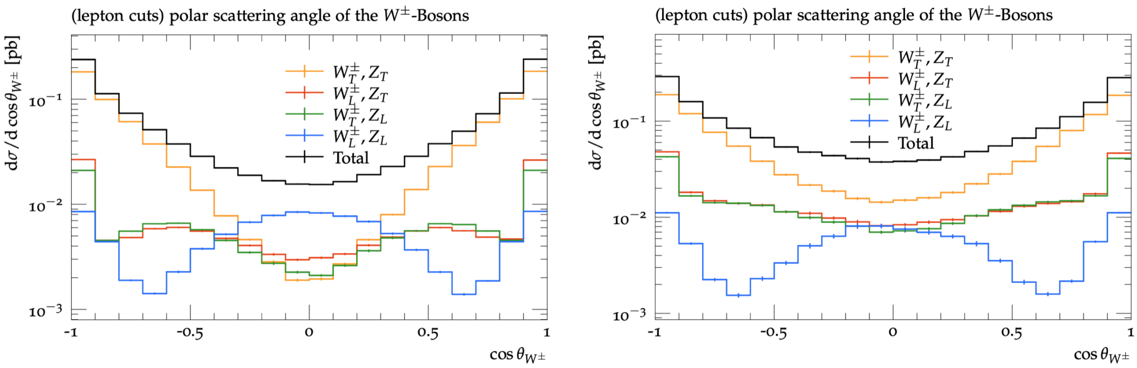

(a) (b)

Figure 2.20: Generator-level $\cos\theta_W$ distributions in the WZ rest frame after lepton selections. (a) Leading-order prediction; (b) LO+1 jet merged sample. Figures taken from [138].

The RAZ effect has already been studied and observed in $W\gamma$ final states [139–141], where it even enhances the sensitivity to potential resonances in the radiation valley [142]. But for WZ, it's trickier—since the Z boson can be either longitudinally or transversely polarized (unlike the photon, which is always transverse) [143]. On top of that, next-to-leading order QCD corrections dilute the effect, making it difficult to observe experimentally [144, 145].

To improve our sensitivity to this Standard Model signature in WZ production, we defined a more LO-like phase space by placing an upper cut on the transverse momentum of the WZ system, denoted p_T^{WZ}. We used thresholds at 20, 40, and 70 GeV. The tighter the cut, the closer we are to LO-like kinematics, and the more visible the dip becomes. As a bonus, this also makes our analysis less sensitive to higher-order effects not captured by the LO+1 jet MADGRAPH simulation.

Experimentally, this analysis was realized in the fully-leptonic WZ final state: three isolated electrons or muons, along with moderate missing transverse energy. Thanks to this clean signature, only about 10% of the events come from background processes, which we estimated using a mix of data-driven methods (for fake/Non-prompt leptons) and MC simulation (for prompt leptons).

The signal definition focused exclusively on the $W_T Z_T$ component. We treated all other polarization states as background and measured the differential fiducial cross section of $|\Delta Y(WZ)|$ in bins of p_T^{WZ}. Figure 2.21(a) compares the unfolded data to the SM prediction for the TT component in the $p_T^{WZ} < 70$

GeV region. To quantify the RAZ dip, we introduced a variable $\mathcal{D}$, defined as

$$\mathcal{D} = 1 - 2 \times \frac{N^{\text{unf}}_{\text{central}}}{N^{\text{unf}}_{\text{sides}}},$$

where $N^{\text{unf}}_{\text{central}}$ is the number of unfolded events with $|\Delta Y(WZ)| < 0.5$, and $N^{\text{unf}}_{\text{sides}}$ counts those in the range $0.5 < |\Delta Y(WZ)| < 1.5$. A positive $\mathcal{D}$ value indicates a dip, zero means a flat distribution, and a negative value would signal an excess. As shown in Figure 2.21(b), all measured $\mathcal{D}$ values are significantly above zero across the different p_T^{WZ} selections, indicating the presence of the RAZ dip at $|\Delta Y_{WZ}| = 0$.

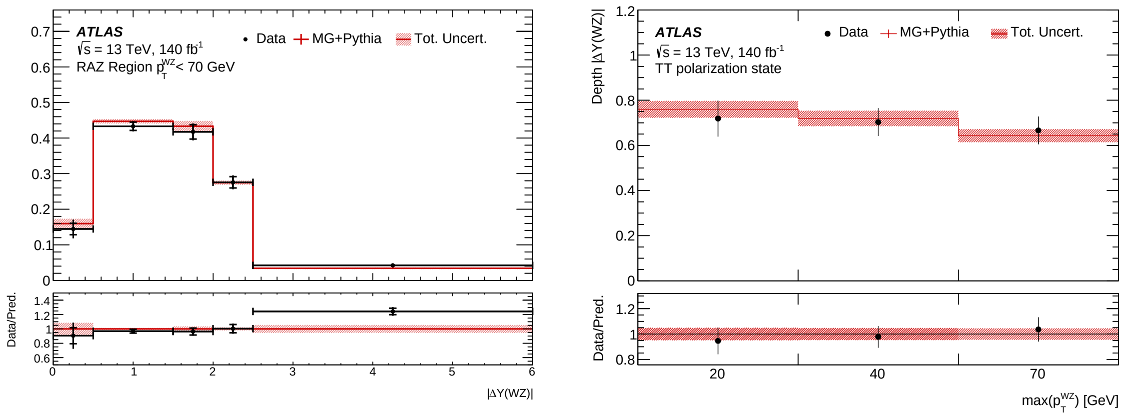

(a) (b)

Figure 2.21: (a) Comparison between the 00+0T+T0-subtracted normalized unfolded $|\Delta Y(WZ)|$ distribution and the SM prediction for the TT component, for $p_T^{WZ} < 70$ GeV; (b) Measured dip depth $\mathcal{D}$ as a function of the p_T^{WZ} cut. All values are positive, indicating a persistent dip at $|\Delta Y(WZ)| = 0$. Figures published in [129].

Detecting the RAZ dip was a real milestone not only for testing polarization sensitive predictions of the Standard Model, but also because it gave us access to a phase space where the $W_T Z_T$ component is suppressed. That opened the door to our next goal: constructing a region with a sizeable double-longitudinal fraction, ideally at high transverse momenta, where the Goldstone Boson Equivalence Theorem applies and longitudinal bosons behave like Goldstone bosons. To achieve this, we applied two additional cuts on top of the inclusive selection: we kept the $p_T^{WZ} < 70$ GeV requirement (to suppress TT), and pushed into higher-momentum regions by requiring either $100 < p_T^Z \leq 200$ GeV or $p_T^Z > 200$ GeV. These high-p_T^Z bins enhance the 00 contribution, providing better sensitivity to this polarization state.

Figure 2.22 shows detector-level distributions in the 00-enhanced signal regions. While the statistics are limited due to the strict p_T^Z requirements, the fraction of doubly-longitudinal bosons increases to above 15% in both regions. To enhance sensitivity to the 00 component, two Boosted Decision Trees were trained—one for each p_T^Z region—to separate 00 from other polarization states. Figure 2.22(a) displays the BDT output for the $100 < p_T^Z \leq 200$ GeV region. While Figure 2.22(b) shows the vector boson scattering angle $\cos\theta_V$ for the region with $p_T^Z > 200$ GeV. Given the limited statistics and the similar shape of the BDT output for $W_0 Z_T$ and $W_T Z_0$, these contributions are merged into a single term in the figures, with their relative ratio fixed to the SM prediction.

To measure the polarization fractions, binned maximum-likelihood fits [146] are performed using the BDT distributions in the two signal regions, independently, each with three free parameters. The results are

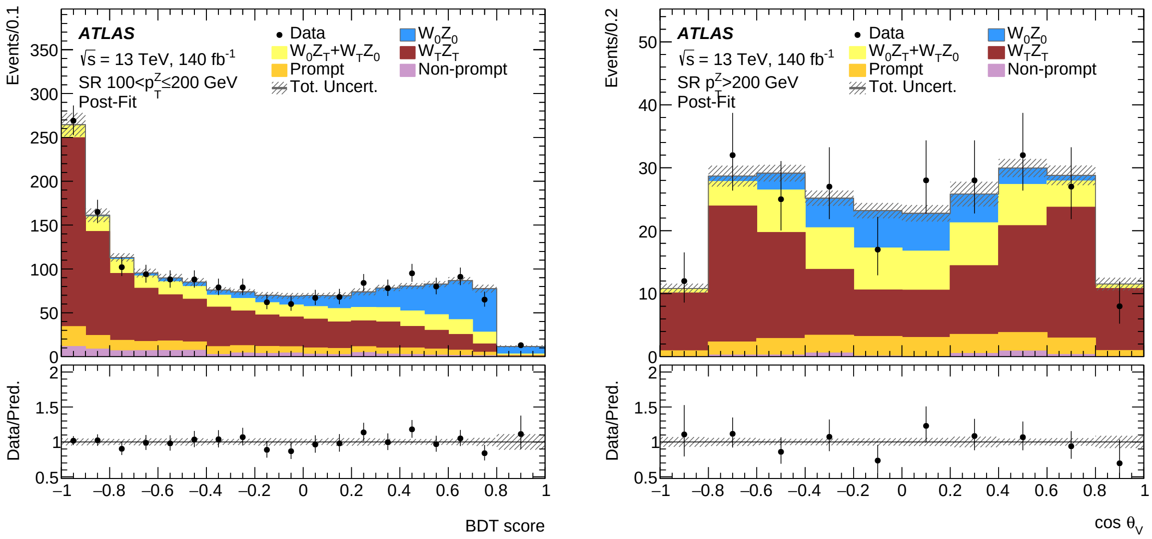

(a) (b)

Figure 2.22: The comparison between the data and the post-fit SM predictions for (a) the BDT distribution in the $100 < p_T^Z \leq 200$ GeV region and (b) the vector boson scattering angle $\cos\theta_V$ for the region with $p_T^Z > 200$ GeV. The bottom panels show the ratios of the data to the post-fit SM predictions. The uncertainty bands include both the MC statistical and systematic uncertainties.

shown in Table 2.7, alongside the predicted fiducial polarization fractions. The predictions are calculated at particle level in a fiducial phase space matching the event selection, using MADGRAPH 0,1j@LO samples reweighted to include higher-order QCD effects and NLO electroweak corrections [112]. We observe a 5.2 standard deviation significance for double-longitudinal bosons in the $100 < p_T^Z \leq 200$ GeV region, surpassing the observation threshold. In the highest p_T region, however, statistics are still insufficient to reach observation with only 1.6 standard deviation measured.

	Measurement			**Prediction**	
	$100 < p_T^Z \leq 200$ GeV	**$p_T^Z > 200$ GeV**		**$100 < p_T^Z \leq 200$ GeV**	**$p_T^Z > 200$ GeV**
f_{00}	$0.19\ ^{+0.03}_{-0.03}$ (stat) $^{+0.02}_{-0.02}$ (syst)	$0.13\ ^{+0.09}_{-0.08}$ (stat) $^{+0.02}_{-0.02}$ (syst)	f_{00}	0.152 ± 0.006	0.234 ± 0.007
f_{0T+T0}	$0.18\ ^{+0.07}_{-0.08}$ (stat) $^{+0.05}_{-0.06}$ (syst)	$0.23\ ^{+0.17}_{-0.18}$ (stat) $^{+0.06}_{-0.10}$ (syst)	f_{0T}	0.120 ± 0.002	0.062 ± 0.002
f_{TT}	$0.63\ ^{+0.05}_{-0.05}$ (stat) $^{+0.04}_{-0.04}$ (syst)	$0.64\ ^{+0.12}_{-0.12}$ (stat) $^{+0.06}_{-0.06}$ (syst)	f_{T0}	0.109 ± 0.001	0.058 ± 0.001
f_{00} obs (exp) sig.	5.2 (4.3) σ	1.6 (2.5) σ	f_{TT}	0.619 ± 0.007	0.646 ± 0.008

Table 2.7: Measured diboson polarization fractions in the two signal regions with $p_T^{WZ} < 70$ GeV and $100 < p_T^Z \leq 200$ GeV or $p_T^Z > 200$ GeV using three unconstrained parameters. The SM predicted fractions for all four polarization states are also shown.

Returning to our original question: are we seeing longitudinal bosons interact with each other?

The spin correlation R_c was evaluated in the $100 < p_T^Z \leq 200$ GeV region—where we reached observation—using an extended analysis from Jan-Eric's thesis [134], which further split the data according to the decay angle to better separate mixed polarization states. The uncorrelated hypothesis were the longitudinal W and Z bosons do not interact is rejected with a significance of 2.8 standard deviations (2.1 expected), just short of the 3σ threshold required to claim evidence. Nevertheless, this result suggests that additional data from Run-3 and future LHC runs could be sufficient to cross this threshold. We are now getting closer than ever to directly observing longitudinal boson interactions and probing this way the dynamics of electroweak symmetry breaking.

I must say, this analysis was easily one of the most innovative—and honestly, one of the most fun—I've ever had the chance to work on. It was a first-of-its-kind effort where everything from signal regions to deliverables had to be defined from scratch.

2.2.4 What Have We Learned from Polarized Diboson Measurements?

Over the past few years, significant progress has been made in the study of diboson polarization. On the theoretical side, developments in the understanding and calculation of helicity amplitudes have enabled the production of polarized Monte Carlo predictions and next-to-leading order (NLO) polarized calculations. On the experimental side, advanced analysis techniques have been developed to exploit polarization-dependent kinematic correlations, allowing for better separation of the different polarization states in data.

The ultimate goal of polarization measurements is to directly probe the interactions between longitudinally polarized vector bosons, both among themselves—via triple ($V_0V_0V_0$) and quartic ($V_0V_0V_0V_0$) gauge couplings—and with the Higgs boson through vertices such as hV_0V_0 and hhV_0V_0. As discussed in the previous sections, vector boson scattering processes are the most natural environment to study such interactions. However, current vector boson scattering measurements are still statistically limited, and it is not yet possible to decompose the signal into polarization-specific contributions in a way that allows a joint-polarization interpretation. Nevertheless, first steps have been taken in the same-charge $W^{\pm}W^{\pm}$ analyses, achieving evidence for single-polarization—i.e., the presence of at least one longitudinal W in $W^{\pm}W^{\pm}jj$ production [70, 80].

In contrast, inclusive diboson production—with cross sections roughly an order of magnitude larger than those of VBS—offers a more statistically powerful environment to begin probing these interactions. First joint-polarization measurements have now been published, reporting for the first time the observation of two longitudinally polarized bosons produced in LHC collisions [128, 129]. While we are not yet in a position to confirm whether their interactions and spin correlations match Standard Model expectations, this marks a major milestone. Thanks to the higher statistics in inclusive diboson samples, it is now becoming possible to focus on specific regions of phase space—such as those where the Goldstone Boson Equivalence Theorem is expected to apply, or where effects like the Radiation Amplitude Zero may become visible. In other words, we are approaching the point where polarization-sensitive measurements in inclusive diboson production will offer the first direct window into polarized boson interactions.

For VBS processes, projection studies currently indicate that joint-polarization measurements—i.e., resolving the V_0V_0 final states—will require the increased luminosity of the HL-LHC to achieve meaningful sensitivity. Nevertheless, the groundwork has already been laid. The first measurements from Run 2 have demonstrated the feasibility of both single- and joint-polarization analyses, providing crucial validation of the analysis strategies and the necessary tools.

There is still much to do. We cannot yet confirm that longitudinal bosons and the Higgs interact precisely as predicted by the Standard Model, but we are steadily moving closer to that goal. Looking ahead, polarization-based analyses are expected to play an increasingly important role—not only in precision tests of the Standard Model, but also in enhancing sensitivity to possible new physics effects. Such effects may preferentially affect specific polarization states and could have remain hidden in inclusive measurements unless the polarization dimension is explicitly considered.

2.3 Summary

This chapter covers a particularly exciting period in particle physics. The era of discovering the particle zoo is over—all particles predicted by the Standard Model have been observed—and we are now beginning to probe its inner workings, reaching into the very heart of Electroweak Symmetry Breaking.

The discovery of the Higgs boson, followed by precise measurements of its couplings to bosons and fermions, suggests that the Higgs mechanism is indeed the way nature realizes Electroweak Symmetry Breaking. But to truly confirm this, we must understand the dynamics of this sector. Over the past years, I have focused on measurements designed to reveal these dynamics. This can be achieved by studying some of the rarest processes accessible at the LHC: vector boson scattering and diboson polarization. These offer a unique window not only into the mechanism that gives mass to the $W^{\pm}$ and Z bosons, but also into the structure of the Standard Model at high energies—allowing us to test the Higgs sector beyond the on-shell mass, and to probe the gauge interactions in regimes never before explored.

Looking back at Run 2, we can clearly see how collective efforts have pushed the field forward. The first observations of vector boson scattering—or more precisely, the electroweak production of dibosons—have matured into differential cross-section measurements. In parallel, polarization analyses have begun, first in inclusive diboson production, pushing the experimental machinery to new levels and revealing the behavior of polarized W and Z bosons in unprecedented detail [70, 80, 128–130, 135].

These advances have been driven not only by the growing LHC dataset, but also by theoretical developments and increasingly sophisticated multivariate analysis techniques, which allow us to extract subtle correlations from the data. Over these years, strong collaborations between experimentalists and theorists have formed, proving essential for refining predictions and interpreting results. This synergy has been instrumental in unlocking the full potential of polarization-sensitive observables.

So far, the Standard Model continues to pass these tests with remarkable precision: its predictions hold up, and the weak bosons behave exactly as expected. Yet we know this is not the end of the story. In the next chapter, we turn to the search for new physics—exploring how the very same diboson processes, which confirm the Standard Model's structure, can also serve as powerful probes for what may lie beyond.

3 Looking for Physics Beyond the Standard Model

"Tiens, j'ai cru voir passer un lapin. J'ai rêvé, tu crois ?"

— Fabrice Melquiot, *Alice et autres merveilles*

In the previous chapter, we explored how recent experimental and theoretical advances have allow us to test the Standard Model with unprecedented precision. Yet, despite its tremendous success, the Standard Model leaves many fundamental questions unanswered. In this chapter, we take a step further and use our boson pairs as a window into the unknown.

There are compelling reasons to believe that the Standard Model is not the ultimate theory of nature. Some of its most striking shortcomings come from experimental observations it cannot explain. Neutrino oscillations, for instance, demonstrate that neutrinos must have mass, contrary to SM predictions [147]. Another major shortcoming is the SM's inability to describe about 95% of the Universe's energy content. While around 23% is attributed to dark matter and 72% to dark energy, the SM offers no candidate for either. Attempts to estimate the vacuum energy from the SM fields result in a discrepancy with observations by more than 100 orders of magnitude — probably one of the worst theoretical predictions in physics to date.

Moreover, the Standard Model provides no explanation for the structure of its own gauge symmetries[1], the existence of three generations of fermions, or the wide span of their masses. It includes 19 free parameters that must be fixed by experimental input, with no deeper rationale for their values. One of the most pressing theoretical concerns is the hierarchy problem. Quantum corrections to the Higgs boson mass are sensitive to new physics at high energy scales. If the SM is valid up to, say, 10 TeV, extreme fine-tuning is required to keep the Higgs mass at its observed value around 125 GeV. This situation is considered unnatural, and therfore push for new physics solutions at a lower energy scale — a problem that many beyond-the-Standard-Model theories attempt to address.

For example, composite Higgs models postulate that the Higgs is not an elementary particle, but a bound state of a new strong interaction, dynamically generating its mass and protecting it from large corrections. These models typically predict new heavy resonances, such as vector-like fermions or extended gauge bosons, possibly accessible at the TeV scale.

To address the hierarchy problem, dark matter, and other open questions, many theoretical frameworks have been proposed — from supersymmetry to extra dimensions, to extended Higgs sectors and new gauge symmetries. As it is unfeasible to test the full breadth of these models directly, experimental searches often rely on simplified benchmark models capturing key features of a broader class of theories.

[1] I probably said that gauge symmetries were crucial and they are in the SM, but why they are as they are?

When it comes to searching for new physics, two main strategies emerge. The first is **direct searches** — looking for new particles produced in high-energy collisions, such as resonances decaying into visible particles that can be measured. This approach benefits from clean experimental signatures a resonance appearing in the data but is limited by the available center-of-mass energy. The second approach is **indirect searches**: assumes that new physics is beyond available experimental energy reach and looks for deviations from the SM in precision measurements, rare processes, or the tails of kinematic distributions. Such deviations, if observed, can hint at the presence of heavy new physics that cannot be produced directly. To interpret these subtle effects consistently across different processes, the Effective Field Theory approach is typically used. EFT provides a model-independent framework where new physics is encoded in higher-dimensional operators, suppressed by a characteristic energy scale. This approach ensures theoretical consistency and allows us to connect different observables in a unified language.

This chapter presents my contributions to the searches efforts. In the first part, I focus on direct searches for new resonances decaying into vector boson pairs—final states particularly sensitive to scenarios involving new heavy particles coupling to the electroweak sector. In the second part, I turn to an indirect strategy based on the Effective Field Theory framework. By systematically parameterizing possible deviations from SM interactions in a model-independent way—even in the absence of direct discoveries.

In both cases, vector boson pairs act as powerful probes. Whether produced via resonant decays or through anomalous interactions, their kinematic properties carry imprints of physics beyond the SM. By combining these complementary strategies, we aim to leave no stone unturned in our exploration.

These studies are the result of collaborative efforts carried out during my postdoctoral fellowship in Dresden and more recently during my Junior Professor Chair in Toulouse, working with brilliant young researchers: Abhishek Nag [148], Stefanie Todt [60], and Anna Tegetmeier. Together, we tackled many facets of this quest — from selection optimization, MC simulation to the statistical analysis.

We know new physics must be out there — perhaps not hiding in plain sight, but in the corners of our data. Let's go and look for it!

3.1 Direct searches: Diboson resonance searches

Beyond confirming known physics, boson pairs serve as windows into the unknown. Their interactions could reveal the presence of new particles or forces. If such particles couple to weak bosons, they might decay into boson pairs, leaving distinctive signatures in the data.

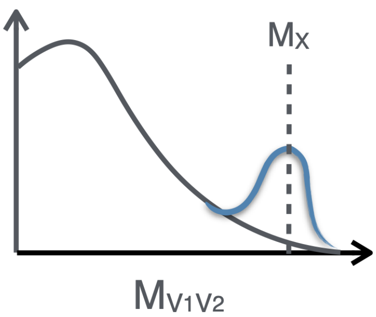

Figure 3.1: Schematic representation of an observable effect when a hypothetical heavy particle X with mass M_X is produced within the energy reach of the LHC.

A powerful strategy is to directly search for new particles in collision events — particles not predicted by the Standard Model. Imagine, for instance, the existence of a massive new particle X that we haven't yet discovered. It would be hard to imagine that such a particle had no involvement in weak interactions. If it does couple to W or Z bosons, it could decay — with some unknown but non-zero probability — into a pair of them. By reconstructing the invariant mass of these boson pairs, $m_{V_1V_2}$, we gain direct access to the possible mass of this new particle (see Figure 3.1). And since vector boson pairs are relatively rare in proton-proton collisions, they offer a relatively clean signature with manageable background.

But there's a catch: we don't observe W and Z bosons directly. Instead, we reconstruct them from their decay products. Up to this point, we've focused mostly on leptonic channels because of their clean signatures and low backgrounds are extremely useful for SM measurements. However, as shown in Table 1.1, over 60% of vector bosons decay hadronically. Hadronic channels at the LHC come with larger backgrounds — especially from QCD — but they compensate with a significantly higher statistics, which translate into better sensitivity at high masses.

For a robust resonance search, it's essential to consider all possible final states: fully leptonic, semi-leptonic, and fully hadronic. Each channel brings different strengths to the table. For example, Figure 3.2 shows 95% CL exclusion limits on the production cross section of a hypothetical W' boson decaying to WZ, as obtained from different final states. At lower masses (below 1.1 TeV), the fully leptonic channel ($WZ \to \ell\nu\ell\ell$, red dashed line) dominates thanks to its low background, but its sensitivity drops off quickly due to limited statistics, and some reconstruction issues for boosted leptonic decays. The fully hadronic channel (blue line), becomes competitive above 1.6 TeV, where its statistical power starts to shine. Finally, the semi-leptonic channel ($WZ \to \nu\nu qq, \ell\nu qq, \ell\ell qq$) offers a sweet middle ground — balancing manageable backgrounds with sufficient statistics — and provides the best sensitivity at the highest masses.

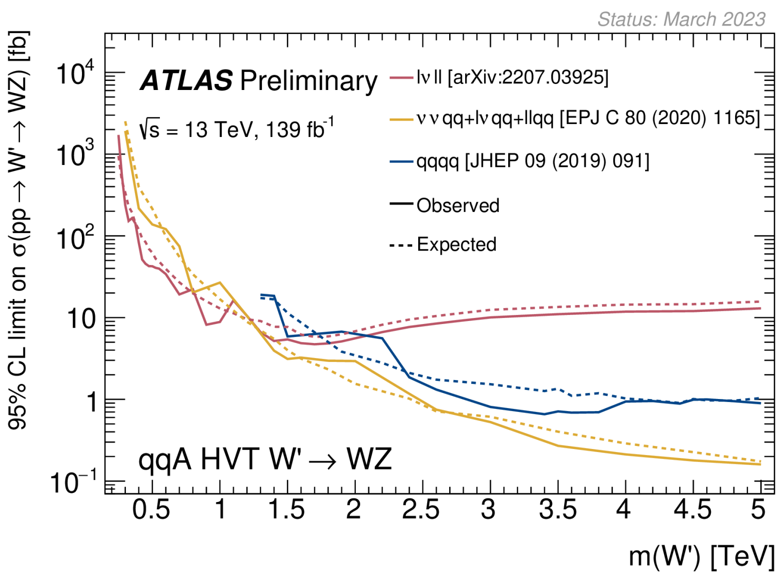

Figure 3.2: Exclusion limits for a HVT W' in diboson resonance searches conducted by ATLAS with the full Run 2 dataset: observed and expected 95% CL upper limits on the cross-section times branching fraction to WZ, in the quark-anti-quark Annihilation production mechanisms, are overlaid for individual analyses. Figure published in [149]

Up to now, we've treated resonance searches as largely model-independent — taking any pair of bosons, computing their invariant mass, and hoping something unexpected pops out. But given the known limitations (and remarkable successes!) of the Standard Model, it makes sense to be a bit more strategic and use a model to guide our search. A rich landscape of theories has been proposed to address its open questions. Some tackle specific issues like the hierarchy problem or dark matter, while others propose more radical changes, such as supersymmetry or composite Higgs models. These theories introduce new particles and interactions that can serve as benchmark models — helping us design more targeted and effective searches.

3.1.1 Models Beyond the Standard Model

The limitations of the Standard Model motivate the ongoing search for a more complete theoretical framework. Among the many proposed scenarios, composite Higgs models offer an elegant solution to the hierarchy problem by interpreting the Higgs boson as a composite state rather than an elementary particle. While the space of Beyond the Standard Model theories is vast, experimental analyses typically rely on a set of representative benchmark models that capture the essential features of broader frameworks. In this section, two such benchmarks are discussed: the Heavy Vector Triplet (HVT) models [150] and the Georgi-Machacek (GM) model [151, 152]. These scenarios encapsulate characteristic theoretical features such as extended gauge symmetries or non-minimal scalar sectors and are used to interpret experimental results in diboson final states.

Heavy Vector Triplet (HVT) Models

The HVT framework provides a simplified Lagrangian description of spin-1 resonances, often arising in composite Higgs or extra-dimensional models. These new heavy partners of the W and Z bosons (denoted W' and Z') couple to Standard Model fermions and bosons with a small set of free parameters [153–155]. In particular, the coupling to longitudinally polarized vector bosons and the Higgs field is governed by the product $g_V c_H$, while couplings to fermions are parameterized by $(g^2/g_V)c_F$, where g is the SU(2) coupling of the Standard Model. The parameter g_V characterizes the strength of the new vector interactions, and c_H, c_F are typically $O(1)$. Adjusting these parameters allows the HVT framework to accommodate a range of theoretical scenarios.

Three benchmark implementations are commonly used to represent different coupling regimes and production mechanisms:

- **Model A**: Represents scenarios with extended gauge symmetries and sizable couplings to fermions. The parameters are set to $g_V = 1$, $c_F = 1$, with universal fermion couplings.
- **Model B**: Typical of strongly-coupled scenarios like composite Higgs models, where couplings to fermions are suppressed and decays to bosons dominate. Here, $g_V = 3$, with $c_F = 1$.
- **Model C**: Tailored for the vector boson fusion (VBF) production of HVT states, expected to have a smaller cross-section. It sets $g_V = c_H = 1$, with all other couplings, including c_F, set to zero to enhance VBF sensitivity.

These benchmarks provide a robust framework to interpret searches for resonances decaying into vector boson pairs, allowing results to be translated into exclusion contours or discovery reach in the HVT parameter space.

The Georgi-Machacek Model

The Georgi-Machacek (GM) model [151, 152] extends the SM Higgs sector by introducing one real and one complex SU(2) triplet in a way that preserves custodial symmetry [156], thus maintaining the tree-level prediction $\rho \simeq 1$. The physical scalar spectrum includes new neutral and charged Higgs bosons, among them doubly-charged states and a custodial fiveplet $(H_5^{++}, H_5^{+}, H_5^{0}, H_5^{-}, H_5^{--})$ that is fermiophobic but couples to W and Z bosons. The model also contains a triplet and two custodial singlets, one of which corresponds to the observed 125 GeV Higgs boson.

A key parameter, $\sin\theta_H$, characterizes the triplet contribution to electroweak symmetry breaking and modifies the couplings of the physical Higgs states to gauge bosons. The GM model is particularly interesting from a phenomenological perspective as it predicts enhanced rates for vector boson fusion and Higgs pair production, which are sensitive probes of the electroweak symmetry breaking mechanism.

The GM model exemplifies how a non-minimal scalar sector can modify Standard Model predictions and introduce new experimental signatures, making it a valuable benchmark in the interpretation of diboson and multiboson searches.

While neither the HVT nor GM model represents a unique solution to physics beyond the Standard Model, both offer well-defined, theoretically motivated frameworks. They allow experimental results to be interpreted in a meaningful way and facilitate the translation of null results into stringent constraints on the broader BSM parameter space.

3.1.2 Experimental Results on Diboson Resonance Searches

Exclusion limits from searches for diboson resonances across different final states are summarized in Refs.[157–159]. These results include analyses of heavy VV and VH vector resonances ($V = W$ or Z), covering Run 1 and Run 2 datasets and probing a wide range of final states: fully hadronic ($qqqq$), semileptonic ($\ell\nu qq$, $\ell\ell qq$, $\nu\nu qq$), and fully leptonic ($\ell\ell\ell\ell$, $\ell\nu\ell\ell$, $\ell\ell\nu\nu$)[160–166].

The fully hadronic [164] and semileptonic [162] channels are statistically powerful due to their larger branching ratios, but they face significant backgrounds, particularly from QCD multijet production. Other subdominant but non-negligible sources include W/Z+jets, top-quark pair and single-top production, and SM diboson processes. To improve sensitivity, these analyses are divided into two reconstruction regimes: the resolved category, where the hadronic decay products of the vector boson are reconstructed as two distinct small-radius jets, and the boosted category, where the decay products are collimated into a single large-radius jet due to the high momentum of the boson. The latter makes use of advanced grooming and jet substructure techniques to identify hadronically decaying W and Z bosons.

In the semileptonic channels [162], where one boson decays leptonically and the other hadronically, the background is lower compared to the fully hadronic case, while still benefiting from a relatively high signal yield. These channels also profit from better mass resolution on the leptonic side and are particularly useful for accessing intermediate mass ranges. Recent analyses have incorporated machine learning classifiers for signal discrimination and improved jet tagging techniques, significantly enhancing sensitivity.

In contrast, fully leptonic channels—though limited by smaller branching ratios—offer excellent background suppression and superior invariant mass resolution, making them particularly well-suited for precision measurements and searches in regions where backgrounds dominate in hadronic or semi-leptonic channels. Given my contributions to the Standard Model diboson analyses described earlier, my work on resonance searches has naturally focused on these channels. The $WZ \to \ell\nu\ell\ell$ final state was used to extract exclusion limits on the three HVT benchmark models [167].

Constraints on the Georgi-Machacek (GM) model have also been set using the same WZ analysis [167], as well as from an earlier ATLAS analysis of opposite-sign WW production [168]. Searches by the CMS Collaboration [66, 169] for singly and doubly charged Higgs bosons—produced via VBF and decaying

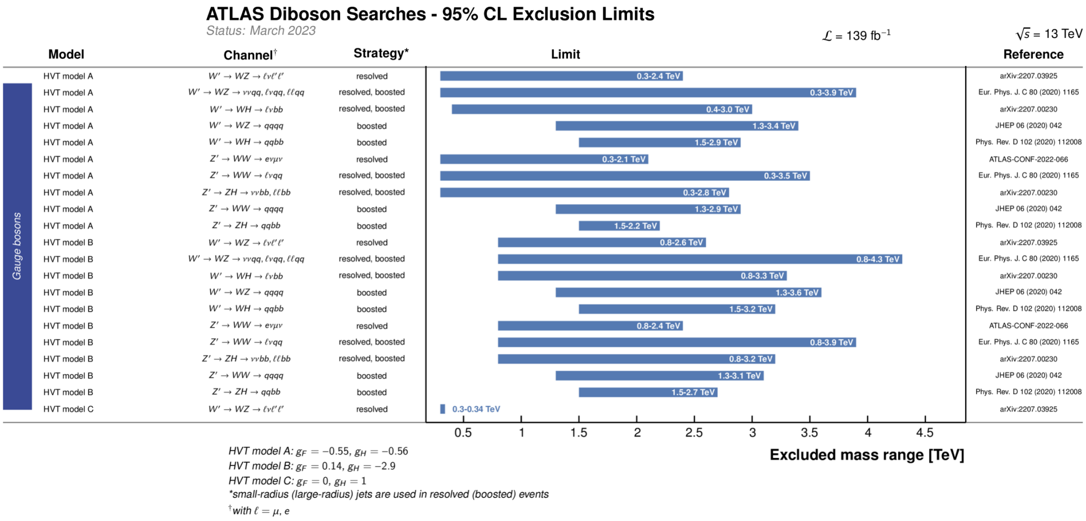

Figure 3.3: Summary of the mass exclusion limits at 95% confidence level from ATLAS diboson searches on the W' and Z' as predicted by the HVT benchmarks. Figure adapted from [149].

respectively into WZ and WW in fully leptonic final states—have also yielded exclusion limits on the coupling parameter of the GM model, under the assumption of degenerate masses for $H_5^{\pm}$ and $H_5^{\pm\pm}$. More recently, the same-sign $W^{\pm}W^{\pm}$ channel, studied in the context of vector boson scattering, has further constrained GM model parameters [71, 169].

Figure 3.3 presents a summary of exclusion limits on W' and Z' masses at 95% confidence level, from various ATLAS diboson searches based on Run 2 data. As discussed, different channels exhibit complementary sensitivity depending on the boson decay modes and resonance mass. An interesting case is the short energy reach observed for HVT Model C, which appears only once in the figure. This is expected, as Model C predicts a fermiophobic W' produced solely via vector boson fusion—a process with low cross-section. Moreover, the only search sensitive to this signature so far is the fully leptonic WZ channel, which itself has limited reach due to branching ratio and acceptance. It's a reminder that high-mass exclusions do not imply that all BSM scenarios are ruled out—some may simply remain out of reach in corners of the phase space that are experimentally challenging.

In the next section, I present the WZ fully leptonic resonance search, the analysis to which I have contributed most directly.

WZ Fully Leptonic Resonance Search

This search targets resonances decaying to WZ in final states with three charged leptons (e or μ) and missing transverse momentum, arising from fully leptonic decays of the vector bosons. Two production mechanisms are considered: the Drell–Yan process ($q\bar{q} \to WZ$) and the vector boson fusion (VBF) process ($pp \to W'jj \to WZjj$).

The analysis uses a cut-based selection to define the Drell–Yan signal region and an artificial neural network (ANN) for the VBF selection. The invariant mass of the WZ candidate, reconstructed using the leptons and the missing transverse energy, is used as the final discriminant in the statistical analysis.

In the VBF topology, similar to that of VBS processes described in Section 2.1.3, two jets with a large rapidity gap are present due to the radiation of vector bosons from the incoming quarks, and the resulting bosons are expected to be central. To effectively suppress the dominant WZ-QCD background in this topology and enhance sensitivity to a potential VBF-produced resonance signal, an ANN-based classifier is trained using simulated signal events from the Georgi–Machacek (GM) model ($H_5^{\pm}$) and WZ-QCD events as background. The GM model is chosen for training since the input VBF kinematic variables exhibit similar distributions across both GM and HVT benchmark signals, and the performance of the ANN was found to be stable across models.

The ANN training is performed in a region enriched in VBF-like events, defined by requiring at least two jets and the leading pair to satisfy $m_{jj} > 100$ GeV. Among the input variables used are the invariant mass and azimuthal angle separation of the leading jets (m_{jj}, $\Delta\phi_{jj}$), the pseudorapidities of the W and Z bosons and of the leading jet (η_W, η_Z, η_{j1}), the event centrality (ζ_{Lep}), the missing transverse momentum (E_T^{miss}), and the scalar sum of the transverse momenta of the VBF jets and the WZ decay leptons (H_T).

All input variables were validated against data in a WZ-QCD enriched control region, showing good agreement between data and simulation. This validation confirms that the simulation accurately models the distributions and correlations of the ANN input features, enabling a reliable multivariate selection. In particular, the ANN output score itself shows excellent modeling in both the control and signal regions, as illustrated in Figure 3.4.

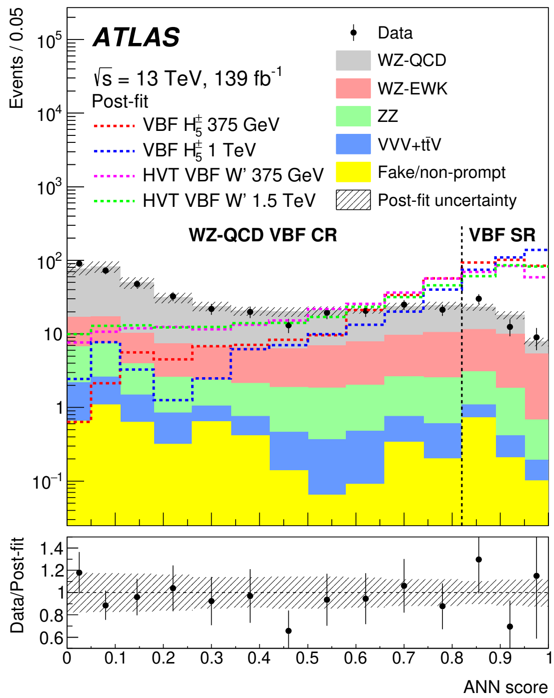

Figure 3.4: Distribution of the ANN score in the WZ-QCD VBF control region and the VBF signal region. The background predictions are obtained from a background-only simultaneous fit to the VBF signal region. The distributions for the HVT VBF model W' and GM $H_5^{\pm}$ simulations are shown normalized to the data integral. The vertical dotted line shows the threshold value for the ANN output score used to define the VBF signal region.

A fixed threshold on the ANN output score is chosen to maximize the expected significance at the lowest tested resonance mass (200 GeV), allowing for a single signal region definition across the full tested mass range. This strategy minimizes training overhead and avoids the need for separate classifiers per mass point. The same ANN is then applied to both GM and HVT signal samples. After final selections, the VBF signal region corresponds to events with $m_{jj} > 500$ GeV.

The statistical analysis was performed using a binned profile-likelihood-ratio test statistic [170], constructed from the distribution of the reconstructed $m(WZ)$ in the signal regions. I was responsible for this analysis, in close collaboration with Abhishek. The fits incorporate both the signal region and dedicated control regions for the dominant backgrounds (WZ-QCD and ZZ), and are performed separately for the Drell–Yan and VBF categories.

In the VBF fits, signal hypotheses for both W' (HVT model) and $H_5^{\pm}$ (GM model) are tested independently. The normalization of the WZ-QCD background is determined from data and is reduced by about 30% relative to the pre-fit expectation, in agreement with the SM analysis. The normalization of the ZZ background remains consistent with its pre-fit value.

The largest excess is observed in the VBF category at $m(WZ) \approx 375$ GeV, corresponding to local significances of 2.8σ for a GM $H_5^{\pm}$ boson and 2.5σ for an HVT W'. The corresponding global significances, accounting for the look-elsewhere effect up to 1.2 TeV, are 1.6σ and 1.7σ, respectively.

Figure 3.3 shows the resulting exclusion limits for the HVT model, with Model C limits being the first reported by ATLAS. These exclusions serve as a reminder that high-mass limits in the Drell-Yann production mode do not imply that all BSM scenarios are ruled out—some may simply remain out of reach in corners of the phase space that are experimentally challenging.

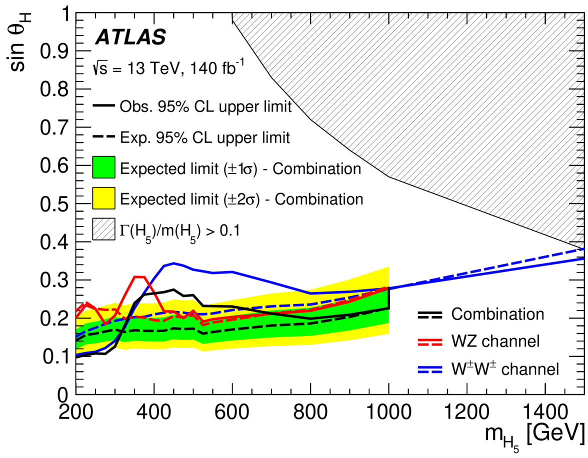

Figure 3.5: The exclusion limits for $sin(\theta_H)$ are shown as a fuction of the resonance mass, up to $m_{H_5} = 1500$ GeV. The limits on $sin(\theta_H)$ obtained separately in the $H_5^{\pm} \rightarrow W^{\pm}Z$ and $H_5^{\pm\pm} \rightarrow W^{\pm}W^{\pm}$ channels are also shown for comparison. The hatched region covers the parameter space where the intrinsic widths of the $H_5^{\pm}$ and $H_5^{\pm\pm}$ bosons would be larger than 10% of m_{H5} and is disfavoured in the GM model.Figure taken from [171]

The GM limits obtained in this analysis [167] were combined with those from the VBS same-charge $W^{\pm}W^{\pm}$ analysis [71]. Figure 3.5 displays the individual limits as well as the combination on the charged Higgs $H_5^{\pm}$ from the GM model [171]. The largest deviation from the Standard Model occurs for a resonant mass near 375 GeV, with a global significance of 2.5 standard deviations.

Despite the interesting local excess observed in the VBF topology, no significant deviation from the Standard Model expectation is found, and no new resonance is established. However, this analysis represents a significant step forward by extending resonance searches for new physics to include scenarios like the Georgi-Machacek model, which had not previously been explored in this channel. Additional results targeting semi-leptonic final states are expected to follow, with the potential to further extend the sensitivity of the search. Who knows—perhaps new physics is hiding in this less-charted corner of the phase space.

3.2 Indirect searches

There are strong theoretical reasons to believe that physics beyond the Standard Model exists. Some of these motivations, like the hierarchy problem and the existence of dark matter, suggest that new physics should emerge at the TeV scale. However, experimental data appears to indicate otherwise. The LHC has conducted thorough searches for new particles, pushing the lower bounds on the masses of most hypothetical particles studied $\gtrsim$1 TeV [172]. Additionally, precision measurements from LHC, LEP-2 [173] and constraints from flavor physics [174] suggest a scenario in which new physics lies at a higher energy scale, separated from the SM Higgs boson by a mass gap of several TeV.

In this context, the SM can be regarded as a highly successful approximation of nature—an effective theory[2] that accurately describes the phenomena observed in experimental data and remains valid up to an as-yet undetermined cutoff energy scale Λ. The goal of indirect searches for physics beyond the SM will be then to identify effects that arise at finite values of Λ but vanish in the limit $\Lambda \to \infty$. Figure 3.6 provides a schematic representation of how an observable can be affected by a hypothetical heavy particle X with mass M_X beyond the direct energy reach of the LHC. In this picture, the effects of the new resonance manifest as deviations in the high-energy tail of the distribution, even if the resonance itself cannot be directly observed at collider energies.

To systematically capture deviations in the data, a model-independent framework is essential. Historically, the κ-framework was widely used for indirect searches, particularly in studies of anomalous triple gauge couplings. This approach dates back to the LEP era and was also employed in some of the first diboson analyses at the LHC that explored indirect searches, including in my own PhD thesis. However, the κ-framework has certain limitations: it is based on coupling modifiers, which directly introduce modifications to selected couplings. While this method is intuitive and straightforward to implement, it lacks a systematic connection to a UV-complete theory and does not naturally correlate deviations across different processes [175]. As a result, the theory and experimental community today favors the Effective Field Theory (EFT) approach, which introduces higher-dimensional operators suppressed by a cutoff scale. This provides a consistent expansion that links deviations across multiple channels, allowing for a more robust and theoretically grounded interpretation of experimental results while ensuring compatibility with various beyond-the-Standard-Model scenarios.

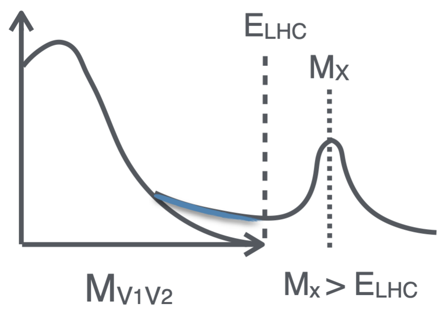

Figure 3.6: Schematic representation of how an observable can be affected by a hypothetical heavy particle X with mass M_X beyond the direct energy reach of the LHC.

In the EFT approach, all possible operators consistent with the assumed symmetries are included, each suppressed by appropriate powers of Λ, the new physics scale. If Λ is of the order of a few TeV, these higher-dimensional operators can induce measurable deviations in physics observables at the LHC. The key advantage of EFT is that it encapsulates the influence of heavy states at low energy in a model-independent manner. If an excess is observed, rather than remaining an isolated deviation in a specific analysis or single coupling, it can be attributed to a particular EFT operator. These operators naturally connect different vertices, observables, and final-state searches through a common theoretical framework, offering a unified interpretation of potential new physics effects and eventually pointing to the direction where new physics is hiding.

My current research focuses on EFT interpretations of the data, aiming to identify correlations across different channels in the hope of revealing new physics effects. The EFT framework provides a consistent and theoretically motivated approach to interpreting deviations observed in experimental results. However,

[2] An effective field theory is an approximation of an underlying physical theory that describes physical phenomena at a given energy scale by focusing on the relevant degrees of freedom. This is achieved by separating energy scales—integrating out short-distance (high-energy) effects into higher-dimensional operators constrained by symmetries. Despite neglecting unresolved microscopic details, EFTs retain predictive power for low-energy phenomena through controlled expansions in the ratio of energy scales E/Λ.

it is important to note that the κ-framework remains a practical tool and is still used at the LHC for certain interpretations, particularly when a simplified and direct modification of couplings is sufficient. In the following sections, I will introduce the EFT framework, outlining its applications in multi-boson physics and discussing the experimental results to which I have contributed in this context.

3.2.1 Effective Field Theories the Bottom-Up Approach

An Effective field theory provides a generic parameterization of an underlying theory at energy scales beyond the current experimental reach. By construction it remains valid only within a restricted energy range, but is able to encapsulate the low-energy effects of new physics that manifest at scales above the characteristic cutoff Λ.

In order to introduce new physics interactions using an effective field theory framework, some assumptions about the underlying symmetries to respect must be made, as these symmetries enforce strict constraints on the allowed higher-dimensional operators. When building an EFT extension of the SM for example, assumptions can be made regarding the mechanism of electroweak symmetry breaking. In the Standard Model Effective Field Theory (SMEFT) [175–178], the Higgs boson is explicitly included as part of an $SU(2)_L$ scalar doublet, and the gauge symmetry $SU(2)_L \otimes U(1)_Y$ is linearly realized. In contrast, the Higgs Effective Field Theory (HEFT) [175, 179] does not assume a specific doublet structure for the Higgs boson and instead allows for a more general parameterization of electroweak symmetry breaking. My research focuses on SMEFT interpretations of experimental data, where we assume a linear realization of the SM and the effective Lagrangian is expressed as:

$$\mathcal{L}_{\text{EFT}} = \mathcal{L}_{\text{SM}} + \sum_{d>4}^{\infty} \sum_{i=0}^{N_d} \frac{f_i^{(d)}}{\Lambda^{d-4}} O_i^{(d)} \tag{3.1}$$

where $\mathcal{L}_{\text{SM}}$ is the Standard Model Lagrangian, O_i are higher-dimensional operators constructed from Standard Model fields, f_i are the associated Wilson coefficients, d is the dimension of the operators, N_d the parameters to describe the interactions at each given dimension, and Λ represents the scale of new physics. The operators include combinations of Higgs doublets, gauge bosons, fermionic fields, and their covariant derivatives. In this expansion, given the factor $1/\Lambda^{d-4}$, the operators with lowest dimensions are expected to have the largest contributions at energies below the new physics scale Λ. In the limit $\Lambda \longrightarrow \infty$ this factor $1/\Lambda^{d-4}$ gets so small that the Lagrangian is composed of SM terms only.

It can also be seen from Eq. 3.1 that all operators of dimension $d > 4$ encode effects of physics beyond the Standard Model. The lowest-order BSM contribution appears at $d = 5$ (dim-5), where a unique operator generates Majorana neutrino masses[3] after electroweak symmetry breaking. At $d = 6$ (dim-6), the number of independent operators increases dramatically, with over 3000 operators contributing to a wide range of physical processes, including Higgs physics, electroweak precision measurements, flavor physics, nuclear interactions, and searches for electric dipole moments. But since my research focuses on bosonic operators, which are constructed solely from SM gauge and Higgs fields without involving fermionic degrees of freedom, we can focus on 15 operators, that at dim-6 in the Warsaw basis, impact vertices with triple

[3] The experimental evidence for neutrino masses raises the question of their fundamental nature. Two main mechanisms can generate neutrino masses: a Majorana mass term for left-handed neutrinos or the introduction of right-handed neutrinos, leading to Dirac masses. The precise nature of SM neutrino masses—whether Majorana, Dirac, or a combination of both—remains an open question.

boson couplings. Dibosons experimental analysis typically provide strong limits on Triple Gage Coupling (TGC) [180, 181]. One example of less constrained dim-6 operators will be the O_H operator, which directly modifies the Higgs potential and, in particular, affects the Higgs boson self-coupling λ_{hhh} —constraining this coupling is a current hot topic at the LHC.

A critical question emerges when considering higher-dimensional operators: Do they offer meaningful insights despite their increased suppression? While the sum in Eq. 3.1 formally extends to $d = \infty$, the number of independent terms grows drastically with operator dimension. At $d = 7$, there are approximately 1500 independent operators; at $d = 8$ (dim-8), this number jumps to around 45000; at $d = 9$, it reaches nearly 90000; and by $d = 10$, we are confronted with close to two million operators [182]. With this rapid growth practical limitations arise. From an experimental perspective, it becomes practically impossible to constrain all these operators with the available data, and from a theoretical standpoint, higher-dimensional operators are increasingly suppressed by factors of $1/\Lambda^{d-4}$, making their effects progressively smaller and harder to justify.

Nevertheless, we can do the exercise again of focusing on bosonic operators only, and dim-8 reveals intriguing possibilities. Notably, this is the first dimension where operators can affect purely quartic gauge couplings (QGCs). In many BSM scenarios, new heavy bosons can generate tree-level contributions to four-gauge boson interactions, whereas their impact on triple gauge couplings arises only at the one-loop level [179]. This distinction provides a key experimental handle to probe the electroweak symmetry-breaking sector. Specifically, comparing deviations in TGCs and QGCs can help determine whether the $SU(2)_L \otimes U(1)_Y$ gauge symmetry is realized linearly or nonlinearly in the low-energy effective field theory [179]. In the following sections, I will describe the work I have performed to constrain dim-8 operators using Vector Boson Scattering measurements.

3.2.2 Anomalous Quartic Couplings and Dimension-8 EFT Operators

As discussed in Section 2.1, vector boson scattering measurements at the LHC offer a unique sensitivity to quartic couplings at the tree level, making this channel particularly interesting in case deviations from the SM model appear generating anomalous quartic interactions.

To interpret the VBS data an EFT theoretical model that focus on quartic interaction was introduced in [178, 179] and recently extended in [183]. This model describes genuine quartic couplings, meaning quartic interactions that do not induce triple couplings. The model assumes a linear realization of the electroweak symmetry, $SU(2)_L \otimes U(1)_Y$, implying that the lowest-order pure quartic couplings arise from dim-8 operators, as described by the following effective Lagrangian:

$$\mathcal{L}_{\text{EFT}} = \mathcal{L}_{\text{SM}} + \sum_{i=0}^{N_8} \frac{f_i^{(8)}}{\Lambda^4} O_i^{(8)}, \tag{3.2}$$

The operators in this model can be classified into three categories based on their field content:

- S-type operators: Quartic in the Higgs field, these operators affect only quartic gauge boson vertices involving longitudinally polarized bosons and/or Higgs bosons.

- M-type operators: Involving both Higgs fields and gauge field strengths, these operators contribute to vertices with mixed longitudinally and transversely polarized vector bosons.
- T-type operators: Quartic in the gauge field strengths, affecting interactions between transversely polarized gauge bosons.

The full mathematical expressions for these operators can be found in [178, 183]. Tab. 3.1 summarizes all the operators included in the latest version of the model [183] and the quartic vertices they are contributing to. The bottom half of the table includes the recently introduced operators $O_{M,8}$ and $O_{M,9}$ that were mistakenly identified as CP odd in previous publications, as well as the CP-odd operators, denoted as $\not{O}_i$.

CP	Operator	Vertices												
		$WWWW$	$WWZZ$	$WW\gamma Z$	$WW\gamma\gamma$	$ZZZZ$	$ZZZ\gamma$	$ZZ\gamma\gamma$	$Z\gamma\gamma\gamma$	$\gamma\gamma\gamma\gamma$	$ZZHH$	$WWHH$	$Z\gamma HH$	$\gamma\gamma HH$
++	$O_{S,0}, O_{S,1}, O_{S,2}$	✓	✓			✓					✓	✓		
	$O_{M,0}, O_{M,1}, O_{M,7}$	✓	✓	✓	✓	✓	✓	✓			✓	✓	✓	✓
	$O_{M,2}, O_{M,3}, O_{M,4}, O_{M,5}$		✓	✓	✓	✓	✓	✓			✓		✓	✓
	$O_{T,0}, O_{T,1}, O_{T,2}$	✓	✓	✓	✓	✓	✓	✓	✓	✓				
	$O_{T,5}, O_{T,6}, O_{T,7}$		✓	✓	✓	✓	✓	✓	✓	✓				
	$O_{T,8}, O_{T,9}$					✓	✓	✓	✓	✓				
−−	$O_{M,8}$	?	?	?	?	?	?	?	?	?				
	$O_{M,9}$	?	?	?	?	?	?	?	?	?		✓		
−+ +−	$\not{O}_{M,1}, \not{O}_{M,2}, \not{O}_{M,4}, \not{O}_{M,5}$	?	?	?	?	?	?	?	?	?	✓		✓	✓
	$\not{O}_{M,3}, \not{O}_{M,6}$	?	?	?	?	?	?	?	?	?				
	$\not{O}_{T,1}, \not{O}_{T,2}, \not{O}_{T,3}$	?	?	?	?	?	?	?	?	?				
	$\not{O}_{T,4}, \not{O}_{T,5}, \not{O}_{T,6}$	?	?	?	?	?	?	?	?	?				

Table 3.1: dim-8 operators in the model [183] and the quartic vertices each operator is contributing to.

Table. 3.1 also serves to highlight the correlations; we can see that a single operator can affect multiple quartic vertices. This implies that if new physics modifies a particular operator, we should expect to observe correlated deviations across different channels sensitive to these quartic vertices. Such correlations are a powerful tool for distinguishing genuine new physics effects from statistical fluctuations or systematic uncertainties.

Preserving Unitarity

Effective Field Theories (EFTs) are rarely formulated as UV-complete theories, which means that unitarity violation[4] is an intrinsic feature unless explicitly controlled. Introducing new physics in quartic couplings messes up the delicate cancellations among triple and quartic gauge couplings, as well as the Higgs boson couplings present in the Standard Model, see Section 2.1. This imbalance leads to a growing scattering amplitude and ultimately results in unitarity violation at high energies.

In the dim-8 EFT under study, this violation occurs below the cutoff scale Λ, and the unitarity bound depends on the specific operators [184], rendering EFT predictions unreliable above a certain energy scale. To address this issue, unitarization techniques are often employed to restore unitarity and maintain the validity of the EFT. Various unitarization methods have been explored in experimental analyses, including the use of form factors and K/T-matrix approaches [185, 186]. However, different unitarization techniques have their own limitations—for instance, the K-matrix approach is not well-defined for final states involving photons.

The choice of unitarization method significantly impacts high-energy predictions and, consequently, the interpretation of experimental data. Unitarization effectively removes some of the predicted high-energy events, meaning that when comparing predictions to data, limits obtained without unitarization tend to be tighter.

During Run-1, ATLAS and CMS employed different approaches to deal with unitarity, making direct comparisons between their results challenging. For example using K-matrix approach limits on operators that affect heavy boson vertices could not be compared with those having photons involved. For Run-2, after numerous discussions a set of LHC recommendations favored the "clipping" approach [187]. In this method, EFT contributions above a chosen energy threshold are discarded, ensuring that predictions remain valid only up to that threshold, without attempting to model physics beyond the cutoff scale Λ. A key advantage of this technique is that, unlike some unitarization methods that may compromise the model independence of the EFT framework, clipping preserves this independence. Following this recommendations the experimental results can be presented for various choices of the clipping energy. This straightforward approach was adopted by both collaborations, significantly improving result comparability. The partial Run-2 VBS $W^{\pm}W^{\pm}$ analysis and the dim-8 EFT combination analysis, which I led, were the first ATLAS analyses to implement the clipping technique for unitarization. Today, this method is considered standard in VBS analyses.

Simulation of dimension-eight EFT Operators

To confront the EFT predictions with experimental data, accurate Monte Carlo (MC) simulations are crucial. Simulated collision events, help us to understand the possible effects of different EFT operators on the observables we will measure. The dim-8 EFT model [178, 179] comes with an associated set of Feynman rules [188], which can be imported into Monte Carlo event generators, allowing for detailed and reliable simulations of EFT operators.

Generating events to study the impact of individual operators, as well as their combinations, is computationally intensive. The latest model [183] incorporates approximately 31 operators, resulting in a vast

[4] Unitarity violation refers to the breakdown of the fundamental quantum mechanical principle of unitarity, which requires that the total probability of all possible outcomes of a scattering process sums to one.

number of possible combinations to explore. Moreover, the cross-section is dependent on the values of Wilson coefficients, meaning that even for a fixed set of operators, variations in these coefficients can lead to different cross-sections and altered shapes of physical distributions.

ATLAS analyses in Run-1 employed a grid-based approach for simulation samples. For one-dimensional exclusion bounds, typically 5-7 samples per operator were generated [189–191]. Two-dimensional scans required significantly more samples, ranging from around 60 in the WZ analysis [191] to over 100 for $W^{\pm}W^{\pm}$ [63, 192] per parameter pair. However, this discrete sampling approach did not provide smooth coverage for continuous predictions of SM+EFT signal cross-sections as a function of the EFT parameter values. To address this, parametrizations were obtained through fits of the EFT sample cross-sections at generator level. While this allowed for interpolation between generated points, it also required certain assumptions about detector acceptance, efficiencies and even more complicated ones to include unitarization.

An alternative method for creating BSM Monte Carlo samples, available in MadGraph, is the amplitude decomposition approach. This technique enables the separation of different contributions to the total amplitude during event generation, by producing Standard Model, interference, and BSM terms, which can later be recombined, added together. At the beginning of Run-2, the dim-8 EFT model [188] became available, allowing for the implementation of this method. In collaboration with Steffanie Todt, a Ph.D. student under my supervision, we validated the feasibility of using this approach for sample generation with this model. The primary advantage of the amplitude decomposition method is its potential to significantly reduce the number of samples required to scan a wide parameter space.

For the dim-8 EFT samples, the total amplitude of the process can be decomposed as the sum of the Standard Model component and the contributions from EFT operators:

$$\underbrace{\left|\mathcal{M}_{\mathrm{SM}} + \sum_i \frac{f_i}{\Lambda^4}\mathcal{M}_i\right|^2}_{\textbf{Full}} = \underbrace{|\mathcal{M}_{\mathrm{SM}}|^2}_{\textbf{SM}} + \underbrace{\sum_i 2\frac{f_i}{\Lambda^4}\Re(\mathcal{M}_i^*\mathcal{M}_{\mathrm{SM}})}_{\textbf{Linear}} + \underbrace{\sum_i \frac{f_i^2}{\Lambda^8}|\mathcal{M}_i|^2}_{\textbf{Quadratic}} + \underbrace{\sum_{i,j;i\neq j} 2\frac{f_i f_j}{\Lambda^8}\Re(\mathcal{M}_i^*\mathcal{M}_j)}_{\textbf{Cross}} \quad (3.3)$$

Here, $\mathcal{M}_{\mathrm{SM}}$ represents the SM amplitude, while $\mathcal{M}_i$ corresponds to the EFT amplitude associated with operator O_i. The terms in this expansion can be interpreted as follows:

- The pure SM contribution: $|\mathcal{M}_{\mathrm{SM}}|^2$.
- The interference term between the SM and EFT operator i, referred to as the linear term: $2\frac{f_i}{\Lambda^4}\Re(\mathcal{M}_i^*\mathcal{M}_{\mathrm{SM}})$.
- The pure EFT contribution, referred to as the quadratic term: $\frac{f_i^2}{\Lambda^8}|\mathcal{M}_i|^2$.
- The interference between two different EFT operators i and j, referred to as the cross term: $2\frac{f_i f_j}{\Lambda^8}\Re(\mathcal{M}_i^*\mathcal{M}_j)$.

The Eq. 3.3 also shows that each Beyond Standard Model contribution is scaled by a coefficient proportional to $\frac{f_i}{\Lambda^4}$. By generating individual Monte Carlo samples for the Linear, Quadratic, and, in two-dimensional cases, the Cross-term contributions, these components can be combined with a SM sample to reconstruct arbitrary points in one- or two-dimensional parameter spaces for any observable. This is achieved using the following formula:

$$\mathbf{Full}(x = \frac{f_i}{\Lambda^4}, y = \frac{f_j}{\Lambda^4}) = \mathbf{SM} + \frac{x}{x_n}\mathbf{Linear}(x_n) + \frac{x^2}{x_n^2}\mathbf{Quadratic}(x_n) + \frac{y}{y_n}\mathbf{Linear}(y_n) + \frac{y^2}{y_n^2}\mathbf{Quadratic}(y_n) + \frac{xy}{x_n y_n}\mathbf{Cross}(x_n, y_n), \quad (3.4)$$

In this formula, x and y represent the coefficients $\frac{f_i}{\Lambda^4}$ for which we want to evaluate the EFT effects, while x_n and y_n are the coefficients used in the original simulation. The resulting Full sample is an event sample that describes the complete effect of the SM with EFT extensions. Its differential kinematic distributions predict the full effect as predicted by the theory.

This approach allows for efficient exploration of the EFT parameter space without the need to generate a new sample for each point of interest. By appropriately scaling and combining the precomputed contributions, we can reconstruct the full amplitude for any desired set of Wilson coefficients- just two samples per operator are needed for one-dimensional limits and five for a complete two-dimensional scan.

The advantages of the amplitude decomposition approach are clear. However, validating this method proved to be a non-trivial and technically challenging task. It required generating multiple sets of samples using the amplitude decomposition, which were then compared with a Full (SM+EFT) simulation for numerous operators and coefficient values. In theory, if the amplitude decomposition approach works correctly for this model, agreement should be within statistical uncertainties. However, sizable discrepancies appeared, particularly for the VBS $W^{\pm}W^{\pm}$ process. These discrepancies were evident not only in the cross-section but also in the shape of physics observables. Figure 3.7(a) illustrates this issue, showing the invariant mass of the $W^{\pm}W^{\pm}$ system at generator level, obtained from both the sum of the amplitudes and a full sample. The discrepancies are significant, exceeding 50% at high m_{WW} values.

The investigation of this discrepancy became an important topic of Stefanie's thesis. We explored various potential issues, including the interference definition, the possible effects of the scale used, and the model itself. All details of these studies are documented in [60]. The key to understanding the source of the discrepancy is illustrated in Figure 3.7(b). We discovered that the Full predictions suffer from deficiencies in the phase space integration of the MC sample simulation. In the Full prediction, the SM contribution dominates, which is large at low energies. Consequently, the MC integration is automatically optimized for this region, neglecting the region where EFT contributions become relevant. This issue is expected to affect all final states, with the extent depending on their energy reach.

Based on these findings, a set of recommendations for validating dim-8 samples was developed and made available to ATLAS analyses through a twiki page [193]. What is recommended is basically to avoid further use of the Full prediction and instead produce the simulation with the amplitude decomposition method. An alternative strategy could involve slicing the Full predictions into multiple samples based on energy or mass variables, this could avoid the integration issues, but will be significantly more resource-intensive.

In the following sections we used the method of amplitude decomposition together with the model [188] this allows for a reduction in the number of fully simulated samples needed for EFT limits. The samples cover the full phase space without requiring interpolations and provide accurate predictions, as they do not suffer from phase space integration issues. The amplitude decomposition approach is the standard in ATLAS for dim-8 EFT interpretations.

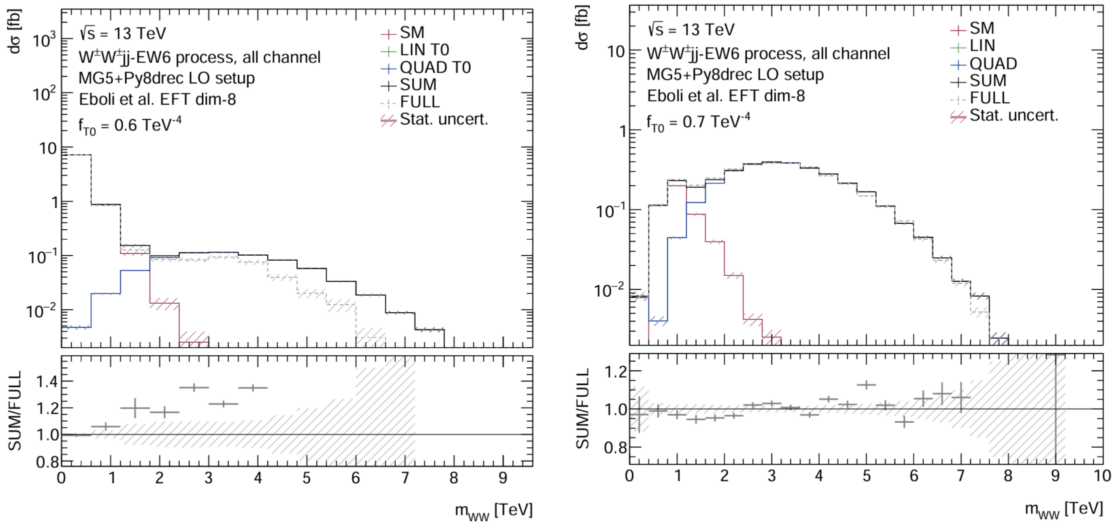

(a) (b)

Figure 3.7: Distributions of the invariant mass of the $W^{\pm}W^{\pm}$ system, m_{WW}. (a) in an inclusive generator phase space; (b) in a restricted generator phase space with a minimum requirement on the dilepton mass, m_{ll}, of 500 GeV for the f_{T0}/Λ^4 parameter. The lines in the figure show the SM prediction, the decomposed Linear (LIN) and Quadratic (QUAD) EFT contributions and their sum, labelled SUM, together with the prediction of an independently simulated sample of the full prediction of the SM with the EFT extension, labelled FULL, are shown. Figures taken from Ref. [60].

3.2.3 Current Status of EFT Interpretations at the LHC

Effective Field Theories have proven to be powerful tools for describing physics beyond experimentally accessible energy scales. The Fermi effective theory of the weak interaction played a crucial role in identifying the structure of the electroweak sector of the Standard Model, just as the chiral effective Lagrangian helped establish QCD as the theory of strong interactions. Naturally, EFT interpretations have always been part of the ATLAS and CMS physics programs at the LHC. The first constraints from Run-1 data built upon earlier measurements of anomalous triple gauge couplings at LEP. While LEP focused on interpreting triple gauge couplings within the k-framework, LHC data opens the door to a broader exploration of anomalous quartic gauge couplings and dimension-8 EFT effects, given the larger energy reach and statistics.

Today, numerous results cover different high-energy runs of the LHC, with analyses spanning over a variety of final states. These include VBS and triboson measurements, where massive bosons decay into leptons, jets, and photons. A summary of the latest ATLAS and CMS results, including exclusion limits on quartic couplings and dim-8 parameters, is presented in the Table 3.2. While some results might have escaped my radar, the table is already large enough to illustrate some key points. First, many channels, final states, can be analyzed with sensitivity to quartic couplings. Second, ATLAS and CMS initially adopted significantly different measurement strategies for the Run-1 results. These differences appear in the choice of formalism for data interpretation, which determines the tested parameters [194], as well as in the handling of unitarity—making it nearly impossible to compare results on equal footing.

Channel	Final state(s)	Experiment	$\sqrt{s}$ [TeV]	Luminosity [fb^{-1}]	Fit	Probed parameters α_i or f_i/Λ^4 α_i	S_i	M_i	T_i	Parameter formalism	Unitarisation method	dim-6	Ref.
$W^\pm W^\pm jj$ and $W^\pm Zjj$	fully leptonic	ATLAS	13	36	2D	×	0-2	0-1,7	0-2	MG5_AMC	-/clipping	×	[195]
$W^\pm W^\pm jj$	$\ell^\pm \nu_\ell \ell'^\pm \nu_{\ell'} jj$	ATLAS	13	139	2D	×	0-2	0-1,7	0-2	MG5_AMC	-/clipping	×	[71]
$W^\pm Zjj$	$\ell^\pm \ell'^\mp \ell'^\pm \nu_{\ell'} jj$	ATLAS	13	140	1D	×	0-2	0-1,7	0-2	MG5_AMC	-/clipping	×	[72]
$W^\pm Vjj$	$\ell^\pm \nu_\ell (\ell'^\pm \nu_{\ell'} / \ell'^\pm \ell'^\mp) jj$	CMS	13	137	1D	×	0-1	0-1,7	0-2	MG5_AMC	-/clipping	×	[196]
$W^\pm W^\pm jj$	$\ell^\pm \nu_\ell \tau^\pm \nu_\tau jj$	CMS	13	138	2D	×	0-2	0-1,7	0-2	MG5_AMC	-/clipping	incl	[197]
$(W^\pm V + ZV)jj$	$\ell^\pm \nu_\ell (\ell^\pm \ell'^\mp) jjjj$	CMS	13	138	1D	×	0-2	0-7	0-9	MG5_AMC	-/clipping	×	[198]
$ZZjj$	$\ell^\pm \ell'^\mp \ell'^\pm \ell'^\mp jj$	ATLAS	13	140	1D	×	×	×	0-2,5-9	MG5_AMC	-	×	[199]
$ZZjj$	$\ell^\pm \ell'^\mp \ell'^\pm \ell'^\mp jj$	CMS	13	137	1D	×	×	×	0-2,8-9	MG5_AMC	-	×	[200]
$VVjj$	$(\ell^\pm \nu_\ell / \ell^\pm \ell'^\mp) jj$	CMS	13	35.9	1D	×	0-1	0-1,7	0-2	MG5_AMC	-	×	[201]
$W^\pm \gamma jj$	$\ell^\pm \nu_\ell \gamma jj$	ATLAS	13	140	1D	×	×	0-7	0-7	MG5_AMC	-/clipping	×	[202]
$W^\pm \gamma jj$	$\ell^\pm \nu_\ell \gamma jj$	CMS	13	138	1D	×	×	0-7	0-3,5-7	MG5_AMC	-	×	[203]
$Z\gamma jj$	$\ell^\pm \ell'^\mp \gamma jj$	CMS	13	137	1D	×	×	all	0-7	MG5_AMC	-	×	[192]
$Z\gamma jj$	$\nu\bar{\nu}\gamma jj$	ATLAS	13	139	1D	×	×	0-2	0,5,8-9	MG5_AMC	–/clipping	×	[192]
$W^\pm W^\pm W^\pm$	$\ell^\pm \nu_\ell \ell'^\pm \nu_{\ell'} (\ell''^\pm \nu_{\ell''} / jj)$	CMS	13	35.9	1D	×	×	×	0-2	MG5_AMC	-	×	[204]
VVZ	fully-lep & semi-lep	ATLAS	13	140	1D	×	×	2-5	×	MG5_AMC	-/clipping	×	[205]
$W^\pm \gamma\gamma$	$\ell^\pm \nu_\ell \gamma\gamma$	CMS	13	137	1D	×	×	2-3	0-3,5-7	MG5_AMC	-	×	[206]
$Z\gamma\gamma$	$\ell^\pm \ell'^\mp \gamma\gamma$	CMS	13	137	1D	×	×	×	all	MG5_AMC	-	×	[206]
$W^\pm W^\pm jj$	$\ell^\pm \nu_\ell \ell'^\pm \nu_{\ell'} jj$	ATLAS	8	20.3	2D	4-5	×	×	×	WHIZARD	K-matrix	×	[63]
$W^\pm Zjj$	$\ell^\pm \ell'^\mp \ell'^\pm \nu_{\ell'} jj$	ATLAS	8	20.3	2D	4-5	×	×	×	WHIZARD	K-matrix	×	[62]
$W^\pm Vjj$	$\ell^\pm \nu_\ell (jj/J) jj$	ATLAS	8	20.2	2D	4-5	×	×	×	WHIZARD	K-matrix	×	[207]
$Z\gamma jj$	$(\ell^\pm \ell'^\mp / \nu_\ell \bar{\nu}_\ell) \gamma jj$	ATLAS	8	20.2	1D	×	×	0-3	0,8-9	MG5_AMC	-/form factor	×	[65]
$W^\pm V\gamma$	$e^\pm \nu_e \nu_\mu, \ell^\pm \nu_\ell jj\gamma$	ATLAS	8	20.2	1D	×	×	all	0-3,5-7	VBFNLO	-/form factor	×	[208]
$W^\pm V\gamma$	$\ell^\pm \nu_\ell jj\gamma$	CMS	8	19.3	1D	×	×	0-3	0	MG5_AMC	-	×	[209]
$W^\pm \gamma\gamma$	$\ell^\pm \nu_\ell \gamma\gamma$	ATLAS	8	20.3	1D	×	×	2-3	0	VBFNLO	-/form factor	×	[190]
$Z\gamma\gamma$	$(\ell^\pm \ell'^\mp / \nu_\ell \bar{\nu}_\ell) \gamma\gamma$	ATLAS	8	20.3	1D	×	×	2-3	0,5,9	VBFNLO	-/form factor	×	[189]

Table 3.2: Overview of VBS and triple boson measurements from the ATLAS and CMS experiments, presenting exclusion limits on aQGCs or dim-8 EFT parameters. The results are shown for centre-of-mass energies of 8 TeV (bottom half) and 13 TeV (top half) in final states involving leptons, jets, and/or photons, where $V = W^\pm, Z$. Only the most recent publication per experiment for each specific channel is included. The probed parameters are indicated by their indices, while "×" signifies that no measurement for this parameter group has been published. The column specifying the parameter formalism refers to different definitions implemented in the simulation programs, as summarized in Ref. [194]. Published results include both cases with and without unitarization; the latter is denoted by "-", while specific unitarization procedures are explicitly stated. The "dim-6" column indicates whether dim-6 effects were considered in the limit extraction, with "×" denoting their absence.

In the first set of results at $sqrts = 8$ TeV, ATLAS analyses followed two distinct strategies depending on the multiboson channels. Channels with only heavy bosons used the α_4 and α_5 parameters and applied the K-matrix unitarization procedure, implemented within WHIZARD. Meanwhile, analyses with photons in the final state—whether in VBS or triboson production—employed the dim-8 model and presented results both with and without form factor unitarization. This differences are due, in part, because K-matrix unitarization is not defined for final states with photons in general. Even within photon-inclusive channels, two different formalisms were used: one implemented in MG5_aMC and the other in VBFNLO. While the results of some of these approaches can be converted in order to be compared, it is fair to say the Run-1 served as a testing ground for models and unitarization methods.

At the beginning of Run-2, a concerted effort was made to harmonize the ATLAS interpretation of dim-8 EFT analyses. As convener of the electroweak group, I strongly supported the modeling studies and validations needed for this transition, some of which have already been discussed in the previous section. All 13 TeV results systematically adopted the dim-8 model [178, 179], with exclusion limits presented both with and without clipping for unitarization, ensuring direct comparisons across channels and experiments. The top part of Tab. 3.2 clearly illustrates how recent results are now well aligned in terms of both model choice and unitarization procedure.

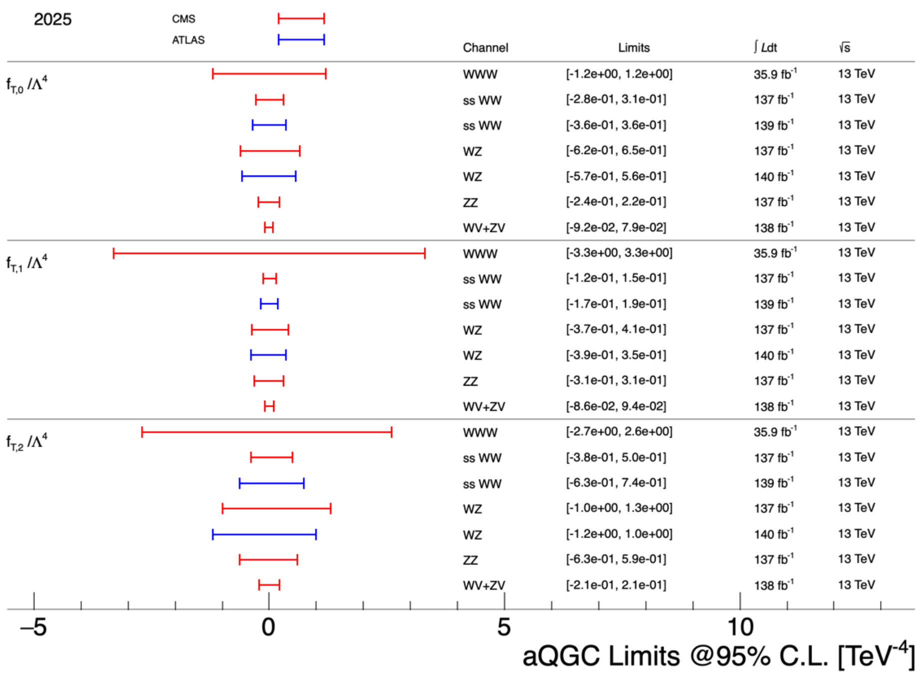

Figure 3.8: Observed 95% confidence level (CL) intervals for the dim-8 T-type operators, derived from individual channels analyzed by the ATLAS and CMS collaborations. These limits are presented without applying unitarization cut-offs.

With this unified strategy, we can now directly compare the one-dimensional observed 95% CL intervals obtained by the ATLAS and CMS collaborations. Figures Figs. 3.8 and 3.9 provide a comparative view of the three types of operators without applying a unitarization cut-off for some selected channels. The sensitivity of different channels to dim-8 EFT operators varies significantly. Channels involving hadronic decays of bosons, such as semi-leptonic processes—particularly the $W(V)/Z(V)$ channels—demonstrate a clear advantage. These benefit from larger branching fractions and access to higher energy regimes due to the inclusion of merged hadronic decays, enhancing their sensitivity. In contrast, fully leptonic final states like the same sign $W^{\pm}W^{\pm}$ and $W^{\pm}Z$ included on the figure, offer cleaner experimental signatures, making them better suited for precision measurements of Standard Model observables. However, their limited energy reach reduces their sensitivity to new physics effects compared to semi-leptonic channels. Nonetheless, probing a diverse set of final states is important to understand the coupling structure of any potential new physics.

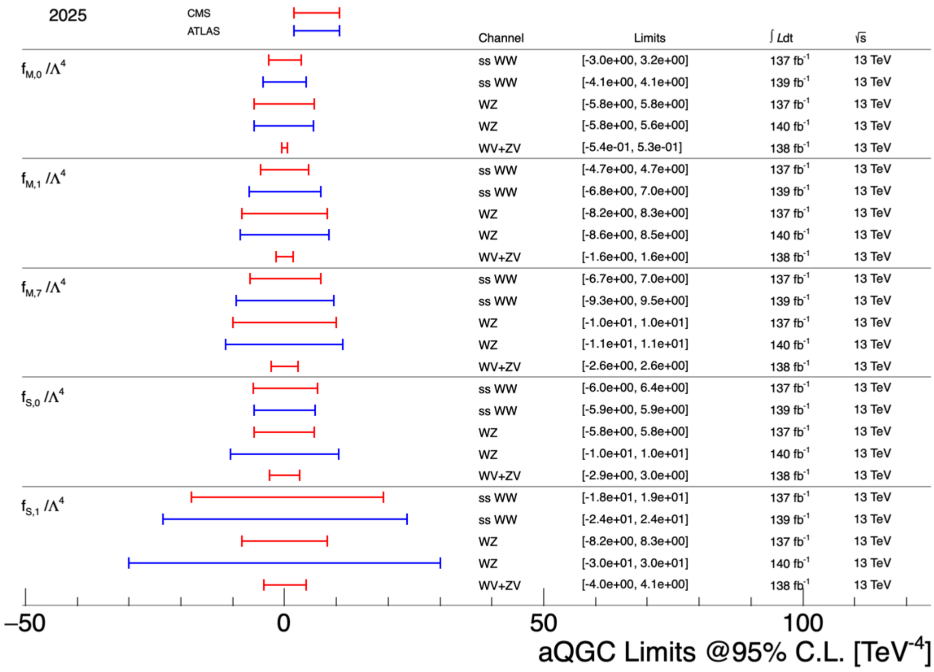

Figure 3.9: Observed 95% confidence level (CL) intervals for the dim-8 M and S-type operators, derived from individual channels analyzed by the ATLAS and CMS collaborations. These limits are presented without applying unitarization cut-offs.

The treatment of dim-6 effects is another key assumption in EFT interpretations, particularly when setting limits on dim-8 operators. The usual argument is that dim-6 operators are better constrained in inclusive diboson measurements, justifying the omission of anomalous triple gauge couplings when extracting limits on quartic interactions. This simplification is applied in nearly all experimental results, with the exception of one recent analysis [197]. However, this assumption has implications for both the reliability of the EFT expansion and the model independence often associated with these interpretations. Even if UV-complete models exist where new physics effects arise exclusively at dim-8, ignoring dim-6 contributions introduces implicit biases about the class of theories being tested. The theory community has been actively investigating the validity of this assumption. Recent studies [210, 211] suggest that the sensitivity of VBS analyses to dim-6 operators may not be negligible, as these effects can contribute not only to the signal but also to non-VBS backgrounds, which can be sizable. Their recommendation is to quantify how current bounds on dim-8 operators are altered when dim-6 contributions are included. Some initial steps to address this issue have already been taken. For instance, in the preparation of the VBS $W^{\pm}W^{\pm}$ analysis, together with Stefanie an uncertainty on the WZ background was estimated using existing dim-6 samples [60]. Another approach—since there is no cross-talk between the dim-6 and dim-8 operators at this order in the EFT expansion—is to treat them as independent contributions in the data interpretation. This strategy was explored for the first time in the CMS analysis [197], which could serve as a proof of principle. Moving forward, we are likely to see a more careful treatment of dim-6 effects in future analyses.

EFT interpretations require constraining a large number of operators, but the limited statistical power of individual analyses often restricts the number of free parameters that can be fitted simultaneously. The 'Fit' column in Tab.3.2 indicates the number of free parameters in each analysis, corresponding to the number of Wilson coefficients allowed to float in the fit. As shown, most published results extract confidence intervals for at most one or two parameters at a time, with all other beyond-Standard-Model parameters set to zero. While this approach simplifies the statistical analysis, it also reduces model independence by probing only specific scenarios and failing to capture potential correlations between different operators. While comparing results from different channels, as in Fig. Figs. 3.8 and 3.9, provides valuable insights, a more effective way to overcome statistical limitations is to combine multiple channels and final states. Tab.3.1 shows that the same operator affects multiple vertices, suggesting that a global fit across multiple channels datasets could allow more parameters to float simultaneously. As a first step toward such a combination, we performed a proof-of-concept study: the first dim-8 EFT combination in ATLAS using the VBS $W^{\pm}W^{\pm}$ and $W^{\pm}Z$ analyses [195]. This work, carried out together with Despoina, a PhD student from Thessaloniki, will be discussed in the following section.

With EFT data analysis strategies now harmonized—thanks to a consistent choice of models and unitarization schemes—we are well-positioned to move toward a combination of results. This will enhance both the robustness and model independence of our interpretations. To fully exploit the available data, it is crucial to extend EFT interpretations beyond current analyses by incorporating hadronic and boosted channels, which will provide access to higher energy regimes. Higgs-associated channels are also particularly promising, as they offer a unique window into quartic gauge-Higgs interactions—an aspect that has yet to be explored in EFT interpretations. As we refine our methods and broaden the scope of EFT studies, expanding the range of analyzed final states and performing combined interpretations will be key to exploit the full potential of the data.

Combined Effective Field Theory Interpretation of $W^{\pm}W^{\pm}jj$ and $W^{\pm}Zjj$ analyses

The results presented in this section represent the first combination effort for dim-8 operators in ATLAS. As described in the previous section, the initial focus has been on harmonizing the strategy to enable a meaningful comparison of results across different channels. Even before performing a combination, comparing independent analyses sensitive to the same operators provides valuable insights. For instance, if an excess is consistently observed across multiple channels, this could indicate that new physics is affecting a specific operator. However, in the absence of significant deviations, the most effective way to maximize sensitivity to dim-8 operators is through a combined analysis. This approach not only benefits from increased statistics but also exploits correlations between observables as predicted by the effective field theory framework, ultimately leading to more precise and robust constraints.

To lay the groundwork for a broader combination, I initiated the first dim-8 EFT combination in ATLAS in collaboration with two PhD students, Despoina and Stefanie. This effort was conceived as a proof of concept, specifically introducing the dim-8 EFT interpretation to the $W^{\pm}W^{\pm}jj$ and $W^{\pm}Zjj$ analyses based on the partial Run-2 dataset of 36 fb^{-1} [5, 7]. The two publications we used as a starting point [5, 7] reported the first observations of electroweak-induced diboson production in their respective channels—an achievement made particularly challenging by the small cross sections. Consequently, the primary focus of these studies was not on EFT interpretations, and such analyses were not included in the original publications. Our reinterpretation effort was therefore conducted post-publication, taking the analyses as they were, without additional optimizations. The goal was to assess their sensitivity to dim-8 EFT effects and establish a foundation for future, more comprehensive EFT studies.

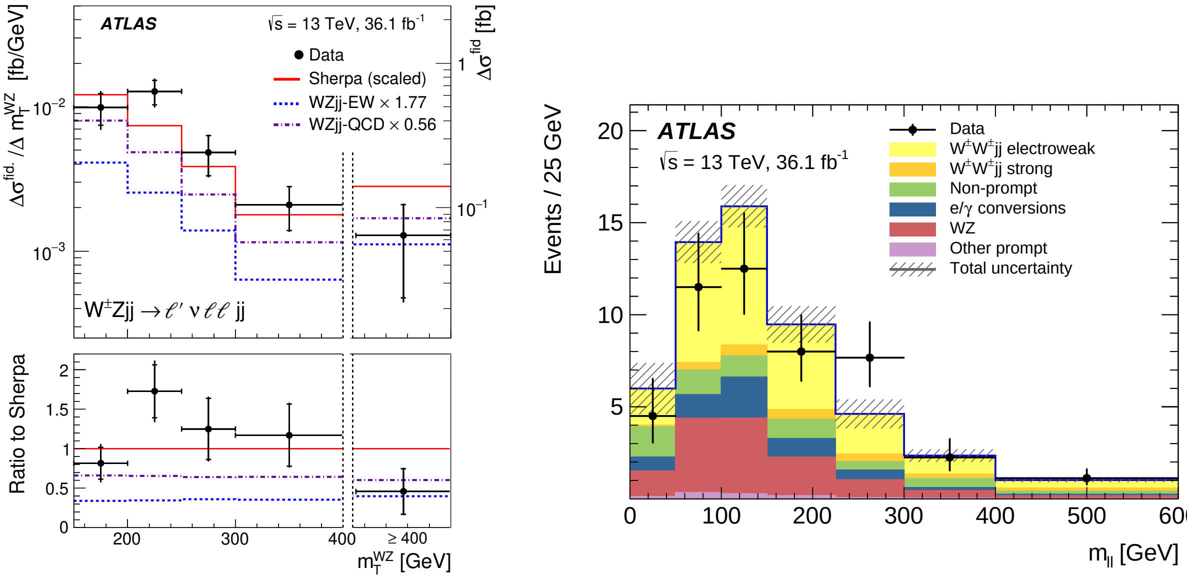

(a)

(b)

Figure 3.10: Input distributions for the combination. (a) The differential fiducial cross-section of the sum of electroweak and QCD-mediated $W^{\pm}Zjj$ production as a function of the transverse mass of the $W^{\pm}Z$ system [5]. (b) The dilepton invariant mass ($m_{\ell\ell}$) distribution at the reconstruction level after the fit for the $W^{\pm}W^{\pm}jj$ analysis [7].

The data inputs for this reinterpretation were taken directly from the published results of the $W^{\pm}Zjj$[5] and $W^{\pm}W^{\pm}jj$[7] analyses. This means that we did not modify the published analyses, not even the binning of the distributions for EFT sensitivity, nor did we use any non-public information—only results that had been officially approved by the ATLAS collaboration. Given these constraints, and considering that dim-8 EFT operators typically induce deviations in the high-energy tails of distributions, we selected two key observables, one per analysis: for $W^{\pm}W^{\pm}jj$, the dilepton invariant mass ($m_{\ell\ell}$) distribution at the reconstruction level after the fit; and for $W^{\pm}Zjj$, the differential fiducial cross-section of the sum of electroweak and QCD-mediated production as a function of the transverse mass of the $W^{\pm}Z$ system (m_T^{WZ}). The input distributions are shown side by side in Fig. 3.10. A first challenge in this combination is already visible: we are dealing with heterogeneous data formats, as one distribution is at the reconstructed level, while the other corresponds to an unfolded cross-section measurement.

To ensure a well-defined EFT interpretation we need to agree on the signal model to use as well as unitarization strategy. The signal generation, already discussed in Sec. 3.2.2, was carefully validated to ensure a consistent simulation of dim-8 operators across different channels. Since our goal was to harmonize the results in view of a larger combination, we carried out an in-depth validation of the amplitude decomposition method in both channels. For this analysis, the $W^{\pm}W^{\pm}jj$ the truth level signal simulation had to be folded to detector level to fit the data, while for the $W^{\pm}Zjj$ channel the simulations in the fiducial phase space could directly be compared with the unfolded data. For unitarization, we opted for the clipping method described earlier. The concept of clipping is straightforward: we introduce a cut for the EFT predictions when they exceed a maximal scale, M_{cut}. Since we are dealing with a VBS process, the energy of interest is not the LHC collision energy but rather the energy of the colliding bosons. We therefore

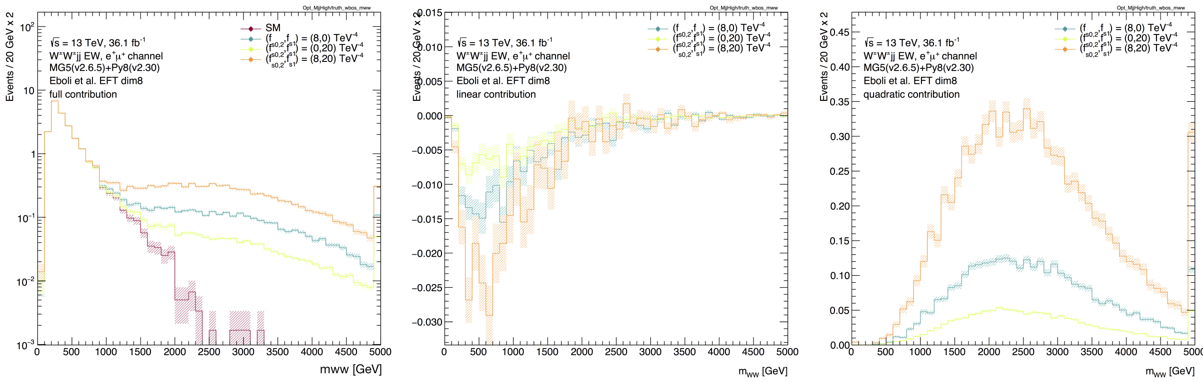

Figure 3.11: Distributions of the truth level m_{WW} for the f_{Si} parameters, the FULL sample including SM+EFT terms on the left, for the interference (INT) in the middle and the quadratic term on the right. Figure taken from [60].

applied the clipping on the invariant mass of the VV-system. Given that the aim is to restore unitary the m_{VV} used is not the reconstructed mass but the parton-level value[5]. Figure 3.11 shows the truth-level m_{WW} distributions for the f_{Si} parameters, on which clipping will be applied. The tested clipping energies for our results are M_{cut} = 500, 1000, 1500, 2000, 4000 GeV and no cut-off.

The choice of M_{cut} directly affects the balance between quadratic and interference contributions in our signal. By looking at the distributions in Fig. 3.11, we can see that lower M_{cut} values suppress quadratic terms more aggressively, which can enhance the role of interference effects. By scanning different M_{cut} values, we can assess how the limits for each operator behave, as the interplay between quadratic and interference terms shifts depending on the final state and the kinematic distributions fitted.

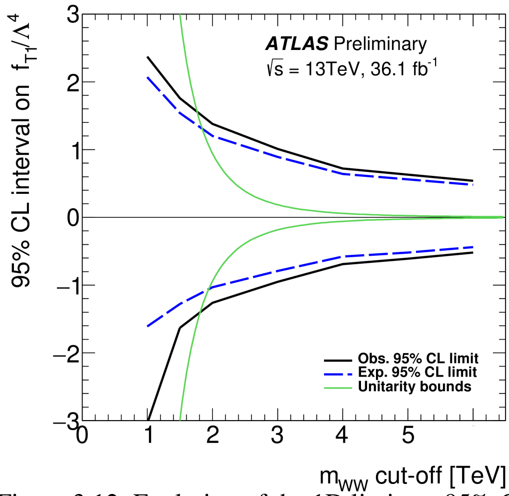

Figure 3.12: Evolution of the 1D limits at 95% CL extracted in the $W^\pm W^\pm jj$ channel as a function of the cut-off scale. Published in Ref. [195].

Fig. 3.12 shows the one-dimensional limits as a function of M_{cut} values tested for the $W^\pm W^\pm jj$ analysis. As expected, the limits degrade as the clipping value decreases. The figure also shows the unitarity bounds as predicted in Ref. [184]. The area inside the green lines corresponds to the region where EFT predictions respect unitary. The unitarity bounds are very tight in this case since they were calculated considering only one operator contribution; they become looser if more than one parameter is used.

Ensuring orthogonality between analyses is an important step in any combination to prevent double counting of events. In this case, orthogonality was straightforward in the signal regions, as the $W^\pm W^\pm jj$ analysis required exactly two leptons, while the $W^\pm Zjj$ analysis required exactly three. However, challenges arose in the control regions, where, for example, the dominant background in $W^\pm W^\pm jj$ is $W^\pm Zjj$-QCD induced production. To constrain this background, the $W^\pm W^\pm jj$ analysis included a control region with three

[5] For the m_{WW}, we select the $W^\pm$ bosons at parton level (i.e., before showering) with `PDG-ID` = 24, `status` = 22 or 23, and `barcode` < 200,000.

leptons, leading to a potential overlap with the $W^{\pm}Zjj$ signal region. Since for this combination we use postfit and unfolded distributions as inputs, it was not possible to correlate the $W^{\pm}Zjj$-QCD normalization in the fit, and therefore the $W^{\pm}Zjj$-QCD was taken as estimated in the SM analyses. This represents a limitation of the reinterpretation, mainly due to the fact that we are dealing with heterogeneous data. It is an issue that could be addressed at the analysis design stage, as demonstrated in the CMS analysis in Ref. [196], where the analysis was designed for the combination, sharing control regions, and background estimation methods.

Correlating uncertainties is another key challenge in combinations. In this case, experimental uncertainties on the object reconstruction had a small impact on both analyses and were not reported in a consistent way. One analysis had more details while the other grouped many uncertainties together in the presentation of the results. Nevertheless different correlation schemes were tested with the available information, and given their small impact if they were correlated or not, they were finally taken as uncorrelated. One of the largest experimental uncertainties for both analyses came from the estimation of the WZ-QCD background, but due to the differing methodologies used in each analysis, it was not possible to correlate them. The uncertainties with the largest impact on the limits were those related to the modeling of the signal, scale and shower uncertainties. Different correlation schemes were tested as well, and the most conservative approach was adopted when setting limits. Ultimately, the correlations of uncertainties remained limited due to the different way the results were presented in each analysis.

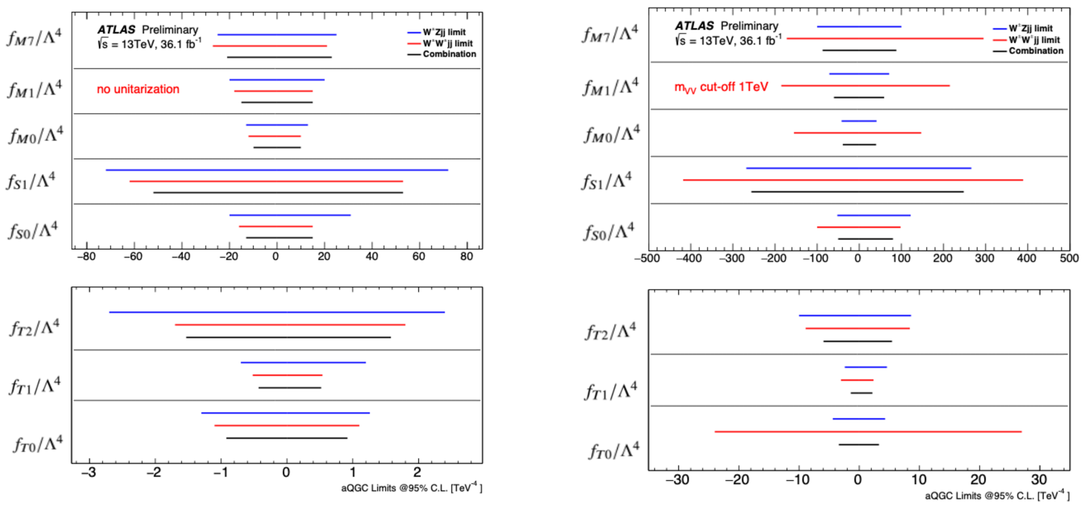

(a) (b)

Figure 3.13: One-dimensional observed 95% CL intervals on the quartic operators for the individual channels and the combination (a) without unitarization cut-off applied (b) with a cut-off at 1 TeV applied. Published in Ref. [195].

Finally, one-dimensional and two-dimensional limits are extracted. Fig. 3.13 shows the one-dimensional limits for each channel and for the combination, including both the un-unitarized limits on the left and those with a cut-off at 1 TeV. Fig. 3.14 presents examples of two-dimensional contours obtained without unitarization. The left side of the figure nicely illustrates how the two channels cover different regions of the parameter phase space.

This combination effort has demonstrated that it is possible to reinterpret data from existing analyses, highlighting the importance of performing combinations to maximize sensitivity. However, to fully exploit

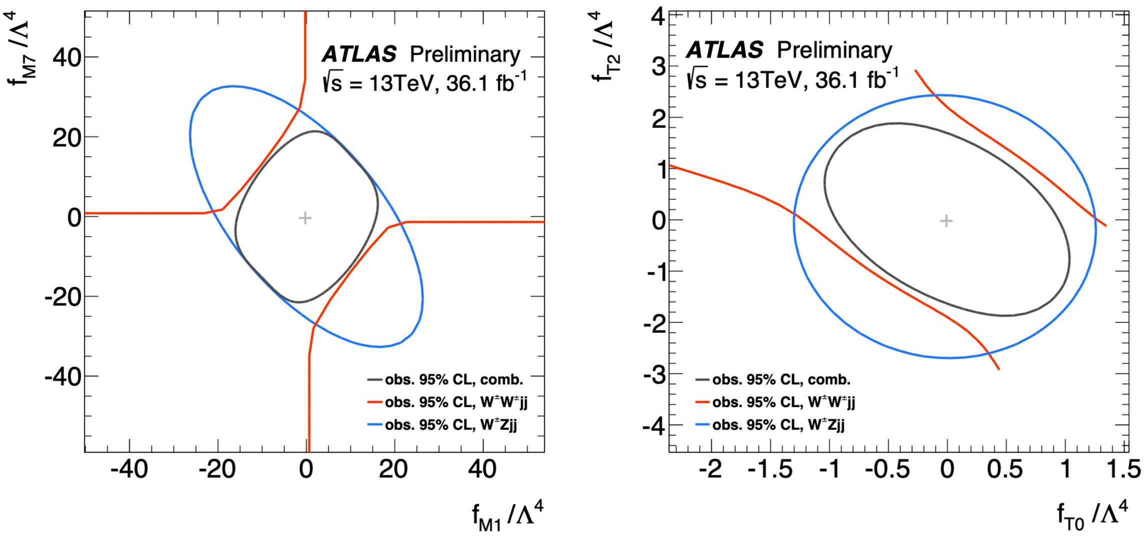

(a) (b)

Figure 3.14: Two-dimensional observed 95% CL intervals on the quartic operators (a) $f_{M1} - f_{M7}$ (b) $f_{T0} - f_{T2}$. No unitarization cut-off applied. Figures published in Ref. [195].

the available data, it is essential to provide public results in a format that allows for future reinterpretations. One of the key limitations of combining public results is the lack of flexibility in optimizing the analysis strategy. In this study, we were unable to optimize either the event selection or the binning of the fitted observable. This was particularly problematic for the WZ channel, where the last bin—expected to be the most sensitive—was too wide, effectively diluting the EFT effects with low-energy background contributions. These lessons emphasize the need for more adaptable public data releases to facilitate future reinterpretations and improve the robustness of EFT studies. A combination of the full Run-2 results building up on this first partial Run-2 publication is currently under preparation.

3.3 Summary

The search for physics beyond the Standard Model remains one of the central goals of the LHC physics program. Despite the success of the Standard Model in describing a vast array of experimental results, it leaves several fundamental questions unanswered. This motivates a wide-ranging experimental effort to probe potential deviations—whether through the discovery of new resonant particles or through indirect signs of new physics emerging at higher energy scales.

This chapter has covered two complementary strategies in this quest: direct resonance searches and indirect probes via Effective Field Theory. While direct searches aim at identifying new heavy particles as peaks or distortions in invariant mass spectra, EFT provides a model-independent framework to capture possible effects of new physics that lies beyond the current energy reach of the LHC.

In recent years, direct searches have pushed exclusion limits for many hypothetical particles well above the TeV scale. Yet, the absence of a discovery does not mean new physics is not there—it may simply reside in less accessible corners of the phase space, or in signatures we have not yet fully explored. This is why analyses targeting specific production mechanisms, such as vector boson fusion, continue to be valuable: they provide enhanced sensitivity in scenarios where new particles couple preferentially to electroweak bosons and may escape detection in more inclusive searches.

EFT-based analyses, on the other hand, enable us to constrain or reveal the presence of higher-dimensional operators that would subtly modify Standard Model predictions. These indirect effects are especially important if new physics lies at scales just beyond our experimental reach.

Throughout these efforts, I have had the opportunity to contribute to and lead both the resonance search group and the Standard Model electroweak group within ATLAS. This dual perspective has made the complementarity between these approaches and the interplay of their analysis techniques all the more evident. Each strategy informs and reinforces the other, providing a more complete picture of where new physics may—or may not—be hiding.

This journey has been deeply enriching, both scientifically and personally. And while we have made remarkable progress, the search is far from over. We still do not know where new physics is hiding—but we are looking, in every direction the data allows.

4 Outlook and Future Directions

At the beginning of my career as a particle physicist, I had the privilege of witnessing the discovery of the Higgs boson by the ATLAS and CMS collaborations — one of the most iconic achievements of the LHC. Yet, over the full span of LHC operations, this discovery stands as a highlight among many remarkable accomplishments in testing the Standard Model. The LHC has enabled the observation of rare processes — including those discussed in Chapter 2, such as vector boson scattering and boson polarization measurements — all in impressive agreement with increasingly refined theoretical predictions. These advances have profoundly deepened our understanding of the Standard Model and its intricate structure

Equally striking, however, is the persistent absence of evidence for physics beyond the Standard Model, despite strong theoretical motivations for new phenomena at the TeV scale, as outlined in Chapter 3. This tension sharpens longstanding questions, particularly regarding the apparent fine-tuning of the scalar sector — the so-called hierarchy problem — and continues to drive intense theoretical and experimental efforts.

Over the past decade, I've had the opportunity to contribute to measurements and searches that push the boundaries of the Standard Model and close off regions where new physics might be hiding. To look ahead, we can start by asking ourselves some of the fundamental questions that remain unanswered. Why do different particles couple so differently to the Higgs field? Why is the Higgs boson so light, despite quantum corrections that should drive its mass to higher scales? What stabilizes the electroweak vacuum? Could additional scalars be involved, possibly linked to the matter–antimatter asymmetry or to dark matter? These open questions ensure that the Higgs sector will remain at the forefront of theoretical and experimental exploration.

My future research will continue to focus on exploring the dynamics of the scalar sector. So far, my work has leveraged the deep connection between vector boson interactions and electroweak symmetry breaking — especially through studies of gauge boson interactions and longitudinally polarized bosons. These remain among the most sensitive probes of the Higgs mechanism and its possible extensions.

In the coming years, I plan to concentrate on two specific Higgs couplings that are still beyond the current experimental reach: the Higgs self-coupling, which encodes the shape of the scalar potential, and the quartic gauge–Higgs coupling. These can be probed through Higgs boson pair production and vector boson scattering processes involving a Higgs (VVh). Together, they provide complementary and powerful insights into scalar–gauge interactions and the structure of the Higgs potential.

In parallel, I will pursue indirect searches for new physics through the Effective Field Theory framework. Even if new particles are out of reach at current energies, their virtual effects may still leave subtle imprints — particularly in vector boson and Higgs interactions. By parameterizing these deviations, incorporating polarization observables, and combining multiple measurements, we can enhance our sensitivity. It's conceivable that new physics may couple preferentially to certain polarization states, leaving traces in angular distributions that have yet to be fully explored.

The data from the first two LHC runs, combined with advances in analysis techniques and theoretical modeling, have significantly sharpened our picture of the Standard Model. Yet many fundamental puzzles remain, the next phase of exploration — guided by precision, creativity, and persistence — holds the promise of new discoveries.

The following sections outline in more detail the key directions I plan to pursue and the opportunities I anticipate in this evolving field.

4.1 More data: From the LHC to the High-Luminosity LHC

All the processes I aim to study — or am currently studying — are severely limited by statistical uncertainties. The good news is that this situation is expected to improve significantly in the coming years. The LHC Run-3 is currently underway, with data being collected at a center-of-mass energy of 13.6 TeV. As of now, approximately 200 fb^{-1} of data have already been recorded and are waiting to be analyzed.

Following Run-3, the LHC program will enter its next phase: the High-Luminosity LHC (HL-LHC) [212]. During the HL-LHC, the instantaneous luminosity will increase by a factor of five with respect to the nominal LHC value, enabling the collection of a much larger data sample in a shorter amount of time. The HL-LHC is expected to begin operations around 2030, and will continue into the early 2040s. By the end of its run, it is expected to deliver a total integrated luminosity of up to 3000 fb^{-1} — about a tenfold increase over the dataset available today. This increase will be crucial for rare processes such as Higgs boson pair production and the scattering of longitudinally polarized electroweak vector bosons, where large statistics are essential to reach the observation.

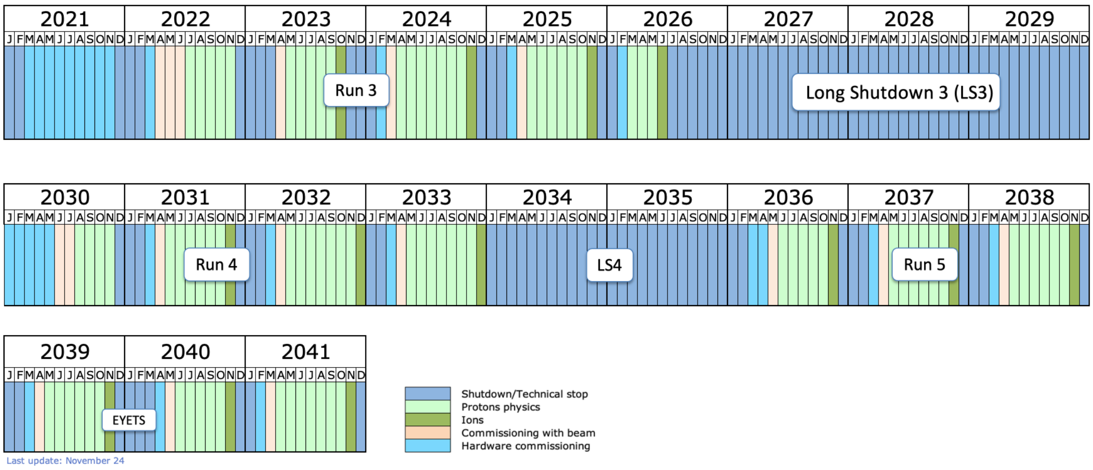

Figure 4.1: Longer-term LHC schedule, including HL-LHC exploitation. Figure taken from [213].

Operating in the high-luminosity regime comes with its own challenges. The HL-LHC will experience unprecedented levels of pileup, with up to 200 interactions per bunch crossing. To cope with this environment, the ATLAS detector will undergo a major upgrade during the Long Shutdown 3. One of the most critical components is the all-new Inner Tracker (ITk), a fully silicon-based tracking system that will replace the current inner detector.

At L2IT, one of the group's key contributions is the development and optimization of tools to fully exploit the upgraded ITk under these demanding conditions. In particular, the team is actively working on advanced tracking algorithms using graph neural networks (GNNs), which show great promise for high-performance tracking in high-pileup environments [214–216]. This is a long-term commitment for our group to ensure a good physics performance throughout the HL-LHC era.

Exploiting the LHC Run 3 and HL-LHC datasets will clearly be a priority for the next 15 years. Projection studies to assess the expected sensitivity of key analyses — such as Higgs pair production and diboson polarization measurements — will be discussed in the following sections.

Looking even further ahead, the Future Circular Collider (FCC) is being studied as a potential next-generation facility to succeed the LHC. The FCC program encompasses both a high-luminosity e^+e^- collider (FCC-ee) in its first phase, followed by a high-energy hadron collider (FCC-hh) in the same tunnel. The hadron collider would operate at a center-of-mass energy of up to 100 TeV, vastly extending the discovery potential for new physics and providing unparalleled precision in the Higgs and electroweak sectors. If realized, the FCC would offer a transformative opportunity for particle physics and could ultimately resolve some of the open questions that the LHC can only begin to explore.

4.2 Di-Higgs Projections

The study of Higgs boson pair production offers a unique window into the structure of the scalar sector of the Standard Model. It directly probes two of the least constrained interactions in the Higgs sector: the trilinear Higgs self-coupling, λ_{HHH}, and the quartic coupling between vector bosons and Higgs bosons, $VVhh$. Precise measurements of these couplings are crucial to exploring the shape of the Higgs potential and the mechanism of electroweak symmetry breaking.

Di-Higgs production proceeds via two main mechanisms: gluon-gluon fusion (ggF), which dominates in the SM, and vector boson fusion, which—while subdominant in rate—offers exceptional experimental advantages, such as better background control and direct sensitivity to the $VVhh$ vertex at tree level. The ggF mode features an interference pattern between triangle and box diagrams, making it especially sensitive to deviations in λ_{HHH}. In contrast, the VBF channel is a clean probe of the quartic gauge-Higgs coupling, with sensitivity arising from delicate cancellations between $VVhh$ and the well-measured VVh vertex. Any departure from the SM prediction in either channel could signal new physics, particularly modifications to the Higgs potential or new electroweak dynamics.

Since the Higgs boson decays almost instantly, searches rely on its decay products, with final states like $b\bar{b}\gamma\gamma$, $b\bar{b}\tau^+\tau^-$, $b\bar{b}b\bar{b}$, $b\bar{b}\ell^+\ell^- + E_T^{miss}$, among others, providing different balances of resolution, branching ratio, and background complexity. The LHC Run-2 data has already enabled a first generation of di-Higgs searches [217–222], setting upper limits on the production cross-section and the coupling modifiers $\kappa_\lambda = \lambda_{HHH}/\lambda_{HHH}^{\mathrm{SM}}$ and $\kappa_{2V} = g_{VVhh}/g_{VVhh}^{\mathrm{SM}}$. The current 95% CL intervals reach $-1.2 < \kappa_\lambda < 7.2$ and $0.6 < \kappa_{2V} < 1.5$, as shown in Figure 4.2.

Looking ahead, HL-LHC projections suggest promising sensitivity gains. Under a baseline extrapolation scenario (where statistical and some systematic uncertainties are reduced but object uncertainties are kept at Run 2 levels), a dataset of 3000 fb^{-1} at 14 TeV would lead to a discovery significance of 4.26 σ for SM-like di-Higgs production—rising to nearly 6 σ with idealized systematics (i.e no systematics at all) as illustrated in Figure 4.3. The expected precision on κ_λ and κ_{2V} would improve to $1.0^{+0.48}_{-0.42}$ and $1.0^{+0.18}_{-0.15}$, respectively.

While the observation of di-Higgs production will still require the full HL-LHC dataset, recent advances in boosted object tagging and background rejection already show that the field is preparing to reach these rare

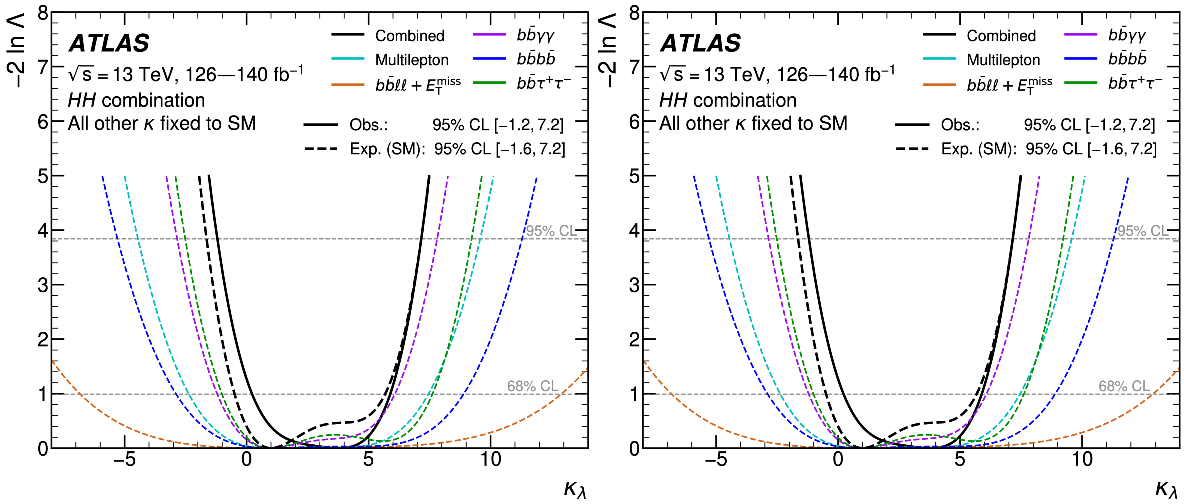

(a) (b)

Figure 4.2: Current limits on the Higgs self-coupling κ_λ and the quartic $VVhh$ coupling κ_{2V} from LHC Run-2 data. Figure taken from [223].

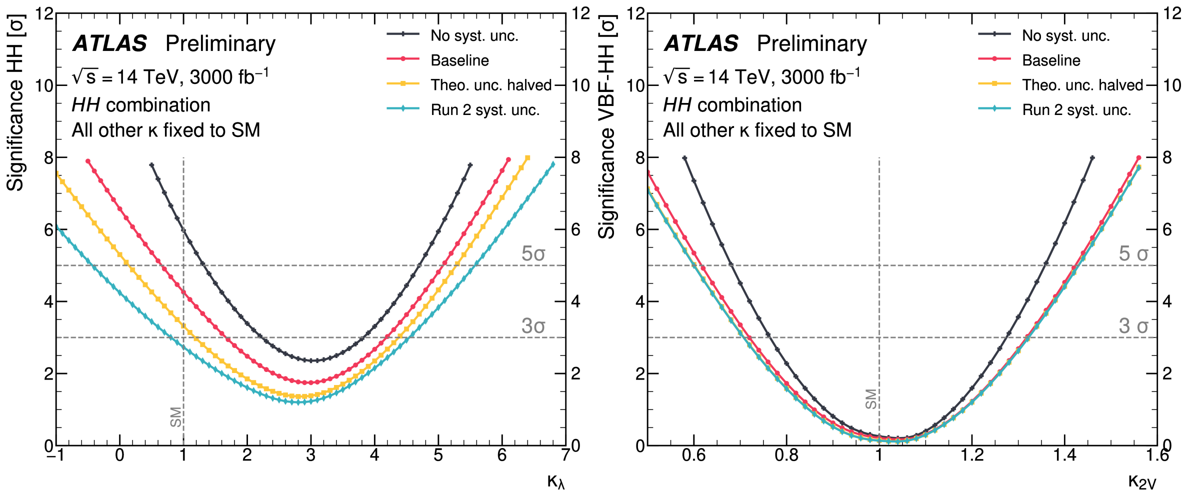

(a) (b)

Figure 4.3: Expected (a) HH and (b) VBF HH significances assuming different values of κ_λ and κ_{2V} with 3000 fb^{-1} of data at 14 TeV. The dashed horizontal lines indicate the thresholds to claim 'evidence' (3σ) and 'observation' (5σ). The dashed vertical line indicates the SM hypothesis. The sensitivity to κ_{2V} under the uncertainty scenario where theory uncertainties are halved is very similar to the uncertainty scenario where the systematic uncertainties are the same as in the Run 2 analyses, because this result is dominated by the boosted VBF $HH \to b\bar{b}b\bar{b}$ analysis, where theory uncertainties have a subdominant effect. Figure taken from [224].

signatures. Moreover, if the couplings deviate from their SM values—especially in the presence of new physics—we might uncover hints of di-Higgs production much earlier than anticipated.

In this spirit, it becomes increasingly important to interpret these measurements not only as precision SM tests but also as potential discovery channels. Most current interpretations focus on simplified coupling modifiers, κ_λ and κ_{2V}, which isolate deviations from the SM in these specific couplings. While this is a powerful first step, it removes the broader interplay with other possible new physics effects across the electroweak sector. In reality, it is difficult to modify the Higgs potential or the quartic gauge-Higgs interactions without leaving a footprint in other related processes.

One of the directions I am actively pursuing is to push these interpretations further by incorporating a more complete effective field theory framework. In particular, I have already started working on a sensitivity study of VBF di-Higgs production to dimension-8 operators, as part of the ongoing PhD thesis of Anna Tegetmeier. The preliminary results are truly encouraging and show a clear path forward to incorporate this interpretation into VBF HH results.

What's especially exciting is that certain EFT operators—such as those discussed in Chapter 3.2.3—simultaneously affect the quartic gauge couplings ($VVVV$) and the gauge-Higgs quartic couplings ($VVhh$). This creates a natural bridge between VBS and di-Higgs measurements, and the complementarity is not just powerful—it's beautiful. These operators are also polarization-aware: for instance, we already see that di-Higgs processes are not sensitive to purely transversal operators, while VBS channels excel in probing transverse polarizations. If new physics is hidding in this sector combining results from both HH and VBS may be an important step to uncovering the full structure of physics beyond the SM.

4.3 Vector Boson Scattering with a Higgs Boson (VBS VVh)

While di-Higgs production has traditionally been the primary channel for probing the Higgs boson self-coupling and quartic gauge–Higgs interactions at the LHC, a complementary process involves the vector boson scattering (VBS) production of a Higgs boson in association with two vector bosons: VBS VVh. This rare but distinctive signature provides access to both the hhh and $VVhh$ vertices in a single final state.

Figure 4.4 shows representative Feynman diagrams illustrating the sensitivity of VBS VVh to the Higgs self-coupling (κ_λ) and the quartic gauge–Higgs coupling (κ_{WW}).

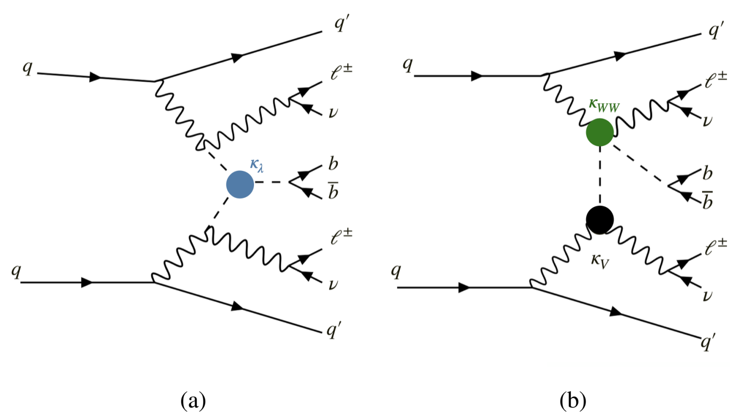

Figure 4.4: Tree-level Feynman diagrams for the vector boson scattering production of a same-sign W boson pair and a Higgs boson, showing (a) a contribution sensitive to the Higgs self-coupling (κ_λ), and (b) a contribution involving the quartic gauge–Higgs coupling (κ_{WW}).

Despite its small cross section in the Standard Model—smaller even than vector boson fusion (VBF) di-Higgs production—this process provides a unique experimental handle. Crucially, it allows independent access to both $WWhh$ and $ZZhh$ couplings, and its sensitivity to potential new physics has been emphasized in several theoretical studies [225, 226]. Notably, CMS has recently placed 95% confidence level limits on the coupling modifier κ_{WW}, demonstrating the feasibility of such an analysis [227].

New physics affecting the scalar potential or gauge–Higgs sector could lead to significant enhancements in the VVh yield, making this channel a valuable target for future LHC analyses. Its sensitivity to multiple vertices simultaneously offers an efficient probe of potential deviations from the Standard Model structure.

To quantify these effects, we adopt the κ-framework, which is commonly used in VBF di-Higgs analyses [228]. This parametrization enables independent variations of the Higgs self-coupling (κ_λ) and the quartic gauge–Higgs coupling (κ_{WW}), facilitating direct comparisons with existing results. In the longer term, this strategy will serve as a foundation for more general interpretations within the Effective Field Theory (EFT) framework, allowing for a systematic exploration of potential deviations in the scalar and gauge sectors.

Figure 4.5 shows the dependence of the VVh cross section on the coupling modifiers κ_λ and κ_{WW}. While the process displays limited sensitivity to variations in the Higgs self-coupling (κ_λ), it is highly responsive to changes in the quartic gauge–Higgs coupling (κ_{WW}).

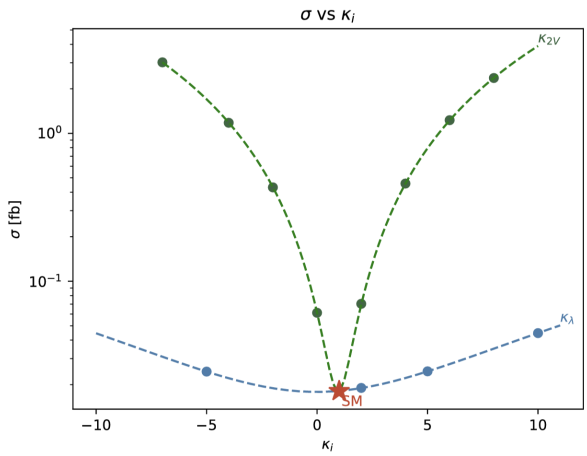

Figure 4.5: Cross section as a function of different κ values. The blue curve corresponds to modifications in κ_λ, while the green curve represents changes in κ_{WW}. Significant variations in the cross section are observed with κ_{WW} modifications, whereas κ_λ induces comparatively smaller changes in the total cross section.

The initiative to explore this process in ATLAS was originally motivated by a sensitivity study carried out during the Master's thesis of Lisa Lehmann [229], hosted in Toulouse. This early work laid the foundation for a broader research effort now underway within ATLAS, including the PhD project of Alexandro Martone and the Master thesis of Tom Allene.

Our ATLAS Run-2 analysis targets the $pp \to W^\pm W^\pm hjj$ final state, with leptonic W decays (to e or μ) and $h \to b\bar{b}$. This channel features two same-sign leptons and VBS-tagged jets, providing a clean and distinctive signature. The strategy builds on established techniques from same-sign WW measurements and aligns closely with the recent CMS approach.

This first analysis iteration will serve as proof of concept. In parallel, work is ongoing on the semi-leptonic channel, which benefits from higher statistics. Ultimately, a combined approach is expected to significantly enhance sensitivity.

As this represents a novel measurement within ATLAS, sensitivity estimates are still in progress. Nevertheless, the potential impact of this analysis at the HL-LHC makes it a timely and exciting opportunity to advance our understanding of Higgs couplings in multi-boson final states.

Looking ahead to the HL-LHC, the increased luminosity will enable exploration of additional observables, such as the angular distributions of leptons from W decays. These variables are sensitive to W boson polarization and offer a complementary probe of the $WWhh$ vertex structure and the electroweak symmetry-breaking mechanism.

4.4 More on Diboson Polarization Measurements

The study of longitudinal vector boson scattering remains a long-standing, yet elusive, milestone in high-energy physics. As discussed in Chapter 2, the scattering amplitude of longitudinally polarized vector bosons grows with the center-of-mass energy in the absence of a Higgs boson, eventually leading to a violation of unitarity. Probing this behavior experimentally means exploring the delicate interplay between triple gauge couplings, quartic gauge interactions, and Higgs-mediated diagrams — a powerful window into the structure of electroweak symmetry breaking.

While VBS processes have already been firmly established at the LHC, measuring the longitudinal components of these processes presents an additional layer of difficulty, due to the challenge of separating longitudinally polarized states from their transverse counterparts. To develop techniques and build sensitivity, early measurements presented in Chapter 2 have focused on inclusive diboson production (VV), where first hints of double longitudinal polarization have emerged. Yet, these results still fall short of isolating the true longitudinal dynamics we seek — for that, we need more data and refined analysis strategies. The ongoing LHC Run-3 and improvements in analysis methods may soon allow us to reach the level of observation for longitudinal interactions in inclusive diboson production.

The situation is much more challenging for vector boson scattering processes ($VVjj$), which have cross sections roughly an order of magnitude smaller. Even by combining LHC Run 2 and Run 3 datasets, fully leptonic VBS channels may not yield enough sensitivity. Projections for the High-Luminosity LHC (HL-LHC), based on fully leptonic decays of the vector bosons, suggest that the $W^{\pm}W^{\pm}jj$ channel is the most promising avenue to establish longitudinal VBS. However, even in this channel — as well as in $WZjj$ and $ZZjj$ — current estimates indicate that no single experiment will reach a 3σ significance without further innovation [135, 230–233]. Nevertheless, the use of more sophisticated analysis strategies — particularly those leveraging deep learning — can significantly boost sensitivity to longitudinal VBS. This has already been demonstrated in the recently publish $W^{\pm}W^{\pm}jj$ channel with leptonic decays [80], where machine learning techniques enhance the separation between polarizations and signal-to-background discrimination reaching already the evidence threshold for single boson polarization.

Looking for new ideas, a key question gaining traction in current discussions is whether hadronic or semi-leptonic final states could also be used to access polarization information [234]. Can we extract polarization observables from bosons decaying into jets? Could we develop a polarized boson tagger, capable of identifying longitudinally polarized W and Z bosons in hadronic decays? This idea, once deemed unfeasible, is now being revisited thanks to two major developments: the advent of detector-level simulations with polarized bosons, and the rapid progress in machine learning techniques for jet substructure analysis. While many technical challenges remain, these advances make the prospect of polarization measurements in hadronic channels more realistic than ever. Unlocking this capability would open a new, complementary path toward understanding the dynamics of electroweak symmetry breaking — and could prove pivotal in the HL-LHC era.

Acknowledgements

Pursuing a deeper understanding of the fundamental laws of nature is one of the most exciting journeys one can take—and doing so within a collaborative, multicultural environment makes it even more meaningful. Particle physics has offered me both: the thrill of exploring the universe at its most elementary level, and the privilege of learning from and working alongside inspiring people from all over the world. Through this field, I've grown not only as a physicist but also as a person, gaining insight into different perspectives, cultures, and ways of thinking.

I feel incredibly fortunate to have crossed paths with outstanding mentors who have guided, supported, and trusted me throughout my career. I am especially grateful to Samira, who was not only an extraordinary advisor during my PhD but also a role model in every sense. I often say I miss her every day. That time working with her was a turning point: I felt grounded, reassured, and even had the impression she helped organize my entire life!

I also want to thank Michael Kobel—my years as a postdoc in Dresden will always hold a special place in my heart. His openness, his insightful view of physics, and his trust in me had a profound impact. Thank you, Michael, for welcoming me into your group, for listening, and for offering your wise guidance.

To the Dresden students I had the joy of supervising—Carsten, Stefanie, Tim, Jan-Eric, Abhishek, Max, Anna, Lisa—thank you for teaching me so much. Each of you brought something unique, and I learned through your questions, our discussions, the ideas we dared to test. I truly enjoyed coming to work: our lunch conversations, the spontaneous brainstorming, the barbecues and birthday celebrations—it all made science feel vibrant and alive.

I also want to thank the broader scientific community that has shaped and supported my work—especially my colleagues and friends from CERN, VBSCan, and COMETA. Your collaboration and insight have greatly enriched my perspective. In particular, I'd like to thank Frank Siegert for the discussions, and Chara Petridou for her valuable advice, and continued encouragement throughout the years.

Joining the L2IT laboratory and the IN2P3 in Toulouse has marked a new and exciting chapter. I feel truly fortunate to have become part of this dynamic and growing research environment, and to contribute to its development. Being involved in the early stages of a new laboratory has been both a challenge and a joy. I'm deeply thankful for the warm welcome from my colleagues and for the energy and curiosity of the students. It is a privilege to be back in France and to continue this journey surrounded by such a vibrant and inspiring scientific community.

None of this would have been possible without the unwavering support of my family. My husband Heberth, my companion of over 20 years, has walked with me through each move, every dream, and all the discoveries along the way. Thank you for your patience, your listening ear, and your love as a co-parent and partner. To our daughter Lucia, who is the best thing that has ever happened to me: thank you for grounding me and reminding me what truly matters. And to my sisters Eli and Andrea, and my parents—especially my mother—for your constant love, encouragement, and all the hours of babysitting.

Bibliography

[1] ATLAS Collaboration, *Observation of Light-by-Light Scattering in Ultraperipheral Pb+Pb Collisions with the ATLAS Detector*, Phys. Rev. Lett. **123** (2019) 052001, arXiv: 1904.03536 [hep-ex] (cit. on p. 3).

[2] ATLAS Collaboration, *Evidence for the production of three massive vector bosons with the ATLAS detector*, Phys. Lett. B **798** (2019) 134913, arXiv: 1903.10415 [hep-ex] (cit. on p. 3).

[3] CMS Collaboration, *Observation of the production of three massive gauge bosons at* $\sqrt{s} = 13$ *TeV*, Phys. Rev. Lett. **125** (2020) 151802, arXiv: 2006.11191 [hep-ex] (cit. on p. 3).

[4] ATLAS Collaboration, *Observation of electroweak production of* W^+W^- *in association with jets in proton–proton collisions at* $\sqrt{s} = 13$ *TeV with the ATLAS Detector*, JHEP **07** (2024) 254, arXiv: 2403.04869 [hep-ex] (cit. on pp. 3, 26).

[5] ATLAS Collaboration, *Observation of Electroweak Production of a Same-Sign W Boson Pair in Association with Two Jets in* pp *Collisions at* $\sqrt{s} = 13$ *TeV with the ATLAS Detector*, Phys. Rev. Lett. **123** (2019) 161801, arXiv: 1906.03203 [hep-ex] (cit. on pp. 3, 17, 18, 24, 27, 30, 32, 35, 68, 69).

[6] ATLAS Collaboration, *Observation of electroweak production of two jets and a Z-boson pair*, Nature Phys. **19** (2023) 237, arXiv: 2004.10612 [hep-ex] (cit. on p. 3).

[7] ATLAS Collaboration, *Observation of electroweak* $W^{\pm}Z$ *boson pair production in association with two jets in* pp *collisions at* $\sqrt{s} = 13$ *TeV with the ATLAS detector*, Phys. Lett. B **793** (2019) 469, arXiv: 1812.09740 [hep-ex] (cit. on pp. 3, 24, 30, 68, 69).

[8] L. Evans and P. Bryant, *LHC Machine*, JINST **3** (2008) S08001 (cit. on p. 5).

[9] ATLAS Collaboration, *ATLAS Luminosity Results for Run-3 of the LHC*, (2025), URL: https://twiki.cern.ch/twiki/bin/view/AtlasPublic/LuminosityPublicResultsRun3, (accessed: 26.02.2025) (cit. on p. 6).

[10] J. Manjarrés et al., *Performances of anode-resistive Micromegas for HL-LHC*, JINST **7** (2012) C03040, ISSN: 1748-0221, URL: http://dx.doi.org/10.1088/1748-0221/7/03/C03040 (cit. on p. 6).

[11] ATLAS Collaboration, *The ATLAS Collaboration Software and Firmware*, ATL-SOFT-PUB-2021-001, 2021, URL: https://cds.cern.ch/record/2767187 (cit. on p. 8).

[12] ATLAS Collaboration, *Electron and photon energy calibration with the ATLAS detector using LHC Run 2 data*, JINST **19** (2024) P02009, arXiv: 2309.05471 [hep-ex] (cit. on pp. 9, 10).

[13] ATLAS Collaboration, *Electron reconstruction and identification in the ATLAS experiment using the 2015 and 2016 LHC proton–proton collision data at* $\sqrt{s} = 13$ *TeV*, Eur. Phys. J. C **79** (2019) 639, arXiv: 1902.04655 [physics.ins-det] (cit. on p. 9).

[14] ATLAS Collaboration,
Topological cell clustering in the ATLAS calorimeters and its performance in LHC Run 1,
Eur. Phys. J. C **77** (2017) 490, arXiv: 1603.02934 [hep-ex] (cit. on p. 9).

[15] A. S. Tegetmeier, *Calorimeter-seeded tracking pass for ITk*, tech. rep., CERN, 2024,
URL: https://cds.cern.ch/record/2906255 (cit. on p. 9).

[16] ATLAS Collaboration, *Electron and photon performance measurements with the ATLAS detector using the 2015–2017 LHC proton–proton collision data*, JINST **14** (2019) P12006,
arXiv: 1908.00005 [hep-ex] (cit. on pp. 9, 10, 31).

[17] ATLAS Collaboration, *Muon reconstruction and identification efficiency in ATLAS using the full Run 2 pp collision data set at $\sqrt{s} = 13$ TeV*, Eur. Phys. J. C **81** (2021) 578,
arXiv: 2012.00578 [hep-ex] (cit. on pp. 9, 10, 31).

[18] ATLAS Collaboration, *Jet energy scale and resolution measured in proton–proton collisions at $\sqrt{s} = 13$ TeV with the ATLAS detector*, Eur. Phys. J. C **81** (2021) 689,
arXiv: 2007.02645 [hep-ex] (cit. on p. 9).

[19] ATLAS Collaboration, *Optimisation of large-radius jet reconstruction for the ATLAS detector in 13 TeV proton–proton collisions*, Eur. Phys. J. C **81** (2021) 334, arXiv: 2009.04986 [hep-ex] (cit. on p. 9).

[20] M. Cacciari, G. P. Salam, and G. Soyez, *The anti-k_t jet clustering algorithm*, JHEP **04** (2008) 063,
arXiv: 0802.1189 [hep-ph] (cit. on p. 9).

[21] D. Krohn, J. Thaler, and L.-T. Wang, *Jet trimming*, Journal of High Energy Physics **2010** (2010),
ISSN: 1029-8479, URL: http://dx.doi.org/10.1007/JHEP02(2010)084 (cit. on p. 9).

[22] ATLAS Collaboration,
Transformer networks for constituent-based b-jet calibration with the ATLAS detector,
ATL-PHYS-PUB-2024-015, 2024,
URL: https://cds.cern.ch/record/https://cds.cern.ch/record/2905688
(cit. on pp. 9, 11).

[23] ATLAS Collaboration, *Performance of missing transverse momentum reconstruction with the ATLAS detector using proton–proton collisions at $\sqrt{s} = 13$ TeV*, Eur. Phys. J. C **78** (2018) 903,
arXiv: 1802.08168 [hep-ex] (cit. on p. 10).

[24] ATLAS Collaboration, *The performance of missing transverse momentum reconstruction and its significance with the ATLAS detector using 140 fb^{-1} of $\sqrt{s} = 13$ TeV pp collisions*, (2024),
arXiv: 2402.05858 [hep-ex] (cit. on p. 10).

[25] S. Navas et al., *Review of particle physics*, Phys. Rev. D **110** (2024) 030001 (cit. on p. 10).

[26] CERN, *CERN Yellow Reports: Monographs, Vol 2 (2017): Handbook of LHC Higgs cross sections: 4. Deciphering the nature of the Higgs sector*, (2017),
URL: https://e-publishing.cern.ch/index.php/CYRM/issue/view/32 (cit. on p. 10).

[27] ATLAS Collaboration, *New techniques for jet calibration with the ATLAS detector*,
Eur. Phys. J. C **83** (2023) 761, arXiv: 2303.17312 [hep-ex] (cit. on p. 10).

[28] ATLAS Collaboration, *Measurement of the W-boson mass and width with the ATLAS detector using proton–proton collisions at $\sqrt{s} = 7$ TeV*, Eur. Phys. J. C **84** (2024) 1309,
arXiv: 2403.15085 [hep-ex] (cit. on p. 10).

[29] ATLAS Collaboration,
Improving jet substructure performance in ATLAS using Track-CaloClusters,
ATL-PHYS-PUB-2017-015, 2017, URL: https://cds.cern.ch/record/2275636
(cit. on p. 11).

[30] S. L. Glashow, *Partial-symmetries of weak interactions*, Nuclear Physics **22** (1961) 579
(cit. on p. 12).

[31] S. Weinberg, *A Model of Leptons*, Phys. Rev. Lett. **19** (21 1967) 1264 (cit. on p. 12).

[32] A. Salam, *Weak and electromagnetic interactions, Selected Papers of Abdus Salam*,
Conf. Proc. C 680519 (1968) 244 (cit. on p. 12).

[33] C. S. Wu, E. Ambler, R. W. Hayward, D. D. Hoppes, and R. P. Hudson,
Experimental Test of Parity Conservation in Beta Decay, Phys. Rev. **105** (4 1957) 1413,
URL: https://link.aps.org/doi/10.1103/PhysRev.105.1413 (cit. on p. 13).

[34] P. W. Higgs, *Broken Symmetries and the Masses of Gauge Bosons*,
Phys. Rev. Lett. **13** (16 1964) 508,
URL: https://link.aps.org/doi/10.1103/PhysRevLett.13.508 (cit. on pp. 13, 36).

[35] F. Englert and R. Brout, *Broken Symmetry and the Mass of Gauge Vector Mesons*,
Phys. Rev. Lett. **13** (9 1964) 321,
URL: https://link.aps.org/doi/10.1103/PhysRevLett.13.321 (cit. on pp. 13, 36).

[36] G. S. Guralnik, C. R. Hagen, and T. W. B. Kibble,
Global Conservation Laws and Massless Particles, Phys. Rev. Lett. **13** (20 1964) 585,
URL: https://link.aps.org/doi/10.1103/PhysRevLett.13.585 (cit. on pp. 13, 36).

[37] A. Denner and T. Hahn,
Radiative corrections to $W^+W^- \to W^+W^-$in the electroweak standard model,
Nuclear Physics B **525** (1998) 27 (cit. on pp. 14, 16).

[38] B. Biedermann, A. Denner, and M. Pellen,
Complete NLO corrections to W^+W^+ scattering and its irreducible background at the LHC,
Journal of High Energy Physics **2017** (2017), ISSN: 1029-8479,
URL: http://dx.doi.org/10.1007/JHEP10(2017)124 (cit. on pp. 18–20).

[39] B. Jäger, C. Oleari, and D. Zeppenfeld,
Next-to-leading order QCD corrections to W^+W^- production via vector-boson fusion,
Journal of High Energy Physics **2006** (2006) 015, ISSN: 1029-8479,
URL: http://dx.doi.org/10.1088/1126-6708/2006/07/015 (cit. on p. 18).

[40] B. Jäger, C. Oleari, and D. Zeppenfeld, *Next-to-leading order QCD corrections to W^+W^+jj and W^-W^-jj and production via weak-boson fusion*, Physical Review D **80** (2009), ISSN: 1550-2368,
URL: http://dx.doi.org/10.1103/PhysRevD.80.034022 (cit. on pp. 18, 19).

[41] A. Ballestrero et al., *Precise predictions for same-sign W-boson scattering at the LHC*,
The European Physical Journal C **78** (2018), ISSN: 1434-6052,
URL: http://dx.doi.org/10.1140/epjc/s10052-018-6136-y (cit. on pp. 18, 20, 22, 27).

[42] A. Denner, L. Hošeková, and S. Kallweit,
Next-to-leading order QCD corrections to W+W+jj production in vector-boson fusion at the LHC,
Physical Review D **86** (2012), ISSN: 1550-2368,
URL: http://dx.doi.org/10.1103/PhysRevD.86.114014 (cit. on p. 19).

[43] F. Campanario, M. Kerner, L. D. Ninh, and D. Zeppenfeld, *Next-to-leading order QCD corrections to< W+W+ and W-W- production in association with two jets*, Physical Review D **89** (2014), ISSN: 1550-2368, URL: http://dx.doi.org/10.1103/PhysRevD.89.054009 (cit. on p. 19).

[44] J. Baglio et al., *Release Note - VBFNLO 2.7.0*, 2014, arXiv: 1404.3940 [hep-ph], URL: https://arxiv.org/abs/1404.3940 (cit. on p. 19).

[45] K. Arnold et al., *Vbfnlo: A parton level Monte Carlo for processes with electroweak bosons*, Computer Physics Communications **180** (2009) 1661, ISSN: 0010-4655, URL: http://dx.doi.org/10.1016/j.cpc.2009.03.006 (cit. on p. 19).

[46] J. Baglio et al., *VBFNLO: A parton level Monte Carlo for processes with electroweak bosons – Manual for Version 3.0*, 2024, arXiv: 1107.4038 [hep-ph], URL: https://arxiv.org/abs/1107.4038 (cit. on p. 19).

[47] J. Alwall et al., *The automated computation of tree-level and next-to-leading order differential cross sections, and their matching to parton shower simulations*, Journal of High Energy Physics **2014** (2014), ISSN: 1029-8479, URL: http://dx.doi.org/10.1007/JHEP07(2014)079 (cit. on p. 19).

[48] A. Denner, D. Lombardi, and C. Schwan, *Double-pole approximation for leading-order semi-leptonic vector-boson scattering at the LHC*, 2024, arXiv: 2406.12301 [hep-ph], URL: https://arxiv.org/abs/2406.12301 (cit. on p. 20).

[49] S. Dawson, *The effective W approximation*, Nuclear Physics B **249** (1985) 42, ISSN: 0550-3213, URL: https://www.sciencedirect.com/science/article/pii/0550321385900380 (cit. on p. 20).

[50] M. Rauch, *Vector-Boson Fusion and Vector-Boson Scattering*, 2016, arXiv: 1610.08420 [hep-ph], URL: https://arxiv.org/abs/1610.08420 (cit. on pp. 20, 21).

[51] B. Jäger and G. Zanderighi, *NLO corrections to electroweak and QCD production of W+W+ plus two jets in the POWHEG BOX*, Journal of High Energy Physics **2011** (2011), ISSN: 1029-8479, URL: http://dx.doi.org/10.1007/JHEP11(2011)055 (cit. on p. 20).

[52] B. Jäger and G. Zanderighi, *Electroweak W+W jj prodution at NLO in QCD matched with parton shower in the POWHEG-BOX*, Journal of High Energy Physics **2013** (2013), ISSN: 1029-8479, URL: http://dx.doi.org/10.1007/JHEP04(2013)024 (cit. on p. 20).

[53] B. Jäger, A. Karlberg, and G. Zanderighi, *Electroweak ZZjj production in the Standard Model and beyond in the POWHEG-BOX V2*, Journal of High Energy Physics **2014** (2014), ISSN: 1029-8479, URL: http://dx.doi.org/10.1007/JHEP03(2014)141 (cit. on p. 20).

[54] M. Bähr et al., *Herwig++ physics and manual*, The European Physical Journal C **58** (2008) 639, ISSN: 1434-6052, URL: http://dx.doi.org/10.1140/epjc/s10052-008-0798-9 (cit. on p. 20).

[55] J. Bellm et al., *Herwig 7.0/Herwig++ 3.0 release note*, The European Physical Journal C **76** (2016), ISSN: 1434-6052, URL: http://dx.doi.org/10.1140/epjc/s10052-016-4018-8 (cit. on p. 20).

[56] B. Biedermann, A. Denner, and M. Pellen, *Large Electroweak Corrections to Vector-Boson Scattering at the Large Hadron Collider*, Physical Review Letters **118** (2017), ISSN: 1079-7114, URL: http://dx.doi.org/10.1103/PhysRevLett.118.261801 (cit. on p. 20).

[57] A. Denner, S. Dittmaier, P. Maierhöfer, M. Pellen, and C. Schwan, *QCD and electroweak corrections to WZ scattering at the LHC*, Journal of High Energy Physics **2019** (2019), ISSN: 1029-8479, URL: http://dx.doi.org/10.1007/JHEP06(2019)067 (cit. on p. 20).

[58] A. Denner, R. Franken, M. Pellen, and T. Schmidt, *NLO QCD and EW corrections to vector-boson scattering into ZZ at the LHC*, Journal of High Energy Physics **2020** (2020), ISSN: 1029-8479, URL: http://dx.doi.org/10.1007/JHEP11(2020)110 (cit. on p. 20).

[59] D. Rainwater, R. Szalapski, and D. Zeppenfeld, *Probing color-singlet exchange in Z+2-jet events at the CERN LHC*, Physical Review D **54** (1996) 6680, ISSN: 1089-4918, URL: http://dx.doi.org/10.1103/PhysRevD.54.6680 (cit. on pp. 20, 21).

[60] S. Todt, *The $W^{\pm}W^{\pm}$ Scattering Process – Theoretical Studies, Observation, Cross-section Measurement, and EFT Reinterpretation at $\sqrt{s}$ = 13 TeV with the ATLAS Detector*, Presented 02 Dec 2022, TU Dresden, 2022, URL: https://cds.cern.ch/record/2845282 (cit. on pp. 22, 26, 32, 50, 63, 64, 67, 70).

[61] C. Gumpert, *Measurement of Electroweak Gauge Boson Scattering in the Channel $pp \to W^{\pm}W^{\pm}jj$ with the ATLAS Detector at the Large Hadron Collider*, Presented 27 Feb 2015, Dresden, Tech. U., Dept. Math., 2014, URL: https://cds.cern.ch/record/2003240 (cit. on p. 23).

[62] ATLAS Collaboration, *Measurements of $W^{\pm}Z$ production cross sections in pp collisions at $\sqrt{s}$ = 8 TeV with the ATLAS detector and limits on anomalous gauge boson self-couplings*, Phys. Rev. D **93** (2016) 092004, arXiv: 1603.02151 [hep-ex] (cit. on pp. 23, 24, 27, 65).

[63] ATLAS Collaboration, *Measurement of $W^{\pm}W^{\pm}$ vector-boson scattering and limits on anomalous quartic gauge couplings with the ATLAS detector*, Phys. Rev. D **96** (2017) 012007, arXiv: 1611.02428 [hep-ex] (cit. on pp. 24, 62, 65).

[64] CMS Collaboration, *Study of vector boson scattering and search for new physics in events with two same-sign leptons and two jets*, Phys. Rev. Lett. **114** (2015) 051801, arXiv: 1410.6315 [hep-ex] (cit. on p. 24).

[65] ATLAS Collaboration, *Studies of $Z\gamma$ production in association with a high-mass dijet system in pp collisions at $\sqrt{s}$ = 8 TeV with the ATLAS detector*, JHEP **07** (2017) 107, arXiv: 1705.01966 [hep-ex] (cit. on pp. 24, 65).

[66] CMS Collaboration, *Observation of Electroweak Production of Same-Sign W Boson Pairs in the Two Jet and Two Same-Sign Lepton Final State in Proton–Proton Collisions at $\sqrt{s}$ = 13 TeV*, Phys. Rev. Lett. **120** (2018) 081801, arXiv: 1709.05822 [hep-ex] (cit. on pp. 24, 53).

[67] CMS Collaboration, *Measurement of electroweak WZ boson production and search for new physics in WZ+ two jets events in pp collisions at $\sqrt{s}$ = 13 TeV*, Phys. Lett. B **795** (2019) 281, arXiv: 1901.04060 [hep-ex] (cit. on pp. 24, 28).

[68] CMS Collaboration,
Measurement of vector boson scattering and constraints on anomalous quartic couplings from events with four leptons and two jets in proton–proton collisions at $\sqrt{s} = 13$ TeV,
Phys. Lett. B **774** (2017) 682, arXiv: 1708.02812 [hep-ex] (cit. on p. 24).

[69] ATLAS Collaboration, *Search for electroweak diboson production in association with a high-mass dijet system in semileptonic final states in pp collisions at $\sqrt{s} = 13$ TeV with the ATLAS detector*,
Phys. Rev. D **100** (2019) 032007, arXiv: 1905.07714 [hep-ex] (cit. on p. 24).

[70] CMS Collaboration, *Measurements of production cross sections of polarized same-sign W boson pairs in association with two jets in proton–proton collisions at $\sqrt{s} = 13$ TeV*,
Phys. Lett. B **812** (2021) 136018, arXiv: 2009.09429 [hep-ex]
(cit. on pp. 24, 26, 41–43, 47, 48).

[71] ATLAS Collaboration, *Measurement and interpretation of same-sign W boson pair production in association with two jets in pp collisions at $\sqrt{s} = 13$ TeV with the ATLAS detector*,
JHEP **04** (2024) 026, arXiv: 2312.00420 [hep-ex] (cit. on pp. 24, 26, 27, 31, 34, 54, 56, 65).

[72] ATLAS Collaboration, *Measurements of electroweak $W^{\pm}Z$ boson pair production in association with two jets in pp collisions at $\sqrt{s} = 13$ TeV with the ATLAS detector*, JHEP **06** (2024) 192,
arXiv: 2403.15296 [hep-ex] (cit. on pp. 24, 26, 65).

[73] R. Frederix and S. Frixione, *Merging meets matching in MC@NLO*, JHEP **12** (2012) 061,
arXiv: 1209.6215 [hep-ph] (cit. on p. 25).

[74] J. Alwall et al., *The automated computation of tree-level and next-to-leading order differential cross sections, and their matching to parton shower simulations*, JHEP **07** (2014) 079,
arXiv: 1405.0301 [hep-ph] (cit. on p. 25).

[75] D. B. Franzosi, O. Mattelaer, R. Ruiz, and S. Shil,
Automated predictions from polarized matrix elements, JHEP **04** (2020) 082,
arXiv: 1912.01725 [hep-ph] (cit. on pp. 25, 27, 38, 39).

[76] E. Bothmann et al., *Event Generation with Sherpa 2.2*, SciPost Phys. **7** (2019) 034,
arXiv: 1905.09127 [hep-ph] (cit. on pp. 26, 27).

[77] CMS Collaboration, *Observation of electroweak W^+W^- pair production in association with two jets in proton–proton collisions at $\sqrt{s} = 13$ TeV*, Phys. Lett. B **841** (2023) 137495,
arXiv: 2205.05711 [hep-ex] (cit. on p. 26).

[78] CMS Collaboration, *Evidence for WW/WZ vector boson scattering in the decay channel $\ell\nu qq$ produced in association with two jets in proton–proton collisions at $\sqrt{s} = 13$ TeV*,
Phys. Lett. B **834** (2022) 137438, arXiv: 2112.05259 [hep-ex] (cit. on p. 26).

[79] A. Collaboration, *Electroweak diboson production in association with a high-mass dijet system in semileptonic final states from pp collisions at $\sqrt{s} = 13$ TeV with the ATLAS detector*, (2025),
arXiv: 2503.17461 [hep-ex], URL: https://arxiv.org/abs/2503.17461 (cit. on p. 26).

[80] ATLAS Collaboration,
Evidence for longitudinally polarized W bosons in the electroweak production of same-sign W boson pairs in association with two jets in pp collisions at $\sqrt{s} = 13$ TeV with the ATLAS detector,
(2025), arXiv: 2503.11317 [hep-ex], URL: https://arxiv.org/abs/2503.11317
(cit. on pp. 26, 41–43, 47, 48, 80).

[81] F. Iltzsche, *Observation of Electroweak Same-Charge $W^{\pm}W^{\pm}jj$ Production at $\sqrt{s} = 13$ TeV with the ATLAS Detector at the LHC*, Presented 27 Sep 2019, Dresden, Tech. U., 2019, URL: https://cds.cern.ch/record/2697175 (cit. on pp. 26, 32).

[82] A. S. Tegetmeier, *Study on the discrimination of quark and gluon jet events of the scattering of weak gauge bosons W and Z with the the ATLAS detector*, Presented 24 Sep 2019, TU Dresden, 2019, URL: https://cds.cern.ch/record/2814729 (cit. on pp. 26, 31).

[83] T. Herrmann, *Total and Differential Cross-Section Measurement and Interpretation of $W^{\pm}W^{\pm}$ Scattering in Effective Field Theories with the Run 2 Data of the ATLAS Experiment*, Presented 27 Sep 2023, TU Dresden, 2023, URL: https://cds.cern.ch/record/2914984 (cit. on pp. 27, 32).

[84] M. V. Stange, *Data-driven estimation of the non-prompt background in same charged $W^{\pm}W^{\pm}$ scattering within the ATLAS experiment*, Presented 05 Nov 2020, Dresden, Tech. U., 2020, URL: https://cds.cern.ch/record/2746597 (cit. on pp. 27, 31).

[85] C. Bittrich, *Evidence for Scattering of Electroweak Gauge Bosons in the $W^{\pm}Z$ Channel with the ATLAS Detector at the Large Hadron Collider*, Presented 14 Jul 2020, Dresden, Tech. U., 2020, URL: https://cds.cern.ch/record/2719126 (cit. on pp. 27, 28).

[86] T. Sjöstrand, S. Mrenna, and P. Skands, *A brief introduction to PYTHIA 8.1*, Comput. Phys. Commun. **178** (2008) 852, arXiv: 0710.3820 [hep-ph] (cit. on p. 27).

[87] L. Lönnblad, *Correcting the Colour-Dipole Cascade Model with Fixed Order Matrix Elements*, JHEP **05** (2002) 046, arXiv: hep-ph/0112284 (cit. on p. 28).

[88] ATLAS Collaboration, *Electron Identification with a Convolutional Neural Network in the ATLAS Experiment*, ATL-PHYS-PUB-2023-001, 2023, URL: https://cds.cern.ch/record/2850666 (cit. on p. 31).

[89] ATLAS Collaboration, *Performance and calibration of quark/gluon-jet taggers using 140 fb^{-1} of pp collisions at $\sqrt{s} = 13$ TeV with the ATLAS detector*, Chin. Phys. C **48** (2024) 023001, arXiv: 2308.00716 [hep-ex] (cit. on p. 31).

[90] *VBSCan COST Network*, https://vbscanaction.web.cern.ch/, Accessed: 2021-09-30 (cit. on p. 33).

[91] ATLAS Collaboration, *Search for leptonic charge asymmetry in $t\bar{t}W$ production in final states with three leptons at $\sqrt{s} = 13$ TeV*, JHEP **07** (2023) 033, arXiv: 2301.04245 [hep-ex] (cit. on p. 33).

[92] R. Franceschini, G. Panico, A. Pomarol, F. Riva, and A. Wulzer, *Electroweak Precision Tests in High-Energy Diboson Processes*, JHEP **02** (2018) 111, arXiv: 1712.01310 [hep-ph] (cit. on p. 36).

[93] D. Liu and L.-T. Wang, *Prospects for precision measurement of diboson processes in the semileptonic decay channel in future LHC runs*, Phys. Rev. D **99** (2019) 055001, arXiv: 1804.08688 [hep-ph] (cit. on p. 36).

[94] G. Valencia and S. Willenbrock, *Goldstone-boson equivalence theorem and the Higgs resonance*, Phys. Rev. D **42** (3 1990) 853, URL: https://link.aps.org/doi/10.1103/PhysRevD.42.853 (cit. on p. 36).

[95] Z. Bern et al., *Left-handed<mml:math xmlns:mml="http://www.w3.org/1998/Math/MathML" display="inline"><mml:mi>W</mml:mi></mml:math>bosons at the LHC*, Physical Review D **84** (2011), ISSN: 1550-2368, URL: http://dx.doi.org/10.1103/PhysRevD.84.034008 (cit. on pp. 37, 41).

[96] W. J. Stirling and E. Vryonidou, *Electroweak gauge boson polarisation at the LHC*, Journal of High Energy Physics **2012** (2012), ISSN: 1029-8479, URL: http://dx.doi.org/10.1007/JHEP07(2012)124 (cit. on pp. 37, 41).

[97] A. Denner, S. Dittmaier, M. Roth, and D. Wackeroth, *Electroweak radiative corrections to e+e→WW→4 fermions in double-pole approximation — the RacoonWW approach*, Nuclear Physics B **587** (2000) 67, ISSN: 0550-3213, URL: http://dx.doi.org/10.1016/S0550-3213(00)00511-3 (cit. on p. 38).

[98] A. Ballestrero, E. Maina, and G. Pelliccioli, *W boson polarization in vector boson scattering at the LHC*, Journal of High Energy Physics **2018** (2018), ISSN: 1029-8479, URL: http://dx.doi.org/10.1007/JHEP03(2018)170 (cit. on pp. 38, 39).

[99] P. Artoisenet, R. Frederix, O. Mattelaer, and R. Rietkerk, *Automatic spin-entangled decays of heavy resonances in Monte Carlo simulations*, Journal of High Energy Physics **2013** (2013), ISSN: 1029-8479, URL: http://dx.doi.org/10.1007/JHEP03(2013)015 (cit. on p. 38).

[100] J. Baglio and D. N. Le, *Polarization Observables in WZ Production at the 13 TeV LHC: Inclusive Case*, Communications in Physics **30** (2020) 35, ISSN: 0868-3166, URL: http://dx.doi.org/10.15625/0868-3166/30/1/14461 (cit. on p. 38).

[101] A. Denner and G. Pelliccioli, *Polarized electroweak bosons in W+W production at the LHC including NLO QCD effects*, Journal of High Energy Physics **2020** (2020), ISSN: 1029-8479, URL: http://dx.doi.org/10.1007/JHEP09(2020)164 (cit. on pp. 38, 39).

[102] A. Denner and G. Pelliccioli, *NLO QCD predictions for doubly-polarized WZ production at the LHC*, Physics Letters B **814** (2021) 136107, ISSN: 0370-2693, URL: http://dx.doi.org/10.1016/j.physletb.2021.136107 (cit. on pp. 38, 39).

[103] A. Denner, C. Haitz, and G. Pelliccioli, *NLO QCD corrections to polarized diboson production in semileptonic final states*, Physical Review D **107** (2023), ISSN: 2470-0029, URL: http://dx.doi.org/10.1103/PhysRevD.107.053004 (cit. on pp. 38, 39).

[104] A. Denner, C. Haitz, and G. Pelliccioli, *NLO EW and QCD corrections to polarised same-sign WW scattering at the LHC*, 2024, arXiv: 2409.03620 [hep-ph], URL: https://arxiv.org/abs/2409.03620 (cit. on pp. 38, 39).

[105] G. Pelliccioli and G. Zanderighi, *Polarised-boson pairs at the LHC with NLOPS accuracy*, (2023), arXiv: 2311.05220 [hep-ph] (cit. on pp. 38, 39).

[106] A. Ballestrero, A. Belhouari, G. Bevilacqua, V. Kashkan, and E. Maina, *PHANTOM: A Monte Carlo event generator for six parton final states at high energy colliders*, Computer Physics Communications **180** (2009) 401, ISSN: 0010-4655, URL: http://dx.doi.org/10.1016/j.cpc.2008.10.005 (cit. on pp. 38, 39).

[107] M. Javurkova, R. Ruiz, R. C. Lopes de Sá, and J. Sandesara, *Polarized ZZ pairs in gluon fusion and vector boson fusion at the LHC*, Physics Letters B **855** (2024) 138787, ISSN: 0370-2693, URL: http://dx.doi.org/10.1016/j.physletb.2024.138787 (cit. on p. 38).

[108] M. Hoppe, M. Schönherr, and F. Siegert, *Polarised cross sections for vector boson production with SHERPA*, (2023), arXiv: 2310.14803 [hep-ph], URL: https://arxiv.org/abs/2310.14803 (cit. on pp. 38–40).

[109] M. Czakon, *A novel subtraction scheme for double-real radiation at NNLO*, Physics Letters B **693** (2010) 259, ISSN: 0370-2693, URL: http://dx.doi.org/10.1016/j.physletb.2010.08.036 (cit. on p. 39).

[110] J. Baglio and L. D. Ninh, *Fiducial polarization observables in hadronic WZ production: A next-to-leading order QCD+EW study*, JHEP **04** (2019) 065, arXiv: 1810.11034 [hep-ph] (cit. on p. 39).

[111] D. N. Le and J. Baglio, *Doubly-polarized WZ hadronic cross sections at NLO QCD+EW accuracy*, 2022, arXiv: 2203.01470 [hep-ph], URL: https://arxiv.org/abs/2203.01470 (cit. on pp. 39, 40).

[112] T. N. Dao and D. N. Le, *Enhancing the doubly-longitudinal polarization in WZ production at the LHC*, Commun. in Phys. **33** (2023) 223, arXiv: 2302.03324 [hep-ph] (cit. on pp. 39, 40, 46).

[113] A. Ballestrero, E. Maina, and G. Pelliccioli, *Different polarization definitions in same-sign WW scattering at the LHC*, Physics Letters B **811** (2020) 135856, ISSN: 0370-2693, URL: https://www.sciencedirect.com/science/article/pii/S0370269320306596 (cit. on pp. 38, 39).

[114] R. Poncelet and A. Popescu, *NNLO QCD study of polarised $W+W$ production at the LHC*, Journal of High Energy Physics **2021** (2021), ISSN: 1029-8479, URL: http://dx.doi.org/10.1007/JHEP07(2021)023 (cit. on p. 39).

[115] A. Denner and G. Pelliccioli, *NLO EW and QCD corrections to polarized ZZ production in the four-charged-lepton channel at the LHC*, Journal of High Energy Physics **2021** (2021), ISSN: 1029-8479, URL: http://dx.doi.org/10.1007/JHEP10(2021)097 (cit. on p. 39).

[116] D. N. Le, J. Baglio, and T. N. Dao, *Doubly-polarized WZ hadronic production at NLO QCD+EW: Calculation method and further results*, 2022, arXiv: 2208.09232 [hep-ph], URL: https://arxiv.org/abs/2208.09232 (cit. on p. 39).

[117] A. Denner, C. Haitz, and G. Pelliccioli, *NLO EW corrections to polarised W^+W^- production and decay at the LHC*, 2023, arXiv: 2311.16031 [hep-ph], URL: https://arxiv.org/abs/2311.16031 (cit. on p. 39).

[118] T. N. Dao and D. N. Le,
NLO electroweak corrections to doubly-polarized W^+W^- production at the LHC,
The European Physical Journal C **84** (2024), ISSN: 1434-6052,
URL: `http://dx.doi.org/10.1140/epjc/s10052-024-12579-y` (cit. on p. 39).

[119] T. N. Dao and D. N. Le, *Polarized W^+W^- pairs at the LHC: Effects from bottom-quark induced processes at NLO QCD+EW*, 2024, arXiv: `2409.06396 [hep-ph]`,
URL: `https://arxiv.org/abs/2409.06396` (cit. on p. 39).

[120] A. Ballestrero, E. Maina, and G. Pelliccioli,
Polarized vector boson scattering in the fully leptonic WZ and ZZ channels at the LHC,
Journal of High Energy Physics **2019** (2019), ISSN: 1029-8479,
URL: `http://dx.doi.org/10.1007/JHEP09(2019)087` (cit. on p. 39).

[121] G. Pelliccioli and G. Zanderighi, *Polarised-boson pairs at the LHC with NLOPS accuracy*,
Eur. Phys. J. C 84, 16 (2024), arXiv: `2311.05220 [hep-ph]`,
URL: `https://arxiv.org/abs/2311.05220` (cit. on p. 40).

[122] L3 Collaboration, *Measurement of W polarisation at LEP*, Physics Letters B **557** (2003) 147,
ISSN: 0370-2693, URL: `http://dx.doi.org/10.1016/S0370-2693(03)00172-2`
(cit. on p. 41).

[123] OPAL Collaboration, *W boson polarisation at LEP2*, Physics Letters B **585** (2004) 223,
ISSN: 0370-2693, URL: `http://dx.doi.org/10.1016/j.physletb.2004.02.003`
(cit. on p. 41).

[124] DELPHI Collaboration, *Study of W-boson polarisations and triple gauge boson couplings in the reaction e^+e^-ßW$^+$W$^-$ at LEP 2*, The European Physical Journal C **54** (2008) 345,
ISSN: 1434-6052, URL: `http://dx.doi.org/10.1140/epjc/s10052-008-0528-3`
(cit. on p. 41).

[125] OPAL collaboration, *Measurement of W boson polarisations and CP-violating triple gauge couplings from W^+ W^- production at LEP*, The European Physical Journal C **19** (2001) 229,
ISSN: 1434-6052, URL: `http://dx.doi.org/10.1007/s100520100602` (cit. on p. 41).

[126] D. Collaboration, *Correlations between polarisation states of W particles in the reaction e e
+→W W + at LEP2 energies 189–209 GeV*, The European Physical Journal C **63** (2009) 611,
ISSN: 1434-6052, URL: `http://dx.doi.org/10.1140/epjc/s10052-009-1123-y`
(cit. on p. 41).

[127] CMS Collaboration, *Measurement of the inclusive and differential WZ production cross sections, polarization angles, and triple gauge couplings in pp collisions at $\sqrt{s}$ = 13 TeV*,
JHEP **07** (2022) 032, arXiv: `2110.11231 [hep-ex]` (cit. on pp. 41, 42).

[128] ATLAS Collaboration, *Measurement of $W^\pm Z$ production cross sections and gauge boson polarisation in pp collisions at $\sqrt{s}$ = 13 TeV with the ATLAS detector*,
Eur. Phys. J. C **79** (2019) 535, arXiv: `1902.05759 [hep-ex]` (cit. on pp. 41, 42, 47, 48).

[129] ATLAS Collaboration, *Studies of the Energy Dependence of Diboson Polarization Fractions and the Radiation-Amplitude-Zero Effect in WZ Production with the ATLAS Detector*,
Phys. Rev. Lett. **133** (2024) 101802, arXiv: `2402.16365 [hep-ex]` (cit. on pp. 41–43, 45, 47, 48),
Erratum: Phys. Rev. Lett. **133** (2024) 169901.

[130] ATLAS Collaboration, *Evidence of pair production of longitudinally polarised vector bosons and study of CP properties in $ZZ \to 4\ell$ events with the ATLAS detector at $\sqrt{s} = 13$ TeV*, JHEP **12** (2023) 107, arXiv: 2310.04350 [hep-ex] (cit. on pp. 41, 42, 48).

[131] CMS Collaboration, *Measurement of the Polarization of W Bosons with Large Transverse Momenta in W+Jets Events at the LHC*, Phys. Rev. Lett. **107** (2011) 021802, arXiv: 1104.3829 [hep-ex] (cit. on p. 42).

[132] ATLAS Collaboration, *Measurement of the polarisation of W bosons produced with large transverse momentum in pp collisions at $\sqrt{s} = 7$ TeV with the ATLAS experiment*, Eur. Phys. J. C **72** (2012) 2001, arXiv: 1203.2165 [hep-ex] (cit. on p. 42).

[133] ATLAS Collaboration, *Observation of gauge boson joint-polarisation states in $W^{\pm}Z$ production from pp collisions at $\sqrt{s} = 13$ TeV with the ATLAS detector*, Phys. Lett. B **843** (2023) 137895, arXiv: 2211.09435 [hep-ex] (cit. on p. 42).

[134] J.-E. Nitschke, *Observation of Longitudinal-Longitudinal Interactions at High p_T^Z and Studies of the Radiation Amplitude Zero Effect in $W^{\pm}Z$ Events with the ATLAS Detector at the Large Hadron Collider*, Presented 17 Apr 2024, Dresden, Tech. U., 2024, URL: https://cds.cern.ch/record/2896505 (cit. on pp. 43, 46).

[135] A. S. Tegetmeier, *Multivariate Analysis of Polarized Vector Boson Scattering of a W and Z Boson with the ATLAS Detector*, Presented 2022, TU Dresden, 2022, URL: https://cds.cern.ch/record/2842600 (cit. on pp. 43, 48, 80).

[136] S. Frixione, P. Nason, and G. Ridolfi, *Strong corrections to WZ production at hadron colliders*, Nucl. Phys. B **383** (1992) 3 (cit. on pp. 43, 44).

[137] U. Baur, T. Han, and J. Ohnemus, *Amplitude zeros in $W^{\pm}Z$ production*, Phys. Rev. Lett. **72** (1994) 3941, arXiv: hep-ph/9403248 (cit. on pp. 43, 44).

[138] J. N. Liebig, *Higher Order Studies of Polarization Effects in W±Z Production at the LHC With Sherpa*, Presented 19 Mar 2024, Dresden, Tech. U., 2024, URL: https://cds.cern.ch/record/2890370 (cit. on p. 44).

[139] D0 Collaboration, *First study of the radiation-amplitude zero in $W\gamma$ production and limits on anomalous $WW\gamma$ couplings at $\sqrt{s} = 1.96$ TeV*, Phys. Rev. Lett. **100** (2008) 241805, arXiv: 0803.0030 [hep-ex] (cit. on p. 44).

[140] CMS Collaboration, *Measurement of the $W\gamma$ and $Z\gamma$ inclusive cross sections in pp collisions at $\sqrt{s} = 7$ TeV and limits on anomalous triple gauge boson couplings*, Phys. Rev. D **89** (2014) 092005, arXiv: 1308.6832 [hep-ex] (cit. on p. 44).

[141] CMS Collaboration, *Measurement of $W^{\pm}\gamma$ differential cross sections in proton–proton collisions at $\sqrt{s} = 13$ TeV and effective field theory constraints*, Phys. Rev. D **105** (2022) 052003, arXiv: 2111.13948 [hep-ex] (cit. on p. 44).

[142] R. Capdevilla, R. Harnik, and A. Martin, *The radiation valley and exotic resonances in $W\gamma$ production at the LHC*, JHEP **03** (2020) 117, arXiv: 1912.08234 [hep-ph] (cit. on p. 44).

[143] C. L. Bilchak, R. W. Brown, and J. D. Stroughair, *$W^{\pm}$ and Z^0 polarization in pair production: Dominant helicities*, Phys. Rev. D **29** (1984) 375 (cit. on p. 44).

[144] U. Baur, T. Han, and J. Ohnemus,
WZ production at hadron colliders: Effects of nonstandard WWZ couplings and QCD corrections,
Phys. Rev. D **51** (1995) 3381, arXiv: hep-ph/9410266 [hep-ph] (cit. on p. 44).

[145] C. Frye, M. Freytsis, J. Scholtz, and M. J. Strassler, *Precision Diboson Observables for the LHC*,
JHEP **03** (2016) 171, arXiv: 1510.08451 [hep-ph] (cit. on p. 44).

[146] K. Cranmer, G. Lewis, L. Moneta, A. Shibata, and W. Verkerke,
HistFactory: A tool for creating statistical models for use with RooFit and RooStats,
CERN-OPEN-2012-016, 2012, URL: https://cds.cern.ch/record/1456844 (cit. on p. 45).

[147] M. Gonzalez-Garcia and M. Maltoni, *Phenomenology with massive neutrinos*,
Physics Reports **460** (2008), ISSN: 0370-1573,
URL: http://dx.doi.org/10.1016/j.physrep.2007.12.004 (cit. on p. 49).

[148] A. Nag, *Search for a new resonance in the WZ leptonic decay channel in proton-proton collisions using the ATLAS detector*, Presented 31-11-2022, Dresden, Tech. U., 2022,
URL: https://cds.cern.ch/record/2825746 (cit. on p. 50).

[149] ATLAS Collaboration,
Summary of Diboson Resonance Searches at the ATLAS experiment using full run-2 data,
ATL-PHYS-PUB-2023-007, 2023, URL: https://cds.cern.ch/record/2853753
(cit. on pp. 51, 54).

[150] D. Pappadopulo, A. Thamm, R. Torre, and A. Wulzer,
Heavy vector triplets: bridging theory and data, Journal of High Energy Physics **2014** (2014),
ISSN: 1029-8479, URL: http://dx.doi.org/10.1007/JHEP09(2014)060 (cit. on p. 52).

[151] H. Georgi and M. Machacek, *Doubly charged Higgs bosons*, Nucl. Phys. B **262** (1985) 463
(cit. on p. 52).

[152] M. S. Chanowitz and M. Golden, *Higgs boson triplets with* $M(W) = M(Z)\cos\theta_W$,
Phys. Lett. B **165** (1985) 105 (cit. on p. 52).

[153] J. de Blas, J. M. Lizana, and M. Perez-Victoria, *Combining searches of Z' and W' bosons*,
JHEP **01** (2013) 166, arXiv: 1211.2229 [hep-ph] (cit. on p. 52).

[154] D. Pappadopulo, A. Thamm, R. Torre, and A. Wulzer,
Heavy vector triplets: bridging theory and data, JHEP **09** (2014) 060,
arXiv: 1402.4431 [hep-ph] (cit. on p. 52).

[155] D. Greco and D. Liu, *Hunting composite vector resonances at the LHC: naturalness facing data*,
JHEP **12** (2014) 126, arXiv: 1410.2883 [hep-ph] (cit. on p. 52).

[156] K. Hartling, K. Kumar, and H. E. Logan,
Indirect constraints on the Georgi-Machacek model and implications for Higgs boson couplings,
Phys. Rev. D **91** (2015) 015013, arXiv: 1410.5538 [hep-ph] (cit. on p. 52).

[157] ATLAS Collaboration, *ATLAS Heavy Particle Searches - 95% CL Exclusion Limits*, 2021,
URL: https://atlas.web.cern.ch/Atlas/GROUPS/PHYSICS/PUBNOTES/ATL-PHYS-PUB-2021-033/fig_01.png (cit. on p. 53).

[158] ATLAS Collaboration, *Summary of Diboson Resonance Searches from the ATLAS Experiment*,
ATL-PHYS-PUB-2021-018, 2021, URL: https://cds.cern.ch/record/2771783
(cit. on p. 53).

[159] CMS Collaboration, *Overview of CMS EXO results*, 2021, URL: https://twiki.cern.ch/twiki/pub/CMSPublic/SummaryPlotsEXO13TeV/CurrentBarChartVersion_v7.svg (cit. on p. 53).

[160] ATLAS Collaboration, *Combination of searches for WW, WZ, and ZZ resonances in pp collisions at $\sqrt{s} = 8$ TeV with the ATLAS detector*, Phys. Lett. B **755** (2016) 285, arXiv: 1512.05099 [hep-ex] (cit. on p. 53).

[161] ATLAS Collaboration, *Searches for heavy diboson resonances in pp collisions at $\sqrt{s} = 13$ TeV with the ATLAS detector*, JHEP **09** (2016) 173, arXiv: 1606.04833 [hep-ex] (cit. on p. 53).

[162] ATLAS Collaboration, *Search for heavy diboson resonances in semileptonic final states in pp collisions at $\sqrt{s} = 13$ TeV with the ATLAS detector*, Eur. Phys. J. C **80** (2020) 1165, arXiv: 2004.14636 [hep-ex] (cit. on p. 53).

[163] CMS Collaboration, *Combination of searches for heavy resonances decaying to WW, WZ, ZZ, WH, and ZH boson pairs in proton–proton collisions at $\sqrt{s} = 8$ TeV and 13 TeV*, Phys. Lett. B **774** (2017) 533, arXiv: 1705.09171 [hep-ex] (cit. on p. 53).

[164] ATLAS Collaboration, *Search for resonances decaying into a weak vector boson and a Higgs boson in the fully hadronic final state produced in proton–proton collisions at $\sqrt{s} = 13$ TeV with the ATLAS detector*, Phys. Rev. D **102** (2020) 112008, arXiv: 2007.05293 [hep-ex] (cit. on p. 53).

[165] ATLAS Collaboration, *Search for heavy resonances decaying into a Z or W boson and a Higgs boson in final states with leptons and b-jets in 139 fb^{-1} of pp collisions at $\sqrt{s} = 13$ TeV with the ATLAS detector*, JHEP **06** (2023) 016, arXiv: 2207.00230 [hep-ex] (cit. on p. 53).

[166] ATLAS Collaboration, *Combination of searches for heavy resonances decaying into bosonic and leptonic final states using 36 fb^{-1} of proton–proton collision data at $\sqrt{s} = 13$ TeV with the ATLAS detector*, Phys. Rev. D **98** (2018) 052008, arXiv: 1808.02380 [hep-ex] (cit. on p. 53).

[167] ATLAS Collaboration, *Search for resonant WZ production in the fully leptonic final state in proton–proton collisions at $\sqrt{s} = 13$ TeV with the ATLAS detector*, Eur. Phys. J. C **83** (2023) 633, arXiv: 2207.03925 [hep-ex] (cit. on pp. 53, 56).

[168] ATLAS Collaboration, *Search for heavy resonances decaying into WW in the $e\nu\mu\nu$ final state in pp collisions at $\sqrt{s} = 13$ TeV with the ATLAS detector*, Eur. Phys. J. C **78** (2018) 24, arXiv: 1710.01123 [hep-ex] (cit. on p. 53).

[169] CMS Collaboration, *Search for charged Higgs bosons produced in vector boson fusion processes and decaying into vector boson pairs in proton–proton collisions at $\sqrt{s} = 13$ TeV*, Eur. Phys. J. C **81** (2021) 723, arXiv: 2104.04762 [hep-ex] (cit. on pp. 53, 54).

[170] G. Cowan, K. Cranmer, E. Gross, and O. Vitells, *Asymptotic formulae for likelihood-based tests of new physics*, Eur. Phys. J. C **71** (2011) 1554, arXiv: 1007.1727 [physics.data-an] (cit. on p. 55), Erratum: Eur. Phys. J. C **73** (2013) 2501.

[171] ATLAS Collaboration, *Combination of searches for singly and doubly charged Higgs bosons produced via vector-boson fusion in proton–proton collisions at $\sqrt{s} = 13$ TeV with the ATLAS detector*, Phys. Lett. B **860** (2025) 139137, arXiv: 2407.10798 [hep-ex] (cit. on p. 56).

[172] *Summary Plots for Heavy Particle Searches and Long-lived Particle Searches - March 2023*, tech. rep., All figures including auxiliary figures are available at https://atlas.web.cern.ch/Atlas/GROUPS/PHYSICS/PUBNOTES/ATL-PHYS-PUB-2023-008: CERN, 2023, URL: https://cds.cern.ch/record/2853754 (cit. on p. 56).

[173] G. GIACOMELLI and R. GIACOMELLI, "THE LEP LEGACY," $e^{\pm}\mu^{\pm}$ Non-Accelerator Astroparticle Physics, WORLD SCIENTIFIC, 2005 218, URL: http://dx.doi.org/10.1142/9789812701893_0016 (cit. on p. 56).

[174] G. Isidori, Y. Nir, and G. Perez, *Flavor Physics Constraints for Physics Beyond the Standard Model*, Annual Review of Nuclear and Particle Science **60** (2010) 355, ISSN: 1545-4134, URL: http://dx.doi.org/10.1146/annurev.nucl.012809.104534 (cit. on p. 56).

[175] I. Brivio and M. Trott, *The standard model as an effective field theory*, Physics Reports **793** (2019) 1, ISSN: 0370-1573, URL: http://dx.doi.org/10.1016/j.physrep.2018.11.002 (cit. on pp. 57, 58).

[176] W. BuchmÃŒller and D. Wyler, *Effective lagrangian analysis of new interactions and flavour conservation*, Nuclear Physics B **268** (1986) 621, ISSN: 0550-3213, URL: https://www.sciencedirect.com/science/article/pii/0550321386902622 (cit. on p. 58).

[177] B. Grzadkowski, M. Iskrzyński, M. Misiak, and J. Rosiek, *Dimension-six terms in the Standard Model Lagrangian*, Journal of High Energy Physics **2010** (2010), ISSN: 1029-8479, URL: http://dx.doi.org/10.1007/JHEP10(2010)085 (cit. on p. 58).

[178] O. J. P. Éboli, M. C. Gonzalez-Garcia, and J. K. Mizukoshi, *$pp \to jje^{\pm}\mu^{\pm}\nu\nu$ and $jje^{\pm}\mu^{\mp}\nu\nu$ at $O(\alpha_{em}^6)$ and $O(\alpha_{em}^4\alpha_s^2)$ for the study of the quartic electroweak gauge boson vertex at CERN LHC*, Phys. Rev. D **74** (7 2006) 073005, URL: https://link.aps.org/doi/10.1103/PhysRevD.74.073005 (cit. on pp. 58–61, 66).

[179] O. J. P. Éboli and M. C. Gonzalez–Garcia, *Classifying the bosonic quartic couplings*, Phys. Rev. D **93** (9 2016) 093013, URL: https://link.aps.org/doi/10.1103/PhysRevD.93.093013 (cit. on pp. 58, 59, 61, 66).

[180] ATLAS Collaboration, *Combined effective field theory interpretation of Higgs boson and weak boson production and decay with ATLAS data and electroweak precision observables*, ATL-PHYS-PUB-2022-037, 2022, URL: https://cds.cern.ch/record/2816369 (cit. on p. 59).

[181] CMS Collaboration, *Measurements of the ZZ production cross sections in the $2\ell2\nu$ channel in proton–proton collisions at $\sqrt{s} = 7$ and 8 TeV and combined constraints on triple gauge couplings*, Eur. Phys. J. C **75** (2015) 511, arXiv: 1503.05467 [hep-ex] (cit. on p. 59).

[182] A. Falkowski, *Lectures on SMEFT*, Eur. Phys. J. C **83** (656 2023), URL: https://doi.org/10.1140/epjc/s10052-023-11821-3 (cit. on p. 59).

[183] G. Durieux et al., *LHC EFT WG Note: Basis for Anomalous Quartic Gauge Couplings*, (2025), arXiv: 2411.02483 [hep-ph], URL: https://arxiv.org/abs/2411.02483 (cit. on pp. 59–61).

[184] E. d. S. Almeida, O. J. P. Éboli, and M. C. Gonzalez–Garcia,
Unitarity constraints on anomalous quartic couplings, Physical Review D **101** (2020),
ISSN: 2470-0029, URL: http://dx.doi.org/10.1103/PhysRevD.101.113003
(cit. on pp. 61, 70).

[185] W. Kilian, M. Sekulla, T. Ohl, and J. Reuter,
High-energy vector boson scattering after the Higgs boson discovery,
Phys. Rev. D **91** (9 2015) 096007,
URL: https://link.aps.org/doi/10.1103/PhysRevD.91.096007 (cit. on p. 61).

[186] G. Perez, M. Sekulla, and D. Zeppenfeld, *Anomalous quartic gauge couplings and unitarization for the vector boson scattering process* $pp \to W^+W^+jjX \to \ell^+\nu_\ell\ell^+\nu_\ell jjX$,
The European Physical Journal C **78** (2018), ISSN: 1434-6052,
URL: http://dx.doi.org/10.1140/epjc/s10052-018-6230-1 (cit. on p. 61).

[187] I. Brivio et al., *LHC EFT WG note: Truncation, validity, uncertainties*, (2022),
arXiv: 2201.04974, URL: https://cds.cern.ch/record/2798082 (cit. on p. 61).

[188] M. G.-G. O.J.P. Eboli, $e^\pm\mu^\pm$ Anomalous quartic electroweak gauge-boson interactions,
URL: https://feynrules.irmp.ucl.ac.be/wiki/AnomalousGaugeCoupling
(cit. on pp. 61–63).

[189] ATLAS Collaboration,
Measurements of $Z\gamma$ *and* $Z\gamma\gamma$ *production in* pp *collisions at* $\sqrt{s} = 8$ *TeV with the ATLAS detector*,
Phys. Rev. D **93** (2016) 112002, arXiv: 1604.05232 [hep-ex] (cit. on pp. 62, 65).

[190] ATLAS Collaboration, *Evidence of* $W\gamma\gamma$ *Production in* pp *Collisions at* $\sqrt{s} = 8$ *TeV and Limits on Anomalous Quartic Gauge Couplings with the ATLAS Detector*,
Phys. Rev. Lett. **115** (2015) 031802, arXiv: 1503.03243 [hep-ex] (cit. on pp. 62, 65).

[191] ATLAS Collaboration, *Measurement of exclusive* $\gamma\gamma \to W^+W^-$ *production and search for exclusive Higgs boson production in* pp *collisions at* $\sqrt{s} = 8$ *TeV using the ATLAS detector*,
Phys. Rev. D **94** (2016) 032011, arXiv: 1607.03745 [hep-ex] (cit. on p. 62).

[192] ATLAS Collaboration, *Evidence for Electroweak Production of* $W^\pm W^\pm jj$ *in* pp *Collisions at* $\sqrt{s} = 8$ *TeV with the ATLAS Detector*, Phys. Rev. Lett. **113** (2014) 141803,
arXiv: 1405.6241 [hep-ex] (cit. on pp. 62, 65).

[193] S. T. J. Manjarres, $e^\pm\mu^\pm$ Dim-8 Generation of MC samples,
URL: https://twiki.cern.ch/twiki/bin/viewauth/AtlasProtected/DIM8EFT
(cit. on p. 63).

[194] C. Degrande et al., *Monte Carlo tools for studies of non-standard electroweak gauge boson interactions in multi-boson processes: A Snowmass White Paper*, (2013),
arXiv: 1309.7890 [hep-ph], URL: https://arxiv.org/abs/1309.7890 (cit. on pp. 64, 65).

[195] ATLAS Collaboration, *Combined effective field theory interpretation of* $W^\pm Zjj$ *and* $W^\pm W^\pm jj$ *measurements using ATLAS* 13 *TeV data*, ATL-PHYS-PUB-2023-002, 2023,
URL: https://cds.cern.ch/record/2850667 (cit. on pp. 65, 68, 70–72).

[196] CMS Collaboration, *Measurements of production cross sections of* WZ *and same-sign* WW *boson pairs in association with two jets in proton–proton collisions at* $\sqrt{s} = 13$ *TeV*,
Phys. Lett. B **809** (2020) 135710, arXiv: 2005.01173 [hep-ex] (cit. on pp. 65, 71).

[197] CMS Collaboration, *Study of same-sign W boson scattering and anomalous couplings in events with one tau lepton from pp collisions at $\sqrt{s} = 13$ TeV*, (2024), arXiv: 2410.04210 [hep-ex] (cit. on pp. 65, 67).

[198] *Study of semileptonic vector boson scattering and anomalous quartic gauge coupling from proton-proton collisions at 13 TeV*, (2025), URL: https://cds.cern.ch/record/2926224 (cit. on p. 65).

[199] ATLAS Collaboration, *Differential cross-section measurements of the production of four charged leptons in association with two jets using the ATLAS detector*, JHEP **01** (2024) 004, arXiv: 2308.12324 [hep-ex] (cit. on p. 65).

[200] CMS Collaboration, *Evidence for electroweak production of four charged leptons and two jets in proton–proton collisions at $\sqrt{s} = 13$ TeV*, Phys. Lett. B **812** (2021) 135992, arXiv: 2008.07013 [hep-ex] (cit. on p. 65).

[201] CMS Collaboration, *Search for anomalous electroweak production of vector boson pairs in association with two jets in proton–proton collisions at 13 TeV*, Phys. Lett. B **798** (2019) 134985, arXiv: 1905.07445 [hep-ex] (cit. on p. 65).

[202] ATLAS Collaboration, *Fiducial and differential cross-section measurements of electroweak $W\gamma jj$ production in pp collisions at $\sqrt{s} = 13$ TeV with the ATLAS detector*, Eur. Phys. J. C **84** (2024) 1064, arXiv: 2403.02809 [hep-ex] (cit. on p. 65).

[203] CMS Collaboration, *Measurement of the electroweak production of $W\gamma$ in association with two jets in proton–proton collisions at $\sqrt{s} = 13$ TeV*, Phys. Rev. D **108** (2023) 032017, arXiv: 2212.12592 [hep-ex] (cit. on p. 65).

[204] CMS Collaboration, *Search for the production of $W^{\pm}W^{\pm}W^{\mp}$ events at $\sqrt{s} = 13$ TeV*, Phys. Rev. D **100** (2019) 012004, arXiv: 1905.04246 [hep-ex] (cit. on p. 65).

[205] ATLAS Collaboration, *Observation of VVZ production at $\sqrt{s} = 13$ TeV with the ATLAS detector*, (2024), arXiv: 2412.15123 [hep-ex] (cit. on p. 65).

[206] CMS Collaboration, *Measurements of the $pp \to W^{\pm}\gamma\gamma$ and $pp \to Z\gamma\gamma$ cross sections at $\sqrt{s} = 13$ TeV and limits on anomalous quartic gauge couplings*, JHEP **10** (2021) 174, arXiv: 2105.12780 [hep-ex] (cit. on p. 65).

[207] ATLAS Collaboration, *Search for anomalous electroweak production of WW/WZ in association with a high-mass dijet system in pp collisions at $\sqrt{s} = 8$ TeV with the ATLAS detector*, Phys. Rev. D **95** (2017) 032001, arXiv: 1609.05122 [hep-ex] (cit. on p. 65).

[208] ATLAS Collaboration, *Study of $WW\gamma$ and $WZ\gamma$ production in pp collisions at $\sqrt{s} = 8$ TeV and search for anomalous quartic gauge couplings with the ATLAS experiment*, Eur. Phys. J. C **77** (2017) 646, arXiv: 1707.05597 [hep-ex] (cit. on p. 65).

[209] CMS Collaboration, *Search for $WW\gamma$ and $WZ\gamma$ production and constraints on anomalous quartic gauge couplings in pp collisions at $\sqrt{s} = 8$ TeV*, Phys. Rev. D **90** (2014) 032008, arXiv: 1404.4619 [hep-ex] (cit. on p. 65).

[210] J. J. Ethier, R. Gomez-Ambrosio, G. Magni, and J. Rojo, *SMEFT analysis of vector boson scattering and diboson data from the LHC Run II*, The European Physical Journal C **81** (2021), ISSN: 1434-6052, URL: http://dx.doi.org/10.1140/epjc/s10052-021-09347-7 (cit. on p. 67).

[211] R. Bellan et al.,
A sensitivity study of VBS and diboson WW to dimension-6 EFT operators at the LHC,
Journal of High Energy Physics **2022** (2022), ISSN: 1029-8479,
URL: http://dx.doi.org/10.1007/JHEP05(2022)039 (cit. on p. 67).

[212] G. Apollinari, I. Béjar Alonso, O. Brüning, M. Lamont, and L. Rossi,
$e^{\pm}\mu^{\pm}$ High-Luminosity Large Hadron Collider (HL-LHC): Preliminary Design Report,
CERN Yellow Reports: Monographs, Geneva: CERN, 2015,
URL: https://cds.cern.ch/record/2116337 (cit. on p. 75).

[213] lhc-commissioning-web, $e^{\pm}\mu^{\pm}$ Longer term LHC schedule,
URL: https://lhc-commissioning.web.cern.ch/schedule/LHC-long-term.htm,
(accessed: 14.04.2025) (cit. on p. 75).

[214] Biscarat, Catherine, Caillou, Sylvain, Rougier, Charline, Stark, Jan, and Zahreddine, Jad, *Towards a realistic track reconstruction algorithm based on graph neural networks for the HL-LHC*,
EPJ Web Conf. **251** (2021) 03047,
URL: https://doi.org/10.1051/epjconf/202125103047 (cit. on p. 76).

[215] A. Collaboration, $e^{\pm}\mu^{\pm}$ Track finding performance plots for a Graph Neural Network pipeline on ATLAS ITk Simulated Data,
URL: https://atlas.web.cern.ch/Atlas/GROUPS/PHYSICS/PLOTS/IDTR-2022-01/,
(accessed: 14.04.2025) (cit. on p. 76).

[216] J. D. Burleson et al., *Physics Performance of the ATLAS GNN4ITk Track Reconstruction Chain*,
tech. rep., CERN, 2023, URL: https://cds.cern.ch/record/2882507 (cit. on p. 76).

[217] ATLAS Collaboration, *Studies of new Higgs boson interactions through nonresonant HH production in the $b\bar{b}\gamma\gamma$ final state in pp collisions at $\sqrt{s}$ = 13 TeV with the ATLAS detector*,
JHEP **01** (2024) 066, arXiv: 2310.12301 [hep-ex] (cit. on p. 76).

[218] ATLAS Collaboration, *Search for the non-resonant production of Higgs boson pairs via gluon fusion and vector-boson fusion in the $b\bar{b}\tau^+\tau^-$ final state in proton–proton collisions at $\sqrt{s}$ = 13 TeV with the ATLAS detector*, Phys. Rev. D **110** (2024) 032012,
arXiv: 2404.12660 [hep-ex] (cit. on p. 76).

[219] ATLAS Collaboration, *Search for nonresonant pair production of Higgs bosons in the $b\bar{b}b\bar{b}$ final state in pp collisions at $\sqrt{s}$ = 13 TeV with the ATLAS detector*, Phys. Rev. D **108** (2023) 052003,
arXiv: 2301.03212 [hep-ex] (cit. on p. 76).

[220] ATLAS Collaboration, *Search for pair production of boosted Higgs bosons via vector-boson fusion in the $b\bar{b}b\bar{b}$ final state using pp collisions at $\sqrt{s}$ = 13 TeV with the ATLAS detector*,
Phys. Lett. B **858** (2024) 139007, arXiv: 2404.17193 [hep-ex] (cit. on p. 76).

[221] ATLAS Collaboration, *Search for non-resonant Higgs boson pair production in final states with leptons, taus, and photons in pp collisions at $\sqrt{s}$ = 13 TeV with the ATLAS detector*,
JHEP **08** (2024) 164, arXiv: 2405.20040 [hep-ex] (cit. on p. 76).

[222] ATLAS Collaboration, *Search for non-resonant Higgs boson pair production in the $2b + 2\ell + E_T^{miss}$ final state in pp collisions at $\sqrt{s}$ = 13TeV with the ATLAS detector*,
JHEP **02** (2024) 037, arXiv: 2310.11286 [hep-ex] (cit. on p. 76).

[223] ATLAS Collaboration, *Combination of Searches for Higgs Boson Pair Production in pp Collisions at $\sqrt{s}$ = 13 TeV with the ATLAS detector*, Phys. Rev. Lett. **133** (2024) 101801,
arXiv: 2406.09971 [hep-ex] (cit. on p. 77).

[224] *Projected sensitivity of measurements of Higgs boson pair production with the ATLAS experiment at the HL-LHC*, tech. rep., All figures including auxiliary figures are available at https://atlas.web.cern.ch/Atlas/GROUPS/PHYSICS/PUBNOTES/ATL-PHYS-PUB-2025-006: CERN, 2025, URL: https://cds.cern.ch/record/2925853 (cit. on p. 77).

[225] B. Henning, D. Lombardo, M. Riembau, and F. Riva, *Measuring Higgs Couplings without Higgs Bosons*, Physical Review Letters **123** (2019), ISSN: 1079-7114, URL: http://dx.doi.org/10.1103/PhysRevLett.123.181801 (cit. on p. 79).

[226] C. Englert, Q. Li, M. Spannowsky, M. Wang, and L. Wang, *VBS WÂ±WÂ±H production at the HL-LHC and a 100 TeV pp-collider*, International Journal of Modern Physics A **32** (2017) 1750106, eprint: https://doi.org/10.1142/S0217751X17501068, URL: https://doi.org/10.1142/S0217751X17501068 (cit. on p. 79).

[227] *Search for HHWW couplings in the VBS production of* $\mathrm{W^\pm W^\pm H}$*, with* $\mathrm{H} \rightarrow \mathrm{b\bar{b}}$ *decays*, tech. rep., CERN, 2024, URL: https://cds.cern.ch/record/2905615 (cit. on p. 79).

[228] *Handbook of LHC Higgs Cross Sections: 3. Higgs Properties: Report of the LHC Higgs Cross Section Working Group*, 2013, URL: http://cds.cern.ch/record/1559921 (cit. on p. 79).

[229] L. M. Lehmann, *Sensitivity study on the Higgs boson's trilinear self-coupling with the VBS ssWWh signal at the ATLAS detector*, Presented 2024, Dresden, Tech. U., 2024, URL: https://cds.cern.ch/record/2905993 (cit. on p. 79).

[230] ATLAS Collaboration, *Prospects for the measurement of the* $W^\pm W^\pm$ *scattering cross section and extraction of the longitudinal scattering component in* pp *collisions at the High-Luminosity LHC with the ATLAS Experiment*, ATL-PHYS-PUB-2018-052, 2018, URL: https://cds.cern.ch/record/2652447 (cit. on p. 80).

[231] ATLAS Collaboration, *Prospective study of vector boson scattering in WZ fully leptonic final state at HL-LHC*, ATL-PHYS-PUB-2018-023, 2018, URL: https://cds.cern.ch/record/2645271 (cit. on p. 80).

[232] *Prospects for the measurement of electroweak and polarized WZ to 3lv production cross sections at the High-Luminosity LHC*, tech. rep., CERN, 2018, URL: https://cds.cern.ch/record/2650774 (cit. on p. 80).

[233] *Vector Boson Scattering prospective studies in the ZZ fully leptonic decay channel for the High-Luminosity and High-Energy LHC upgrades*, tech. rep., CERN, 2018, URL: https://cds.cern.ch/record/2650915 (cit. on p. 80).

[234] J. Roloff, V. Cavaliere, M.-A. Pleier, and L. Xu, *Sensitivity to longitudinal vector boson scattering in semileptonic final states at the HL-LHC*, Physical Review D **104** (2021), ISSN: 2470-0029, URL: http://dx.doi.org/10.1103/PhysRevD.104.093002 (cit. on p. 80).